SECURITY INFORMATION

CONFIDENTIAL

Copy 207
RM L53I30b

NACA RM L53I30b

NACA

Reissued as TN 3817

RESEARCH MEMORANDUM

TWO-DIMENSIONAL LOW-SPEED CASCADE INVESTIGATION OF NACA COMPRESSOR BLADE SECTIONS HAVING A SYSTEMATIC VARIATION IN MEAN-LINE LOADING

By John R. Erwin, Melvyn Savage, and James C. Emery

Langley Aeronautical Laboratory
Langley Field, Va.

NATIONAL ADVISORY COMMITTEE FOR AERONAUTICS

WASHINGTON

November 25, 1953

CONFIDENTIAL

NATIONAL ADVISORY COMMITTEE FOR AERONAUTICS

RESEARCH MEMORANDUM

TWO-DIMENSIONAL LOW-SPEED CASCADE INVESTIGATION OF NACA COMPRESSOR BLADE SECTIONS HAVING A SYSTEMATIC VARIATION IN MEAN-LINE LOADING

By John R. Erwin, Melvyn Savage, and James C. Emery

SUMMARY

The low-speed cascade performance of the high-speed NACA 65-$(C_{l_o}A_2I_{8b})$10 compressor blade sections has been systematically investigated. Porous test-section side walls and porous flexible end walls were employed to establish a close simulation of two-dimensional flow. Blade-section cambers of 0.4, 0.8, 1.2, and 1.8 were tested over the usable angle-of-attack range for inlet angles β of 30°, 45°, and 60° at solidities σ of 1.0 and 1.5. A sufficient number of cascade configurations were tested to permit interpolation and extrapolation of the data within the usual range of application.

Comparative tests of blade sections having an isolated airfoil lift coefficient of 1.2 were made for two other blade sections with mean lines having different loading distributions at an inlet angle of 45° with a solidity of 1.5 and at an inlet angle of 60° with a solidity of 1.0. The results of this comparison indicated that the data presented herein, when utilized in conjunction with published cascade data for the NACA 65-$(C_{l_o}A_{10})$10 series blades, will permit a fairly accurate prediction of design performance for most compressor blade sections since the mean lines tested are believed to encompass the practical range of compressor-blade mean-line loading distributions.

A comparative evaluation of the cascade test results obtained for the mean lines investigated indicated that the NACA 65-$(C_{l_o}A_2I_{8b})$10 and NACA 65-$(C_{l_o}A_6I_{4b})$10 blades should be capable of efficient operation to a higher inlet Mach number than the 65-$(C_{l_o}A_{10})$10 blades at high inlet angles and low solidities (β = 60°; σ = 1.0). At low inlet angles and high solidities (β = 45°; σ = 1.5), the NACA 65-$(C_{l_o}A_6I_{4b})$10 blades appeared to offer better high-speed capabilities than either the 65-$(C_{l_o}A_2I_{8b})$10 or the 65-$(C_{l_o}A_{10})$10 blades.

INTRODUCTION

The design of more powerful jet-propulsion engines for transonic and supersonic aircraft will require high-flow-capacity compressors. Since the compressor frontal area should be held to a minimum from engine-drag considerations, and since very low inlet hub-to-tip diameter ratios are currently being used, any appreciable gain in flow capacity can best be achieved by increases in axial velocity and hence blade inlet Mach number. From size, weight, cost, production time, and stage-matching considerations, it is desirable to raise the magnitude of stage-pressure rise and thereby reduce the number of stages necessary to obtain the design over-all pressure ratio. Higher stage-pressure rises generally require higher blade inlet Mach numbers. Hence, in order to obtain high flow capacities and high stage-pressure ratios, compressor blade sections must be developed which can operate efficiently at higher inlet Mach numbers than are presently in use.

The blade sections currently used in subsonic axial-flow compressors have circular-arc, parabolic, or constant-loading mean lines with the position of maximum section thickness well forward at the 30- to 40-percent-chord point (refs. 1 to 4). At design angle of attack for such blades, the velocity of the flow over the forward portion of the convex surface is considerably above the free-stream inlet velocity. Thus, if these sections are used at higher inlet Mach numbers, sonic and supersonic velocities occur over the forward convex surface. Toward the rear of the blade the stream velocity is reduced and the surface velocities are much lower than near the leading edge. It was felt that blade sections capable of efficient operation at higher Mach numbers could be obtained by effecting a reduction in blade-surface velocities over the forward portion of the blade. This reduction can be accomplished by altering either the loading distribution, that is, the mean-line shape, or the thickness distribution, or both. Transonic rotor tests (ref. 5) indicated that reducing the surface velocities in the forward portion of the blade by shifting the mean-line loading rearward raised the efficient operating Mach number level considerably above that currently being used. Transonic stage tests (ref. 6) indicated the same success when the surface-velocity reduction was accomplished by altering the thickness distribution used in conjunction with a mean line which has an elliptical loading distribution, and by reducing the maximum thickness.

The purpose of the present investigation is to present sufficient low-speed cascade data for blade sections having a systematic variation in mean-line loading to permit compressor designers to use such blade sections. The conventional NACA 65-series thickness distribution with 10 percent maximum thickness was used for all the blade sections. In addition, an estimation of the comparative effectiveness of the variation in mean-line loading in improving high-speed and transonic performance has been made.

SYMBOLS

A_1	area of far upstream stream tube bounded by stagnation streamlines of two adjacent blade sections
A_T	minimum passage area between two adjacent blade sections
a	mean-line loading designation
c	blade chord, ft
C_d	section drag coefficient
C_l	section lift coefficient
C_{l_o}	camber, expressed as design lift coefficient of isolated airfoil
C_N	section normal-force coefficient
C_{N_M}	section normal-force coefficient obtained by calculation of momentum and pressure changes across blade row
C_{N_P}	section normal-force coefficient obtained by integration of blade-surface pressure distribution
C_w	wake-momentum-difference coefficient
g	tangential spacing between blades, ft
l/d	lift-drag ratio, C_l/C_d
P	total pressure, lb/sq ft
P_R	resultant pressure coefficient; difference between local convex- and concave-surface pressure coefficients
p	static pressure, lb/sq ft
q	dynamic pressure, lb/sq ft
$\Delta p/q$	nondimensional static-pressure-rise parameter
R	Reynolds number based on blade chord

S pressure coefficient, $\frac{P - p_l}{q_1}$

x chordwise distance from blade leading edge, percent chord

y perpendicular distance from blade chord line, percent chord

α angle between flow direction and blade chord, deg

β angle between flow direction and cascade axis, deg (see fig. 1)

θ flow turning angle, deg

σ solidity, chord of blades divided by tangential spacing, c/g

Subscripts:

d design, when used with angles

l local

1 upstream of blade row

2 downstream of blade row

APPARATUS

Description of Test Equipment

The test facility used in this investigation was the Langley 5-inch, low-speed, porous-wall cascade tunnel described in reference 4 and shown in figure 1. The only change incorporated into the test rig as described in reference 4 was a screen of 1/2-inch mesh hardware cloth which was placed at the nozzle inlet. (See fig. 1.) This coarse screen was intended to increase the tunnel turbulence level in order to improve the probability of transition of the laminar boundary layer of the blade without laminar separation. It was felt that the cascade test results would more closely approximate actual compressor operation if the cascade turbulence level more closely approximated the actual compressor turbulence level.

DESCRIPTION OF AIRFOILS

The blade families used in this investigation were formed by combining the NACA 65-010 basic thickness distribution, modified to include

a trailing-edge radius of 1 percent chord with cambered mean lines. The amount of camber is expressed as the design lift coefficient C_{l_o} for the isolated airfoil. A system of designating mean lines derived by combining the mean lines presented in reference 7 in varying proportions has been presented in reference 8. For completeness, this system is briefly reviewed here. The basic mean lines having the type of loading ranging from $a = 0$ to 1.0 in reference 7 are given designations starting with A for $a = 1.0$ and ending with K for $a = 0$. The camber of each basic mean line used to derive a combined mean line of $C_{l_o} = 1.0$ is indicated in tenths as a subscript to the letter designating that basic mean line. The subscript "b" is used to indicate that the basic mean line is added backwards; that is, the mean line as given in reference 7 is reversed so that the trailing edge is considered to be the leading edge and conversely. Since all the blade sections tested in this report have the same thickness distribution and vary only in the mean-line shape, the terms "mean line" and "blade" will be used interchangebly when discussing different mean lines.

A_2I_{8b} Mean Line

Many basic mean lines or combinations of basic mean lines are available to produce the desired condition of low convex-surface velocities in the forward region. Preliminary studies of the problem indicated that a triangular-loading diagram increasing from zero at the leading edge to a maximum value at the trailing edge would be desirable. (These studies did not fully consider the strong effects of the passage area upon the surface velocities, however.) The triangular-loading diagram could be obtained by using the basic NACA $a = o$ mean line reversed (K_b). Two practical difficulties weighed against the use of the K_b mean line. The condition of maximum loading at 100 percent chord would require an extremely rapid pressure recovery that probably would not occur in practical applications. A less serious objection was that the K_b mean line exhibited a reflex curvature in the forward portion. For these reasons, a mean line having a more gradual pressure recovery in the rearward portion of the blade and a nonreflexed curvature was selected. This camber line was derived for $C_{l_o} = 1.0$ by adding the mean lines presented in reference 7 in the proportions of $a = 1.0$ for $C_{l_o} = 0.2$ and $a = 0.2$ backwards for $C_{l_o} = 0.8$. By using the designation system outlined previously, this mean line is denoted A_2I_{8b}. The distribution of isolated airfoil resultant pressure coefficients P_R is shown in figure 2(a) for $C_{l_o} = 1.0$. Ordinates and slopes for the A_2I_{8b} compressor blade mean line

for $C_{l_o} = 1.0$ are given in table I and the mean line is indicated in figure 2(b). Both ordinates and slopes are scaled directly to obtain other cambers. Cambered blade sections are obtained by applying the thickness perpendicular to the mean line at stations laid out along the chord line. In the section designation, the amount of camber is given by the first number after the dash in tenths of C_{l_o} and the letter designation for the type of mean line follows the camber. For example, an A_2I_{8b} blade having $C_{l_o} = 1.2$ and an NACA 65-010 thickness distribution is designated as the NACA 65-$(12A_2I_{8b})$10 blade section. This blade is shown in figure 2(c). All the A_2I_{8b} blade sections tested are shown in figure 3 and their coordinates are presented in tables II to V.

The blade sections tested in the investigation reported in reference 4 were composed of A_{10} $(a = 1.0)$ mean lines and NACA 65-series thickness distributions. The A_{10} mean line has uniform loading when used as an isolated airfoil. The distribution of isolated-airfoil resultant-pressure coefficients P_R is shown in figure 2(a) for $C_{l_o} = 1.0$. The mean line is indicated in figure 2(b) and the NACA 65-$(12A_{10})$10 blade section is indicated in figure 2(c). The A_2I_{8b} blades differ from these conventional A_{10} blades in that, by shifting the mean-line loading to the rear, the incremental surface velocities due to loading have been reduced over the forward portion of the convex surface. Since, for high subsonic inlet Mach numbers, choking may occur in the blade passage, it is desirable to examine the blade passage to determine what effect the A_2I_{8b} loading has had on blade passage minimum areas. By laying out large-scale drawings of blade passages for both the A_2I_{8b} blades and the conventional A_{10} blades at design angle of attack for various combinations of inlet air angle, solidity, and camber, the ratio of minimum passage area A_T to inlet area A_1 could be measured. Figure 4 presents A_T/A_1 plotted against inlet air angle β_1 for solidity $\sigma = 1.0$ and 1.5 and camber $C_{l_o} = 0.4$, 0.8, 1.2, and 1.8 for both A_2I_{8b} and A_{10} blades at design angle of attack (the angle for which there is no contribution of angle of attack to the surface pressures). It appears that shifting the loading to the rear has decreased the minimum area of the blade passage. Hence, at low inlet air angles and high solidities, the A_2I_{8b} blade sections at design angle of attack may well present choking problems.

The passage area can be increased to some extent by setting the blades at angles of attack above design or by altering the thickness. In order to determine how much increasing angle of attack relieves choking, the variation of A_T/A_1 with angle of attack for the NACA 65-$(12A_2I_{8b})$10 blade at $\beta = 30°$, 45°, and 60° at $\sigma = 1.0$ and 1.5 was determined and

is presented in figure 5. It can be seen that for both solidities the increase in A_T/A_1 accomplished by an increase in angle of attack becomes greater as inlet air angle increases. However, even at the lower inlet air angle, where the design angle-of-attack condition presents a possibly choked passage $\left(\frac{A_T}{A_1} < 1.0\right)$, the relieving effect of increasing angle of attack is appreciable. For example, at $\beta = 45^\circ$ and $\sigma = 1.0$, $A_T/A_1 = 0.985$ for design angle of attack. Increasing the angle of attack by 2° results in a value of A_T/A_1 of 1.011. Of course, if the angle of attack is increased to alleviate the choking condition, the high angle-of-attack operating range of a compressor-blade row may be reduced.

A_6I_{4b} Mean Line

The A_2I_{8b} mean lines represent a rather radical departure from conventional compressor-blade practice. Blade sections intermediate between the A_{10} and A_2I_{8b} series might offer advantages of moderately increased critical speed and more open passage area. Hence, another family of high-critical-speed blades has been developed in which the mean line is just halfway between the A_2I_{8b} and the conventional A_{10} mean lines. This mean line is derived for $C_{l_o} = 1.0$ by adding the mean lines presented in reference 7 in the proportions of $a = 1.0$ for $C_{l_o} = 0.6$ and $a = 0.2$ backwards for $C_{l_o} = 0.4$. Again the NACA 65-010 thickness distribution was used. By using the previously mentioned mean-line designation system, this family of blades is denoted as the A_6I_{4b} blades. The distribution of isolated-airfoil resultant-pressure coefficients P_R for this mean line at $C_{l_o} = 1.0$ is indicated in figure 2(a). Coordinates and slopes for the A_6I_{4b} mean line for $C_{l_o} = 1.0$ are given in table VI and the mean line is shown in figure 2(b). The coordinates for the NACA $65\text{-}(12A_6I_{4b})10$ blade section are given in table VII and the blade is indicated in figure 2(c). The values of A_T/A_1 for the A_2I_{8b}, A_6I_{4b}, and A_{10} compressor blades at $C_{l_o} = 1.2$ for various inlet angles at solidities of 1.0 and 1.5 are presented in figure 6. The A_6I_{4b} blade passages present a degree of openness which is closer to the A_{10} blades than to the A_2I_{8b} blades. The A_6I_{4b} blades have higher critical-speed characteristics than the A_{10} blades but possibly not as high as the A_2I_{8b} blades. However, for low inlet air angles and high solidities, the A_2I_{8b} blades may be choked, necessitating the use of some intermediate series of blades such as the A_6I_{4b}.

A_6I_4 Mean Line

As stated previously, the A_2I_{8b} and A_6I_{4b} blades have their loading shifted to the rear, whereas the A_{10} blade is a constant loading blade. It is felt that the A_2I_{8b} blade is at the extreme end of the rearward-loading type of blade. In order to encompass the outer extreme, which is a forward-loading type of blade, a mean line was developed which is derived for $C_{l_o} = 1.0$ by adding mean lines in the following proportions: $a = 1.0$ for $C_{l_o} = 0.6$ plus $a = 0.2$ for $C_{l_o} = 0.4$. This mean line will hereinafter be denoted as the A_6I_4 mean line. The distribution of isolated-airfoil resultant-pressure coefficient P_R for this mean line at $C_{l_o} = 1.0$ is indicated in figure 2(a). Coordinates and slopes for the A_6I_4 mean line for $C_{l_o} = 1.0$ are given in table VIII and the mean line is indicated in figure 2(b). The coordinates for the NACA 65-$(12A_6I_4)$10 blade section are given in table IX and the airfoil is indicated in figure 2(c). The values of A_T/A_1 for this type of blade are included in figure 6 for completeness.

REYNOLDS NUMBER, TURBULENCE LEVEL, AND SURFACE ROUGHNESS

Since both A_2I_{8b} and A_6I_{4b} blades have more favorable convex-surface pressure gradients than the A_{10} blades, they show a greater tendency toward extensive regions of laminar boundary-layer flow than do the A_{10} blades. Boundary-layer transition becomes more likely as Reynolds number, turbulence level, and surface roughness are increased. In compressors, the turbulence level and Reynolds numbers are generally different from those occurring in low-speed cascade tunnels. Hence, the amount of laminar boundary-layer flow in the two-dimensional low-speed cascade may well be different from that in the compressor. Another significant difference between the compressor and the cascade tunnel is that, in the compressor, radial flows exist which will affect the nature of the boundary-layer flow. Hence, exact simulation of compressor boundary-layer flow cannot be obtained in two-dimensional cascade tunnels. It is not known whether the best simulation of compressor performance is obtained in low-speed cascade tests by permitting laminar boundary-layer flow if the pressure gradients, turbulence level, and Reynolds numbers support it, or whether transition to a turbulent boundary layer should be induced by some artificial means such as surface roughness. One prime difficulty in artificially inducing transition with surface roughness is that the resulting blade performance appears to be affected by the magnitude and location of the surface roughness. Hence, it was decided that the main

portion of the tests would be conducted with smooth blades (no surface roughness) since (1) duplication of compressor boundary-layer flow cannot be attained in the two-dimensional cascade, and (2) since simulation of compressor performance in the cascade tunnel would require adjustment of the magnitude and location of surface roughness to account for the influence of the various radial-flow effects which exist only in the compressor. In order to approximate compressor performance more closely, the A_2I_{8b} blades were tested at as high a Reynolds number as was practical (approximately 444,000 based on blade chord which corresponds to an entering velocity of 165 ft/sec). This Reynolds number is considerably higher than that of 245,000 used for most of the A_{10} blades of reference 4. Since the A_6I_{4b} and A_6I_4 blades were less susceptible to extensive laminar-flow regions than the A_2I_{8b} blades, the Reynolds number for these tests was maintained at approximately 346,000. The effect on blade-section turning angle of varying Reynolds number by varying inlet velocity was investigated over a Reynolds number range from 160,000 to 520,000 for the NACA 65-$(12A_2I_{8b})$10 blade section at $\beta = 60^\circ$, $\sigma = 1.0$, and $\alpha = 9.6^\circ$. This series of tests was repeated but the turbulence level was reduced by removing the coarse screen.

In order to study the effects of surface roughness on cascade blade performance, additional tests were made for most cascade combinations for the A_2I_{8b} blades near the design angle of attack by using surface roughness. Previously used methods of eliminating laminar boundary-layer flow by adding leading-edge roughness were not effective for the A_2I_{8b} blades. The types of surface roughness used consisted of either (1) 1/16-inch-wide strips of masking tape at the 35-percent-chord point on the upper surface running from wall to wall, or (2) No. 600 carborundum paper draped around the blade leading-edge region from 35-percent-chord point on the convex surface to the 35-percent-chord point on the concave surface. Some tests were made in which Scotch brand cellophane tape was substituted for the masking tape at the 35-percent-chord point. All the A_2I_{8b} roughness test data presented were for the masking-tape type of roughness except for the $C_{l_o} = 1.8$ tests at $\beta = 30^\circ$ with $\sigma = 1.0$ and 1.5, and $\beta = 60^\circ$ with $\sigma = 1.5$ in which carborundum paper was used.

In order to study further the effects of surface roughness, tests of the NACA 65-$(12A_2I_{8b})$10 blade section were made at $\beta = 45^\circ$ with $\sigma = 1.5$ and at $\beta = 60^\circ$ with $\sigma = 1.0$ with and without roughness through the angle-of-attack range. Similar tests were made for the NACA 65-$(18A_2I_{8b})$10 blade section at $\beta = 45^\circ$ with $\sigma = 1.0$.

TEST PROGRAM AND PROCEDURE

Range of Test Program

The test program for the A_2I_{8b} blades was planned to provide enough information to satisfy conventional compressor-velocity diagrams when these data are used in conjunction with the A_{10} data presented in reference 4. Tests of seven blade cascades were made at inlet air angles β of 30°, 45°, and 60° with solidities σ of 1.0 and 1.5 for cambers C_{l_o} of 0.4, 0.8, 1.2, and 1.8. Additional tests were made to determine design angle of attack and design turning angle at $\beta = 60°$ with $\sigma = 0.50$ for these cambers. The A_6I_{4b} and A_6I_4 blades of $C_{l_o} = 1.2$ were tested at $\beta = 45°$ with $\sigma = 1.5$ and at $\beta = 60°$ with $\sigma = 1.0$.

Examination and interpolation of the test data presented in this report for the A_2I_{8b}, A_6I_{4b}, and A_6I_4 mean lines and the A_{10} mean-line data presented in reference 4 should permit fairly accurate performance predictions to be made for all intermediate blade mean lines which can be derived by varying the proportions of A and I loadings.

Test measurements.- Blade pressure distribution was measured at the midspan position of the central airfoil at each angle of attack. In addition, surveys of wake total-pressure loss and turning angle were made. The methods of obtaining these measurements and the test procedure are the same as those in reference 4.

Calculations.- The calculative procedure is completely described in reference 4. For the sake of completeness, the definitions of wake, lift, and drag coefficients used in the calculations are repeated here. The wake coefficient C_{w_1} represents the momentum difference between the wake and the stream outside the wake; it is not considered to be a true drag coefficient but is used merely for convenience in assessing the wake contribution in the summation of forces. All forces due to pressure and momentum changes across the blade row were summed to obtain the resultant blade-force coefficient. The resultant force coefficient was resolved into components perpendicular and parallel to the vector mean velocity to obtain the lift coefficient C_{l_1} and the drag coefficient C_{d_1}, respectively. All coefficients are based on upstream dynamic pressure q_1.

Accuracy of results.- In general, the measured turning-angle accuracy was within $\pm 1/2°$ near the design values. The correlation procedure used was believed to have improved further the accuracy of the design values in the final results. For tests far from design, that is, near positive or negative stall, the accuracy was somewhat reduced.

The blade normal-force coefficient (the component of the resultant force coefficient perpendicular to the blade chord line) calculated from pressure rise and momentum considerations was compared with the normal-force coefficient obtained by integration of the pressure distribution. Since these values would be affected by error in turning angle, surface pressure or wake-survey readings, laminar-separation effects, or a failure to achieve two-dimensionality of the flow, this comparison is a check of the over-all acceptability of the results. The agreement between normal-force coefficients obtained by the aforementioned methods was well within 6 percent for the majority of the tests made for lift coefficients above 0.4. For lift coefficients below 0.4, the numerical comparison between normal-force coefficients was almost always well within 0.04. The accuracy of the lift coefficients is directly comparable to that of the normal-force coefficients. The lift coefficients presented were those obtained from momentum considerations. Wake-coefficient and drag-coefficient accuracy is discussed subsequently.

PRESENTATION OF RESULTS

Detailed blade-performance data for the A_2I_{8b} blades are presented in figures 7 to 30. The representative pressure distributions presented have been selected to illustrate the variation through the angle-of-attack range for each combination of C_{l_o}, β, and σ. The section characteristics presented throughout the angle-of-attack range are turning angle, lift coefficient, wake coefficient, drag coefficient, and lift-drag ratio. The effects of two types of roughness are indicated by the pressure distributions presented in figure 31 of tests made using a 1/16-inch strip of either masking tape or Scotch tape at the 35-percent-chord station on the convex surface. The effects of surface roughness on turning angle and drag coefficient over the usual angle-of-attack range at two combinations of inlet angle and solidity for the NACA 65-$(12A_2I_{8b})$10 blade section are presented in figures 32 and 33.

A comparison of the pressure distributions of the NACA 65-$(18A_2I_{8b})$10 blade section with and without the 1/16-inch masking tape is presented in figure 34. The effects of surface roughness on turning angle and drag coefficient over the usual angle-of-attack range for this blade are presented in figure 35. A comparison of the pressure distributions for the NACA 65-$(18A_2I_{8b})$10 blade section with and without No. 600 carborundum paper draped around the forward 35 percent of the blade is presented in figure 36. The effects of changes in Reynolds number and turbulence level on turning angle and drag coefficient over a Reynolds number range from 160,000 to 520,000 are presented in figure 37.

Trends of variation in section operating range, in terms of angle-of-attack range, with camber for inlet angles of 30°, 45°, and 60° at $\sigma = 1.0$ and 1.5 are presented in figure 38. Variation of experimental and ideal dynamic-pressure ratios across the cascade with turning angle and inlet angle is presented in figure 39. Figure 40 gives the relation between inlet dynamic pressure and mean dynamic pressure for convenience in converting coefficients from one reference velocity to the other.

The information most useful for selecting blade sections to fulfill compressor design vector diagrams is summarized in figures 41 to 51. The data used for the preparation of these figures were those obtained from smooth-blade tests. The variation of turning angle with angle of attack for each camber at each of the inlet air angle and solidity combinations tested is presented in figures 41 to 46. Figures 47 to 51 are design and correlation charts. The variation of design turning angle and design angle of attack with the parameters camber, inlet angle, and solidity is indicated for several combinations of the parameters to facilitate interpolations required to satisfy design velocity diagrams.

Detailed blade-performance data are presented for the A_6I_{4b} blades in figures 52 and 53 and for the A_6I_4 blades in figures 54 and 55. A comparison of the turning angles and drag coefficients for the $C_{l_o} = 1.2$ A_2I_{8b}, A_6I_{4b}, A_{10}, and A_6I_4 blade sections is presented in figures 56 and 57. Figure 58 indicates the variation in design angle of attack as distribution of mean-line loading is varied for $C_{l_o} = 1.2$. These data used in conjunction with the test data presented herein for the A_2I_{8b} blades and the data for the A_{10} blades in reference 4 for interpolation purposes should permit the utilization of a wide variety of blade mean lines (having varying proportions of A and I loadings) for design purposes.

The design pressure distributions for the A_2I_{8b}, A_6I_{4b}, and A_6I_4 mean-line blades are compared with the A_{10} blades at $\beta = 60°$ with $\sigma = 1.0$ in figures 59 to 61 and at $\beta = 45°$ with $\sigma = 1.5$ in figures 62 to 64 in order to estimate their respective high-speed-performance capabilities. The effect of angle of attack on operating inlet Mach number level is indicated in figure 65 by a comparison of low-speed pressure distributions of the A_2I_{8b} blade at $\beta = 45°$ with $\sigma = 1.5$ at design angle of attack and 3.4° above design angle of attack with estimated values of critical pressure coefficients.

DISCUSSION

Low-Speed Pressure Distribution

One purpose of this investigation was to derive new types of axial-flow compressor blade sections having low surface velocities in their forward regions. Examination of the surface pressure distributions of the NACA 65-$(C_{l_o}A_2I_{8b})$10 blade sections at design angle of attack for all combinations of inlet angle and solidity confirms that this purpose has been achieved. The $12A_2I_{8b}$ section at $\beta = 60^\circ$ and $\sigma = 1.0$ (fig. 25(c)) may be considered typical. Not only are the surface velocities low at design angle of attack but also the surface velocities remain low at angles of attack several degrees on either side of design.

Selection of Design Angle of Attack

The magnitude and shape of the blade-surface pressure distribution are important criteria for predicting the conditions of best operation at high Mach numbers. Velocity peaks occurring on either surface in low-speed tests would, of course, be accentuated at high speed, and supersonic velocities with attendant shock losses would occur at relatively low entering Mach numbers. The trend of low-speed pressure-distribution shape over the angle-of-attack range was examined for each cascade combination and the angle for which neither surface had any velocity peaks was selected as design for high-speed usage. In general, this angle is near the middle of the low drag range, indicating efficient blade-section performance for angles a few degrees above and below design. The design angle-of-attack choices are indicated by an arrow on the blade-section-characteristic plots of figures 7 to 30 and 52 to 55. They are also indicated by cross bars on the turning-angle summary curves in figures 41 to 46.

In reference 5 it has been found that at high inlet Mach numbers (Mach numbers in the transonic range) peak efficiency shifts to angles of attack which are greater by approximately 4° than those selected as design from an examination of low-speed pressure distributions. Hence, for transonic design work it may be desirable to use design angles of attack which are higher than those herein presented. Unpublished high-speed cascade tests of an NACA 65-$(12A_2I_{8b})$10 blade at $\beta = 45^\circ$ with $\sigma = 1.5$ for Mach numbers close to 0.60 indicate that the concave surface has a considerable velocity peak. This peak occurred in the region of minimum passage area. It undoubtedly results because at these conditions the blade passage is geometrically contracted, that is, A_T/A_1 is less than 1. Hence, the design angle of attack for such conditions of β, σ, M, and C_{l_o} should be 2° to 3° above that determined from

low-speed data. Additional unpublished data for the same blade at $\beta = 60^\circ$ with $\sigma = 1.0$ indicated that at Mach numbers close to 0.70 and above the design angle of attack selected from the high-speed cascade pressure distributions was some 3° above that obtained from low-speed data. Hence, the unpublished high-speed cascade data and the rotor results of reference 5 seem to indicate better performance when the A_2I_{8b} blades are operating some 2° to 4° above the design angle of attack selected from low-speed cascade pressure distributions. However, caution must be used in arbitrarily raising the design angles of attack as presented herein to ensure that the angle-of-attack operating range before positive stall is adequate.

Correlation of Design Angle of Attack and Design Turning Angle

Correlation of the design angle of attack and design turning angles over the range of camber, solidity, and inlet angle for the A_2I_{8b} blades is given by figures 47 to 51 in a manner convenient for design use. Excellent correlation is obtained. These figures were compared with similar figures presented in reference 4 and the trends were similar to those of the A_{10} blades.

Turning Angle, Angle-of-Attack Relationships

Summaries of the turning angle, angle-of-attack relationships through the camber range are given for each inlet angle and solidity in figures 41 to 46 for the A_2I_{8b} blades. The inconsistency in the shape of the curves at stall is a result of reduced measurement accuracy. For most of the combinations tested there are approximately straight-line relationships for considerable portions of the curves. Some of the curves showed a definite reduction in $d\theta/d\alpha_1$ in the region where the nature of the boundary-layer flow could very well have changed from an extensive laminar-flow region and laminar separation to an almost entirely turbulent boundary-layer flow. This condition was particularly noticeable in figures 41 and 42 for $C_{l_o} = 1.2$ and 1.8. The values of $d\theta/d\alpha_1$ for the A_2I_{8b} blades near design that can be obtained from figures 41 to 46 showed considerable variation with camber for each inlet angle and solidity condition. Hence, average values of $d\theta/d\alpha_1$ for each inlet angle and solidity condition neglecting the camber effect have not been presented. It is recommended that values of $d\theta/d\alpha_1$ for each camber under consideration be obtained directly from figures 41 to 46.

Operating Range

In order to estimate the useful operating range of the various sections at the solidity and inlet-angle conditions tested, Howell's index of twice the minimum drag (ref. 9) was used to determine the upper and lower limits of angle of attack. For some of the test configurations, the drag-coefficient change was gradual enough near the ends of the useful angle-of-attack range so that the value of minimum drag used would have some effect on the operating range value. The variation of drag coefficient with angle of attack is often erratic because the A_2I_{8b} blade is so susceptible to variation in the nature of the boundary-layer flow (early transition or extensive regions of laminar flow). This variation in the nature of the boundary-layer flow will also undoubtedly affect the minimum drag values. Hence, considerable scatter in the operating ranges obtained from an examination of twice minimum drag can be expected. Figure 38 indicates the operating ranges for the conditions tested. The dashed portions are approximate values obtained by extrapolation of the test data. A comparison of the operating range of the A_2I_{8b} blades with that of the A_{10} blades of reference 4 indicated that the ranges were generally similar.

For high angles of attack the use of twice the minimum drag as a range criteria is conservative in that the ratio of l/d may be high at twice the minimum drag. Hence, the blade-section efficiency could be fairly high at this so-called limiting range condition. Also, the range plots presented in figure 38 are for low-speed cascade tests. Operating range has been shown to change with Mach number. The high-speed rotor tests of A_2I_{8b} blades reported in reference 5 indicated efficient high-speed operation at angles of attack above the operating range indicated by the low-speed cascade tests. The rotor tests also indicated that as inlet Mach number increased the operating range on the low angle-of-attack side of design was greatly reduced. Unpublished high-speed cascade tests of an NACA 65-$\left(12A_2I_{8b}\right)$10 blade section at $\beta = 45^\circ$ and $\sigma = 1.5$ at Mach numbers close to 0.60 indicate about the same angle-of-attack operating range as the low-speed cascade data. Hence, operating range obtained in the high-speed compressor tests is not coincident with that indicated by the low-speed cascade tests or the $M = 0.60$ test just mentioned.

Pressure Rise

As stated in reference 4 the actual pressure rise occurring through a cascade is less than the ideal rise because of the "blocking effect" of the wake on the downstream flow area. For incompressible flow, the nondimensional pressure rise is equal to 1 minus the exit dynamic-pressure

ratio, that is, $\frac{\Delta p}{q_1} = 1 - \frac{q_2}{q_1}$. The actual dynamic-pressure ratio becomes higher than the ideal ratio because of blockage. The ideal dynamic-pressure ratio and the actual ratios at design turning angles for two solidities are summarized in figure 39 for the range of inlet angles tested. The dynamic-pressure ratios for individual tests are given by the short bars at the 100-percent-chord points of the pressure-distribution plots. Wake blocking effects are changed by the same Reynolds number and roughness factors which change C_{W_1}; however, the percentage change in dynamic-pressure ratio would be small.

Effects of Roughness, Reynolds Number, and Turbulence on Blade Performance

Existence of laminar boundary-layer flow and laminar separation in many cascade tests.- Laminar boundary-layer separation is characterized by a relatively flat region in the pressure distribution and the turbulent reattachment is characterized by a rapid pressure recovery just downstream of the separated region. (For further discussion of laminar separation see refs. 4 and 10.) This type of variation in the pressure distribution was noticeable in many of the pressure distributions presented in this report, for example, on the convex surface in figures 9(a) to (d), 14(a) to (d), and 18(b) to (d) and on the concave surface in figures 7(b) and (c) and 10(b) to (d). At higher angles of attack where the adverse pressure gradient on the convex surface became more severe, the boundary-layer transition from a laminar to a turbulent boundary-layer flow occurred in the forward portion of the blade and hence no laminar-separation region was observed. Obviously, erratic variations in the curves of wake and drag coefficients plotted against angle of attack will occur because of the sudden changes in the nature of the boundary-layer flow. These variations are noticeable in most of the wake and drag curves presented for the A_2I_{8b} blades. The wake and drag coefficients for the A_6I_{4b} and A_6I_4 blades (figs. 52 to 55) do not exhibit the erratic variations found in the data for the A_2I_{8b} blade section. Hence, the A_6I_4 blades are less susceptible to pronounced laminar-separation effects than are the A_2I_{8b} blades.

In many of the A_2I_{8b} tests, where the pressure distributions indicate that laminar separation exists, the values of C_{w_1} and C_{d_1} are low. (For example, see figs. 10, 11, and 13.) Hence, the amount of boundary-layer thickening that occurred in the reattachment of the laminar-separated boundary layer was not great. For some tests where the static-pressure rise was large, the laminar separation was very strong, resulting

in a thick boundary layer. For such tests, figures 18, 22, 25, 26, and 30, the values of C_{w_1} and C_{d_1} are high in the range of α where laminar separation occurred and they decrease abruptly where there is no laminar separation. Hence, it is clear that some care must be exhibited in using the absolute value of C_{d_1} in the low drag range for predicting section efficiencies in a design analysis. However, these values should be of some use for comparison purposes.

Effects of surface roughness.- A comparison of the effects of using a 1/16-inch strip of either Scotch tape or masking tape at the convex-surface 35-percent-chord point for the NACA 65-$(12A_2I_{8b})$10 blade section at $\beta = 45^\circ$ with $\sigma = 1.5$ is presented in figure 31. The no-roughness pressure distribution (fig. 21(c)) practically coincided with that corresponding to the Scotch-tape test. No significant change in pressure-distribution shape occurred with varying degrees of roughness. The masking-tape test, however, did show an increase in drag and a decrease in lift and hence a decrease in turning angle when compared with the Scotch-tape test and the no-roughness test in figure 21, both of which had practically identical values of C_{l_1}, C_{d_1}, and θ.

A comparison of the turning angles and drag coefficients obtained with roughness (the 1/16-inch masking tape) and without roughness over the usual angle-of-attack range is presented in figures 32 and 33 for the NACA 65-$(12A_2I_{8b})$10 blade. There was a 2.5° to 3.0° reduction in turning angles at the lower angles of attack when roughness was used. The drag coefficients at the lower angles increased appreciably when roughness was used.

A comparison of the pressure distributions of the NACA 65-$(18A_2I_{8b})$10 blade section at $\beta = 45^\circ$ and $\sigma = 1.0$ with and without the 1/16-inch masking tape (fig. 34) indicate that the convex-surface laminar separation has been eliminated by using roughness. The roughness did decrease the turning angles by 3.0° to 3.5° and effected an appreciable increase in drag coefficient over much of the angle-of-attack range (fig. 35). In all these comparisons of C_{d_1} with and without roughness the useful angle-of-attack range was not affected significantly by the use of roughness. However, it is not surprising that the large drag rise associated with positive and negative stall should be relatively insensitive to roughness effect since the pressure gradients on the critical surface are then so unfavorable to laminar boundary-layer flow that the boundary-layer flow must be turbulent regardless of whether roughness is used.

Figure 36 presents a comparison of the pressure distributions for the NACA 65-$(18A_2I_{8b})$10 blade section at $\beta = 30^\circ$ and $\sigma = 1.5$ with and

without No. 600 carborundum paper draped around the forward 35 percent of the blade. The carborundum paper was fairly effective in producing early boundary-layer transition and hence eliminated the laminar separation. Again, the roughness reduced the lift coefficient and turning angle although this time the roughness decreased the drag slightly.

In summation, when the roughness was sufficient to reduce or eliminate the laminar separation the drag was generally higher and the turning angle generally lower than that of the smooth-blade tests.

Effects of Reynolds number and turbulence level.- The effects of Reynolds number on drag coefficient and turning angle were investigated by testing the NACA 65-$(12A_2I_{8b})$10 blade at $\beta = 60^\circ$, $\alpha = 9.6^\circ$, and $\sigma = 1.0$ over a range of Reynolds number (fig. 37). The solid-line curves indicate that the major change in C_{d_1} with R occurred below 300,000, whereas the turning-angle variation for R between 200,000 and 520,000 was almost insignificant when the 1/2-inch-mesh turbulence screen mentioned previously is left in place. The dashed-line curves represent a reduction in turbulence level accomplished by the removal of the screen. The effect of varying the turbulence level was most pronounced at the lower Reynolds numbers. At R = 444,000, the Reynolds number at which all the cascade tests for the A_2I_{8b} blades were conducted, the effect of the increased turbulence was negligible.

Comparison of Performance of A_2I_{8b}, A_6I_{4b}, A_{10}, and A_6I_4 Blade Sections

Comparison of the low-speed cascade performance of various types of mean lines has been made by comparing the $C_{l_o} = 1.2$ turning angle and drag-coefficient data for the A_2I_{8b}, A_6I_{4b}, A_{10}, and A_6I_4 blades plotted against $\alpha - \alpha_d$. Figures 56 and 57 present the comparison at $\beta = 45^\circ$ with $\sigma = 1.5$ and $\beta = 60^\circ$ with $\sigma = 1.0$, respectively. It can be seen that at both inlet air angles at design angle of attack the variation in turning angle for the various types of loadings investigated is small. Since the loading distributions examined encompass a very wide range of loading conditions, it may be concluded that most compressor blade sections will be included in this range of loading conditions. Hence, for the same isolated airfoil lift coefficient, design turning angle may be accurately estimated for most compressor blade sections once design angle of attack is determined. Figure 58 indicates the variation in design angle of attack, as obtained from an examination of low-speed pressure distributions, as distribution of mean-line loading is varied for $C_{l_o} = 1.2$. It was obtained from tests of the A_6I_4, A_{10},

A_6I_{4b}, and A_2I_{8b} blades at $\beta = 45^\circ$ with $\sigma = 1.5$ and $\beta = 60^\circ$ with $\sigma = 1.0$. The variation in α_d is continuous and almost linear over this wide range of mean-line loading distributions. Similar trends can be expected for other cambers. Hence, the determination of design angle of attack for other cambers having varying amounts of A and I loading intermediate between the A_2I_{8b} and the A_{10} loading can be made by linear interpolation of the design-angle-of-attack data presented for the A_2I_{8b} blade sections and the data presented for the A_{10} blade sections of reference 4. Hence, the cascade data presented in this report and that presented in reference 4 will permit a fairly accurate prediction of design conditions for a wide range of mean-line shapes having the AI type of loading over the usual range of inlet air angle and solidity conditions.

At $\beta = 45^\circ$ with $\sigma = 1.5$ the operating range as indicated from an examination of twice minimum C_d in figure 56 was similar for the A_2I_{8b}, A_6I_{4b}, and A_{10} blade sections. The A_6I_4 section indicated a more gradual increase in C_d at the higher angles of attack. At $\beta = 60^\circ$ with $\sigma = 1.0$ (see fig. 57), the A_{10} blade has maximum range with the A_6I_4 blade having slightly less range. The A_2I_{8b} and A_6I_{4b} blades exhibit approximately the same operating range which is somewhat less than that of both the A_{10} and A_6I_4 blades.

Evaluation of High-Speed Performance Capabilities of the A_2I_{8b}, A_6I_{4b}, A_{10}, and A_6I_4 Series Mean Lines

General discussion.- The pressure-distribution data obtained from low-speed cascade tests can be extrapolated to high-speed conditions with sufficient accuracy for comparative purposes. For a complete description of the extrapolation method used see reference 9; however, a brief description is included herein. The low-speed average passage dynamic pressures divided by the inlet dynamic pressure are determined on a one-dimensional passage-area basis through the cascade. The passage area used intersects the blade at the surface point under consideration. The low-speed surface-pressure coefficients, based on the average passage dynamic pressures, are extrapolated in terms of the average blade-passage Mach number (obtained on a one-dimensional isentropic passage-area basis) by using the Prandtl-Glauert or Kármán-Tsien relations. This extrapolation method has been verified for turbine blades in reference 11 and for compressor blades by unpublished high-speed cascade tests. This method can be used to determine the values of low-speed surface-pressure coefficients analogous to sonic surface velocities once the passage areas are known and an inlet Mach number is assumed. Since the value of low-speed surface-pressure coefficient analogous to sonic surface velocity

is dependent on the passage areas which exist, examination of low-speed surface-pressure coefficients based on q_1 is not sufficient to evaluate the high-speed performance capabilities of a compressor blade section.

An evaluation of the high-speed performance capabilities of the various mean lines discussed in this report has been made by comparing their low-speed pressure distributions at design angle of attack. The design pressure distributions for the A_2I_{8b}, A_6I_{4b}, and A_6I_4 mean-line blades are compared with the A_{10} blade sections of reference 4 at $\beta = 60^\circ$ with $\sigma = 1.0$ in figures 59 to 61 and at $\beta = 45^\circ$ with $\sigma = 1.5$ in figures 62 to 64. The extrapolation method cannot be used effectively at inlet Mach numbers close to 1.0 because the shock waves will invalidate the use of the one-dimensional isentropic methods of obtaining average Mach numbers and the Prandtl-Glauert and Kármán-Tsien relations are not accurate near $M = 1.0$. However, it was felt that differences in predicted high-speed performance observed at moderate subsonic Mach numbers (0.70 to 0.75) would persist at higher inlet Mach numbers. Hence, the inlet Mach number selected for comparative purposes was 0.75 for the conditions of $\beta = 60^\circ$ and $\sigma = 1.0$ and was 0.70 for the conditions of $\beta = 45^\circ$ and $\sigma = 1.5$. Curves indicating the low-speed pressure coefficients analogous to sonic velocity over the convex surfaces for the inlet Mach numbers selected are presented. Such curves are hereinafter called critical-pressure-coefficient curves and are denoted as S_{crit}. The convex-surface Mach numbers estimated to occur at the inlet Mach numbers selected are also presented.

Some criterion was needed to estimate which mean line would maintain efficient operation to the highest inlet Mach number level for a particular inlet air angle and solidity condition. Therefore, the assumption was made that the blade having the lowest maximum surface Mach number and, hence, the lowest static-pressure recovery along the blade surface would operate most efficiently at high Mach number levels. One unfortunate limitation of this criterion is that the maximum surface velocity and static-pressure recovery that can be tolerated with high efficiency is undoubtedly dependent on the condition of the blade boundary layer. Hence, the location of the maximum surface Mach number is of importance. It might be that a higher surface Mach number can be tolerated at 10- or 15-percent-chord point on the convex surface than can be tolerated at the 30- or 40-percent-chord point since the boundary layer may be thinner in the more forward portion.

In addition to the effect of surface-pressure recovery limiting the inlet Mach number level possible for efficient performance, the minimum blade-passage area was previously shown to be reduced at low inlet angles and high solidities. Hence, operating Mach number level could be limited by choke flow through the minimum passage area for low inlet angle and high-solidity conditions. This effect was most pronounced for the A_2I_{8b} blades.

Comparison of A_2I_{8b}, A_6I_{4b}, and A_6I_4 mean-line blade sections at $\beta = 60^\circ$ with $\sigma = 1.0$ at low speed and at an inlet Mach number of 0.75.- A comparison of the low-speed pressure distributions in figures 59 to 61 indicated that the level of the surface velocities over the forward portion of the convex surface steadily decreased as more of the loading was distributed to the rearward portion of the blade. (The mean lines listed in order of increased rearward loading are as follows: A_6I_4, A_{10}, A_6I_{4b}, and A_2I_{8b}.) From the extrapolated local Mach number plots of figures 59 to 61, both the A_2I_{8b} and A_6I_{4b} blades have a maximum surface Mach number of 0.98, whereas that of the A_{10} blade is 1.07 and that of the A_6I_4 blade is 1.11 for an inlet Mach number of 0.75. A similar trend, of course, will exist for the magnitude of the convex-surface static-pressure recoveries. Hence, it appears that both the A_2I_{8b} and A_6I_{4b} blades should have a higher efficient operating Mach number level than the A_{10} or A_6I_4 blades. The operating level for the A_6I_4 blades should be less than that of the A_{10} blades.

Although the maximum surface Mach numbers for the A_2I_{8b} and A_6I_{4b} blades are approximately the same (0.98), the location of the maximum surface Mach number is further forward for the A_6I_{4b} blade. However, since so many of the other factors which influence shock boundary-layer interaction effects which occur at transonic inlet Mach numbers are not known, it is impossible to state which of the two mean lines, that is, the A_6I_{4b} or the A_2I_{8b}, is more desirable. It is recommended that a high-speed comparison be made to determine which of the sections has the better high-speed performance.

Comparison of A_2I_{8b}, A_6I_{4b}, A_{10}, and A_6I_4 mean-line blade sections at $\beta = 45^\circ$ and $\sigma = 1.5$ at low speed and at an inlet Mach number of 0.70.- A comparison of the low-speed pressure distributions and S_{crit} lines in figures 62 to 64 indicated that the A_2I_{8b} blade had the smallest minimum passage area. It can be seen that the effect of the passage area on S_{crit} was considerably more pronounced for the high solidity condition for this low inlet angle than for $\beta = 60^\circ$ and $\sigma = 1.0$. Although the peak pressure coefficient obtained in cascade at low speed is less for the A_2I_{8b} than that of the A_{10} (1.47 compared with 1.55), the contraction of the A_2I_{8b} passage area results in a much higher maximum surface Mach number for the A_2I_{8b} compared with that of the A_{10} (1.13 compared with 1.0 at an inlet Mach number of 0.70). Hence, the convex surface

pressure recovery will be more severe for the A_2I_{8b} than for the A_{10}. Therefore, the A_2I_{8b} blade will not exhibit as high an efficient operating Mach number level. Also, since the A_2I_{8b} blade has a smaller minimum passage area, it will choke at a lower inlet Mach number than the A_{10}.

The minimum passage area associated with the A_6I_{4b} blade section has been increased sufficiently over that of the A_2I_{8b} so that the maximum surface Mach number is subsonic at 0.96 compared with 1.13 for the A_2I_{8b} and 1.00 for the A_{10}. Hence, the convex surface pressure rise and maximum surface Mach number is least for the A_6I_{4b} blade at $\beta = 45^\circ$ with $\sigma = 1.5$. Because of the large difference in maximum surface Mach number and convex surface pressure recovery between the A_6I_{4b} and A_2I_{8b} blades, the A_6I_{4b} blade should operate efficiently to a considerably higher inlet Mach number level than the A_2I_{8b}. The A_6I_{4b} blade section should probably be capable of operating efficiently to a higher inlet Mach number level than the A_{10} blades, although how much higher can be determined only by high speed tests.

The A_6I_4 blade had the highest maximum surface Mach number and hence the most severe static-pressure recovery over the convex surface. Therefore, this section would exhibit the lowest efficient operating Mach number level and will be given no further consideration herein as a mean line for transonic operation.

At low inlet angle, high solidity conditions it appears that the A_6I_{4b} mean line should have the highest operating Mach number level. The A_2I_{8b} mean line, which was actually synthesized for conditions of $\beta = 60^\circ$ and $\sigma = 1.0$ typical of the tip region of compressor rotors, was derived at a time when the strong influence of the passage-area distribution on high-speed performance was not fully realized. Because of very low minimum passage area at low inlet angle and high solidity conditions, the A_2I_{8b} blade is not a good high-speed mean line from choking considerations as well as from considerations of maximum surface Mach number at low inlet angle and high solidity conditions.

Effect of angle of attack on operating inlet Mach number level.- As previously mentioned, peak efficiency in high-speed application occurred at higher angles of attack than those selected as design from examination of low-speed pressure distributions. Therefore, an examination of the effect of increasing angle of attack on a predicted high-speed pressure distribution was made. Figure 65 presents the A_2I_{8b} mean-line low-speed

pressure distributions and S_{crit} curves for an inlet Mach number of 0.70 at $\beta = 45^{\circ}$ and $\sigma = 1.5$ at design angle of attack and 3.4° above design angle of attack. It can be seen that increasing angle of attack has reduced the maximum surface Mach number as well as the adverse surface-pressure gradient although the leading-edge region of the convex surface is peaking. An intermediate angle of attack would have reduced the leading-edge-region velocities while still reducing the maximum convex surface velocity which occurred in the minimum passage region at the 50-percent-chord point. Hence, it appears that increasing the angle of attack by something of the order of 2° should improve the high-speed performance under these cascade conditions.

Further Comments on Blade Sections for Transonic Compressors

In summation, it appears that in selecting blade sections for high-speed and transonic operation the type of blading that should be used is dictated by the design inlet air angle, solidity, camber, and section thickness required. For conditions of low inlet angle and high solidity ($\beta = 45^{\circ}$ and $\sigma = 1.5$), it is advisable to use mean lines such as the A_6I_{4b} or A_{10} blades or some intermediate mean line which tend to keep the ratio of A_T/A_1 high in order to reduce both maximum surface Mach numbers and the surface-pressure recovery. A concurrent means of reducing maximum surface Mach numbers and surface-pressure recovery is by suitable alteration of the thickness distribution as was done in reference 6. This method tends to minimize the choking problem. For high inlet angle and low solidity conditions ($\beta = 60^{\circ}$ and $\sigma = 1.0$) where A_T/A_1 is fairly high for all three mean lines, it is advisable to use the A_2I_{8b} or A_6I_{4b} blades or some intermediate mean line for transonic operation. Unfortunately, there are not sufficient transonic test data available to indicate either the limits of surface-pressure recoveries before losses become excessive or the maximum surface velocities which can be tolerated before performance is adversely affected. Hence, it is not possible to determine which blade, that is, the A_2I_{8b} or A_6I_{4b}, would give better performance at transonic inlet Mach numbers at the higher inlet angle, lower solidity conditions.

The blades tested in this investigation employed the NACA 65-series basic thickness distribution. This thickness distribution has its maximum thickness at approximately the 40-percent-chord station. Since both minimum passage area and maximum convex surface Mach numbers invariably occurred in the forward half of the blade section, further improvement in high-speed performance might be realized by utilizing thickness distributions which have their maximum ordinate shifted rearward. The optimum blade section requires the correct combination of mean line,

thickness, and thickness distribution for the combination of inlet angle, solidity, and camber under consideration.

CONCLUDING REMARKS

The systematic low-speed cascade tests of the high-speed NACA 65-$(C_{l_o}A_2I_{8b})$10 compressor blade sections have provided design data for a wide variation of conditions. These data, when used in conjunction with the data of NACA RM L51G31, provide design data for all inlet angle and solidity conditions within the usual range of application. Summary curves have been prepared to facilitate the selection of blade sections and settings to fulfill the conditions dictated by compressor design velocity diagrams.

Comparative tests of blade sections having the same isolated airfoil lift coefficient and related but widely different mean-line loading distributions (derived with varying proportions of A and I loadings) indicated only a slight variation in turning angle at design angle of attack at the same inlet angle and solidity conditions. Hence, the data presented herein when used in conjunction with the data of NACA RM L51G31 will permit a fairly accurate prediction of design performance for most compressor blade sections since the mean lines tested are believed to encompass the practical range of compressor blade mean-line loading distributions.

A comparative evaluation of the cascade test results obtained for the mean lines investigated indicated that the NACA A_2I_{8b} and A_6I_{4b} blades should be capable of efficient operation to a higher inlet Mach number than the NACA A_{10} blades at high inlet angles and low solidities. At low inlet angles and high solidities the A_6I_{4b} blade appeared to offer better high-speed capabilities than either the A_2I_{8b} or the A_{10} blades.

Langley Aeronautical Laboratory,
National Advisory Committee for Aeronautics,
Langley Field, Va., September 21, 1953.

REFERENCES

1. Howell, A. R.: The Present Basis of Axial Flow Compresoor Design. Part I. Cascade Theory and Performance. R. & M. No. 2095, British A.R.C., 1942.

2. Carter, A. D. S.: Some Tests on Compressor Cascades of Related Aerofoils Having Different Positions of Maximum Camber. National Gas Turbine Establishment Rep. No. R.47, British Ministry of Supply, Dec. 1948.

3. Fletcher, P. J.: Low Speed Tests on Compressor Cascades of Parabolic Cambered Aerofoils. Part I - Pitch/Chord Ratio = 1.0. National Gas Turbine Establishment Memo. No. M.81, British Ministry of Supply, Mar. 1950.

4. Herrig, L. Joseph, Emery, James C., and Erwin, John R.: Systematic Two-Dimensional Cascade Tests of NACA 65-Series Compressor Blades at Low Speeds. NACA RM L51G31, 1951.

5. Savage, Melvyn, Erwin, John R., and Whitley, Robert P.: Investigation of an Axial-Flow Compressor Rotor Having NACA High-Speed Blade Sections (A_2I_{8b} Series) at Mean Radius Relative Inlet Mach Numbers up to 1.13. NACA RM L53G02, 1953.

6. Lieblein, Seymour, Lewis, George W., Jr., and Sandercock, Donald M.: Experimental Investigation of an Axial-Flow Compressor Inlet Stage Operating at Transonic Relative Inlet Mach Numbers. I - Over-All Performance of Stage With Transonic Rotor and Subsonic Stators up to Rotor Relative Inlet Mach Number of 1.1. NACA RM E52A24, 1952.

7. Abbott, Ira H., Von Doenhoff, Albert E., and Stivers, Louis S., Jr.: Summary of Airfoil Data. NACA Rep. 824, 1945. (Supersedes NACA WR-560.)

8. Erwin, John R., and Yacobi, Laura A.: Method of Estimating the Incompressible-Flow Pressure Distribution of Compressor Blade Sections at Design Angle of Attack. NACA RM L53F17, 1953.

9. Howell, A. R.: Design of Axial Compressors. Lectures on the Development of the British Gas Turbine Jet Unit Published in War Emergency Issue No. 12 of the Institution of Mechanical Engineers. A.S.M.E. Reprint, Jan. 1947, pp. 452-462.

10. Bursnall, William J., and Loftin, Laurence K., Jr.: Experimental Investigation of Localized Regions of Laminar-Boundary-Layer Separation. NACA TN 2338, 1951.

11. Dunavant, James C., and Erwin, John R.: Investigation of a Related Series of Turbine-Blade Profiles in Cascade. NACA RM L53G15, 1953.

TABLE I.- ORDINATES FOR NACA A_2I_{8b} COMPRESSOR-BLADE MEAN LINE

[Stations and ordinates in percent of chord]

$C_{l_o} = 1.0$		
Station, x	Ordinate, y	Slope, dy/dx
0	0	-------
.5	.087	0.15926
.75	.126	.15411
1.25	.201	.14824
2.5	.382	.14190
5.0	.730	.13775
7.5	1.073	.13625
10	1.412	.13530
15	2.084	.13310
20	2.741	.12958
25	3.377	.12439
30	3.982	.11737
35	4.547	.10839
40	5.062	.09732
45	5.517	.08400
50	5.898	.06818
55	6.193	.04951
60	6.388	.02752
65	6.461	.00149
70	6.394	-.02973
75	6.153	-.06825
80	5.690	-.12130
85	4.927	-.18259
90	3.852	-.24939
95	2.382	-.34815
100	0	-------
Slope of radius through L.E.: 0.1593		
Slope of radius through T.E.: -0.6402		

TABLE II.- COORDINATES FOR NACA 65-$\left(4A_2I_{8b}\right)$10 COMPRESSOR BLADE SECTION

[Stations and ordinates in percent of chord]

Upper surface		Lower surface	
x	y	x	y
0	0	0	0
.451	.805	.549	-.736
.693	.981	.807	-.880
1.181	1.247	1.319	-1.087
2.411	1.724	2.589	-1.419
4.880	2.466	5.120	-1.882
7.356	3.072	7.644	-2.214
9.836	3.600	10.164	-2.471
14.805	4.494	15.195	-2.827
19.785	5.234	20.215	-3.041
24.776	5.848	25.224	-3.147
29.777	6.347	30.223	-3.162
34.782	6.738	35.218	-3.100
39.806	7.017	40.194	-2.967
44.834	7.167	45.166	-2.753
49.869	7.169	50.131	-2.451
54.911	7.006	55.089	-2.052
59.954	6.715	60.046	-1.604
64.998	6.339	65.002	-1.171
70.040	5.907	70.040	-.792
75.080	5.405	74.920	-.483
80.123	4.813	79.877	-.261
85.156	5.000	84.844	-.159
90.172	3.262	89.828	-.181
95.183	2.265	94.817	-.360

L.E. radius: 0.667
Slope of radius through L.E.: 0.064
T. E. radius: 1.000
Slope of radius through T.E.: -0.256

TABLE III.- COORDINATES FOR NACA 65-$(8A_2I_{8b})$10 COMPRESSOR BLADE SECTION

[Stations and ordinates in percent of chord]

Upper surface		Lower surface	
x	y	x	y
0	0	0	0
.403	.826	.597	-.696
.637	1.026	.863	-.824
1.125	1.322	1.375	-1.000
2.324	1.866	2.676	-1.254
4.763	2.748	5.237	-1.580
7.215	3.490	7.785	-1.773
9.675	4.152	10.325	-1.893
14.614	5.313	15.386	-1.978
19.588	6.314	20.412	-1.928
24.556	7.183	25.444	-1.779
29.557	7.924	30.444	-1.554
34.576	8.543	35.424	-1.268
39.620	9.031	40.380	-.931
44.668	9.365	45.332	-.538
49.739	9.523	50.262	-.087
54.821	9.481	55.179	.428
59.909	9.270	60.092	.952
64.995	8.924	65.005	1.414
70.079	8.464	69.921	1.766
75.161	7.862	74.839	1.981
80.244	7.080	79.756	2.024
85.305	6.053	84.695	1.828
90.332	4.778	89.668	1.385
95.342	3.182	94.658	.629

L.E. radius: 0.667
Slope of radius through L.E.: 0.127
T.E. radius: 1.000
Slope of radius through T.E.: -0.512

TABLE IV.- COORDINATES FOR NACA 65-$(12A_2I_{8b})$10 COMPRESSOR BLADE SECTION

[Stations and ordinates in percent of chord]

Upper surface		Lower surface	
x	y	x	y
0	0	0	0
.355	.862	.645	-.654
.581	1.067	.919	-.765
1.045	1.392	1.455	-.910
2.236	2.010	2.764	-1.094
4.645	3.024	5.355	-1.272
7.073	3.900	7.927	-1.324
9.505	4.694	10.495	-1.306
14.422	6.121	15.578	-1.119
19.363	7.383	20.637	-.805
24.326	8.506	25.674	-.402
29.336	9.491	30.664	.064
34.365	10.339	35.635	.573
39.421	11.036	40.579	1.112
44.502	11.558	45.498	1.682
49.608	11.873	50.392	2.281
54.731	11.917	55.269	2.945
59.863	11.810	60.137	3.522
64.993	11.497	65.007	4.009
70.119	11.011	69.881	4.335
75.240	10.309	74.760	4.454
80.365	9.336	79.635	4.320
85.456	7.993	84.544	3.829
90.495	6.278	89.504	2.967
95.511	4.082	94.489	1.635
100.000	0	100.000	0

L.E. radius: 0.667
Slope of radius through L.E.: 0.191
T.E. radius: 1.000
Slope of radius through T.E.: -0.768

TABLE V.- COORDINATES FOR NACA 65-$(18A_2I_{8b})$10 COMPRESSOR BLADE SECTION

[Stations and ordinates in percent of chord]

Upper surface		Lower surface	
x	y	x	y
0	0	0	0
.287	.899	.713	-.586
.501	1.125	.999	-.671
.949	1.491	1.551	-.768
2.110	2.213	2.890	-.837
4.476	3.427	5.524	-.799
6.870	4.502	8.130	-.639
9.281	5.495	10.719	-.412
14.146	7.316	15.854	.186
19.059	8.969	20.941	.899
24.016	10.473	25.984	1.684
29.016	11.823	30.984	2.509
34.057	13.018	35.943	3.352
39.138	14.033	40.862	4.191
44.258	14.838	45.742	5.023
49.414	15.393	50.586	5.840
54.598	15.660	55.402	6.635
59.794	15.655	60.206	7.345
64.990	15.385	65.010	7.875
70.179	14.854	69.821	8.164
75.359	13.997	74.641	8.151
80.542	12.724	79.459	7.760
85.667	10.895	84.333	6.839
90.709	8.512	89.291	5.355
95.704	5.410	94.297	3.165

L.E. radius: 0.667
Slope of radius through L.E.: 0.2858
T.E. radius: 1.000
Slope of radius through T.E.: -1.152

TABLE VI.- ORDINATES FOR NACA A_6I_{4b}

COMPRESSOR-BLADE MEAN LINE

[Stations and ordinates in percent of chord]

$C_{l_o} = 1.0$		
Station, x	Ordinate, y	Slope, dy/dx
0	0	-----
.5	.168	0.291
.75	.238	.271
1.25	.368	.248
2.5	.656	.217
5.0	1.155	.186
7.5	1.596	.168
10	1.999	.155
15	2.725	.136
20	3.360	.120
25	3.926	.105
30	4.421	.092
35	4.848	.079
40	5.209	.064
45	5.496	.050
50	5.707	.034
55	5.834	.016
60	5.871	-.002
65	5.806	-.024
70	5.627	-.048
75	5.314	-.077
80	4.835	-.116
85	4.146	-.160
90	3.219	-.212
95	1.981	-.292
100	0	-----
Slope of radius through L.E.: 0.2902		
Slope of radius through T.E.: -0.5307		

TABLE VII.- COORDINATES FOR NACA 65-$(12A_6I_{4b})10$

COMPRESSOR BLADE SECTION

[Stations and ordinates in percent of chord]

Convex surface		Concave surface	
x	y	x	y
0	0	0	0
.245	.931	.754	-.527
.462	1.172	1.038	-.600
.917	1.562	1.583	-.678
2.103	2.311	2.897	-.735
4.526	3.512	5.474	-.738
6.977	4.510	8.023	-.680
9.444	5.387	10.556	-.591
14.409	6.888	15.591	-.348
19.410	8.134	20.590	-.068
24.437	9.179	25.563	.243
29.478	10.036	30.522	.574
34.535	10.720	35.465	.916
39.618	11.232	40.382	1.270
44.703	11.549	45.297	1.641
49.803	11.656	50.196	2.040
54.913	11.530	55.087	2.472
60.010	11.192	59.990	2.900
65.108	10.709	64.892	3.225
70.192	10.086	69.808	3.418
75.270	9.302	74.730	3.452
80.349	8.312	79.651	3.292
85.402	7.068	84.598	2.882
90.426	5.537	89.574	2.187
95.438	3.629	94.562	1.127
100.000	0	100.000	0

L.E. radius: 0.667
Slope of radius through L.E.: 0.348
T.E. radius: 1.000
Slope of radius through T.E.: -0.637

TABLE VIII.- ORDINATES FOR NACA A_6I_4

COMPRESSOR-BLADE MEAN LINE

[Stations and ordinates in percent of chord]

$C_{l_o} = 1.0$		
Station, x	Ordinate, y	Slope, dy/dx
0	0	------
.5	.316	0.531
.75	.442	.489
1.25	.674	.438
2.5	1.170	.365
5.0	1.981	.292
7.5	2.649	.246
10	3.219	.212
15	4.146	.160
20	4.835	.116
25	5.314	.077
30	5.627	.048
35	5.806	.024
40	5.871	.002
45	5.834	-.016
50	5.707	-.034
55	5.495	-.050
60	5.209	-.064
65	4.848	-.079
70	4.421	-.092
75	3.926	-.105
80	3.360	-.120
85	2.725	-.136
90	1.999	-.155
95	1.155	-1.86
100	0	------
Slope of radius through L.E.: 0.5307 Slope of radius through T.E.: -0.2902		

TABLE IX.- COORDINATES FOR NACA 65-$(12A_6I_4)$10 COMPRESSOR BLADE SECTION

[Stations and ordinates in percent of chord]

Convex surface		Concave surface	
x	y	x	y
0	0	0	0
.085	1.030	.915	-.279
.278	1.334	1.222	-.273
.706	1.844	1.794	-.226
1.869	2.846	3.231	-.038
4.280	4.432	5.720	.323
6.750	5.717	8.250	.640
9.251	6.809	10.749	.917
14.309	8.575	15.691	1.375
19.429	9.905	20.571	1.699
24.586	10.861	25.414	1.893
29.726	11.505	30.274	2.000
34.858	11.889	35.142	2.045
39.988	12.041	40.012	2.049
45.095	11.963	44.905	2.039
50.196	11.656	49.804	2.040
55.271	11.116	54.729	2.072
60.318	10.385	59.683	2.117
65.354	9.545	64.646	2.090
70.367	8.625	69.634	1.985
75.367	7.625	74.633	1.797
80.361	6.540	79.639	1.524
85.343	5.373	84.657	1.167
90.316	4.098	89.684	.700
95.289	2.680	94.711	.092
100.000	0	100.000	0

L.E. radius: 0.667
Slope of radius through L.E.: 0.637
T.E. radius: 1.000
Slope of radius through T.E.: -0.348

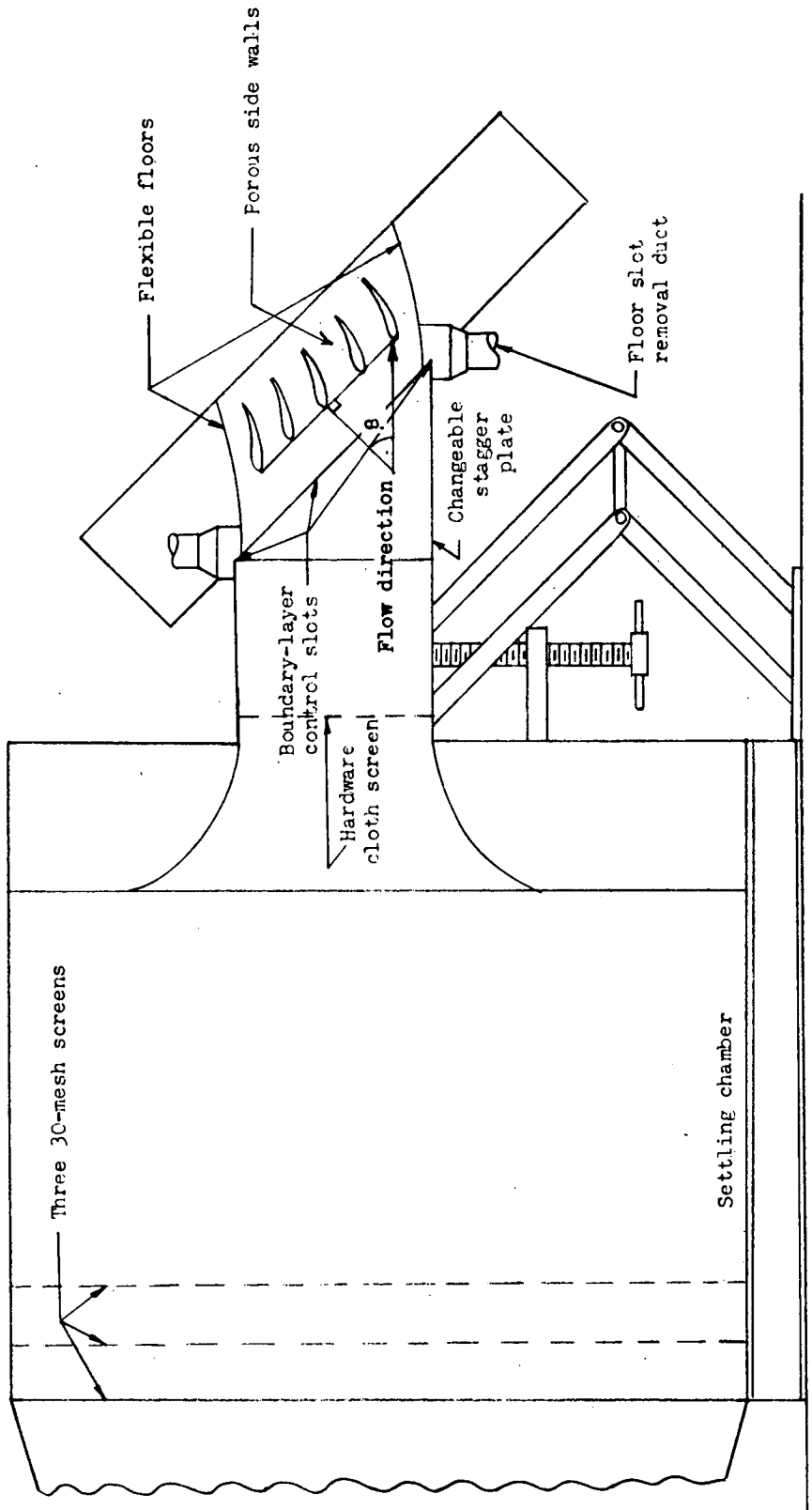

Figure 1.- Vertical cross section of two-dimensional low-speed cascade tunnel.

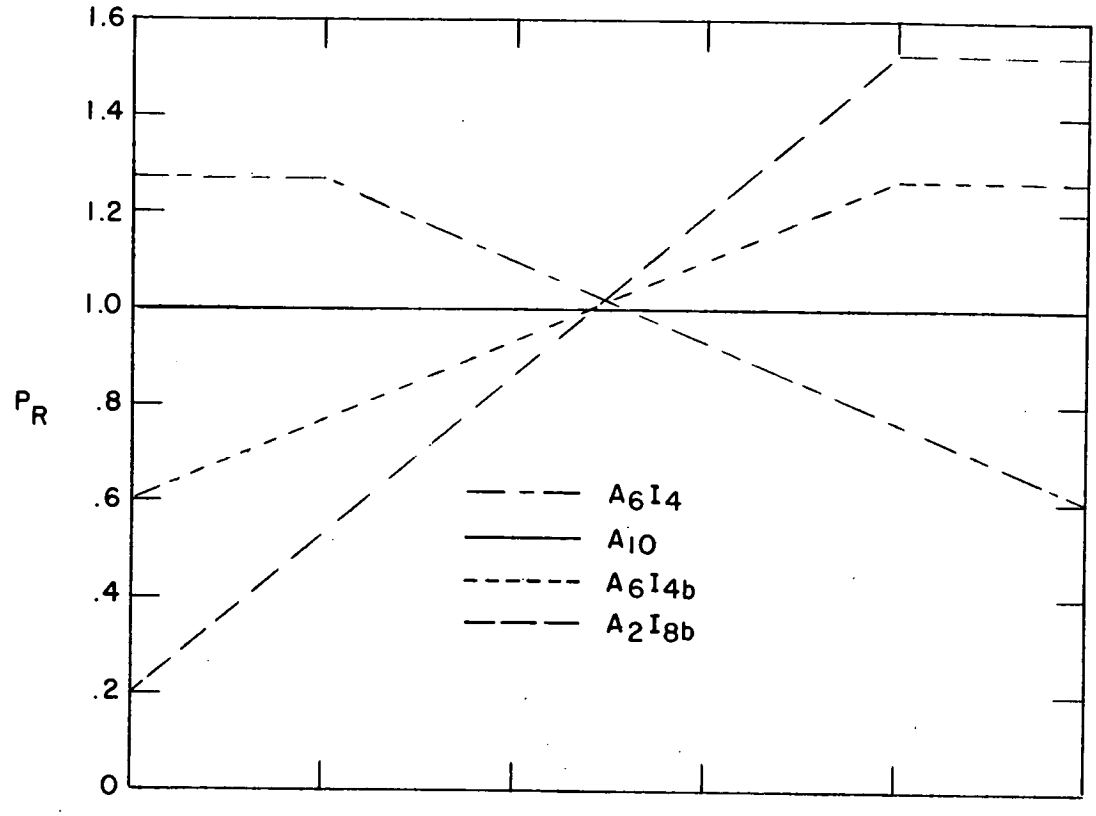

(a) Loading diagrams for $C_{l_o} = 1.0$.

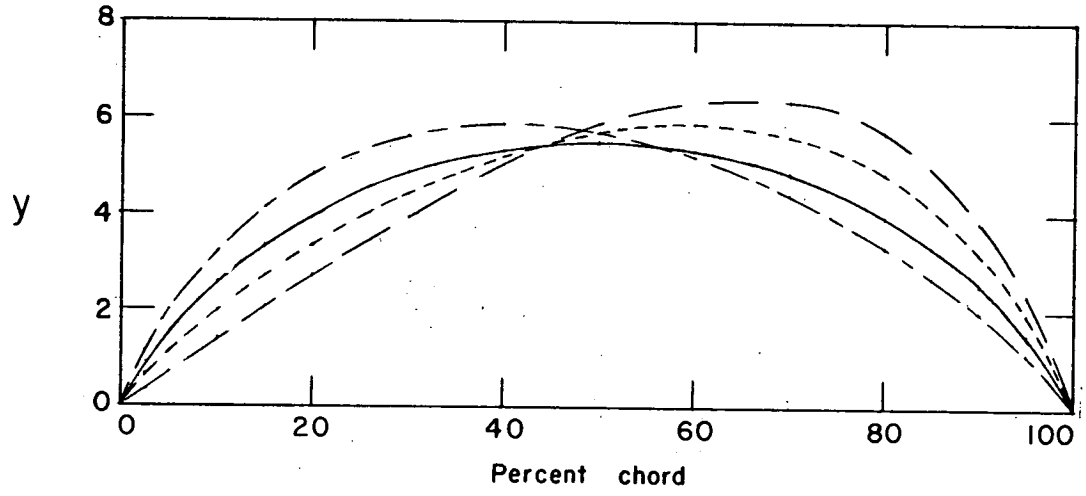

(b) Mean lines for $C_{l_o} = 1.0$.

Figure 2.- Illustration of various mean lines, loading diagrams, and blade sections tested.

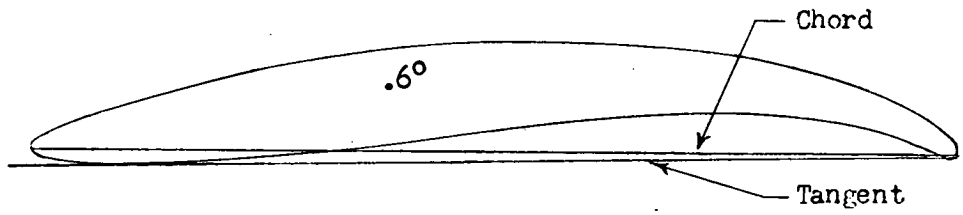

NACA 65-($12A_2I_{8b}$)10

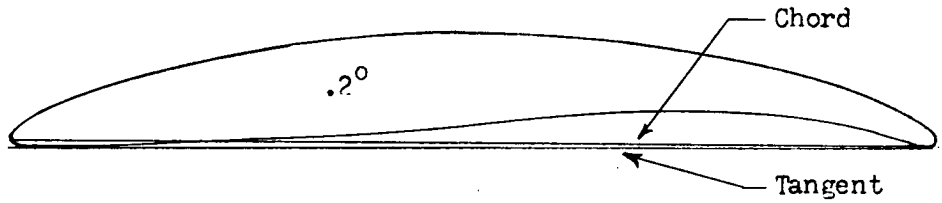

NACA 65-($12A_6I_{4b}$)10

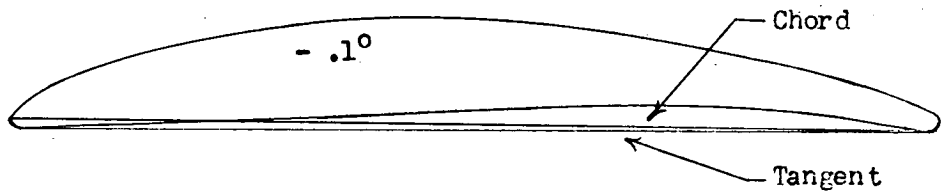

NACA 65-($12A_{10}$)10

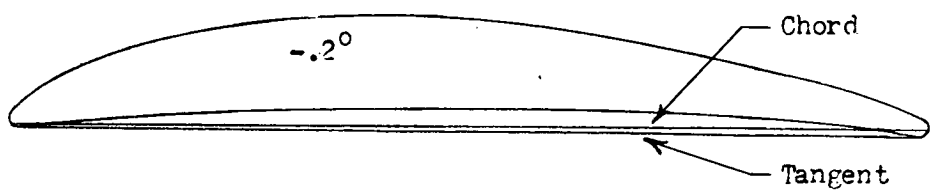

NACA 65-($12A_6I_4$)10

(c) Blade sections for A_2I_{8b}, A_6I_{4b}, A_{10}, and A_6I_4 mean lines used in conjunction with NACA 65-010 thickness distribution. Angle between chord line and tangent to concave surface is shown for various sections.

Figure 2.- Concluded.

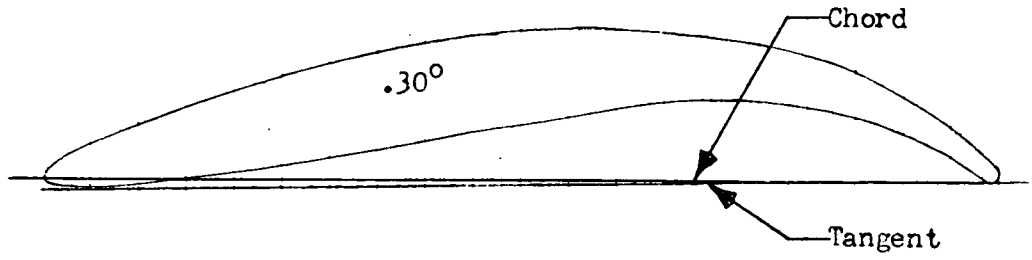

NACA 65-(18A_2I_{8b})10

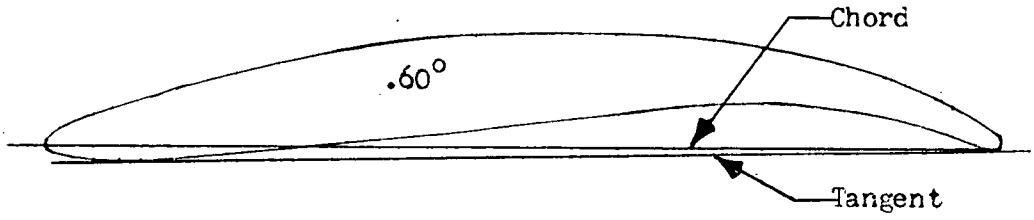

NACA 65-(12A_2I_{8b})10

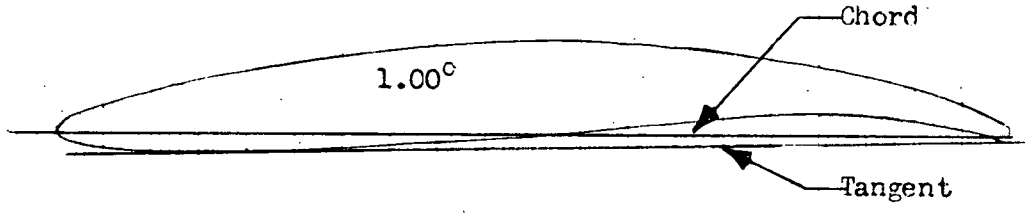

NACA 65-(8A_2I_{8b})10

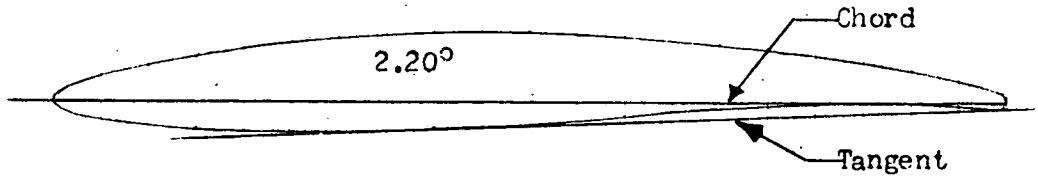

NACA 65-(4A_2I_{8b})10

Figure 3.- Blade sections tested in this investigation. Angle between chord line and tangent to concave surface is shown for various sections.

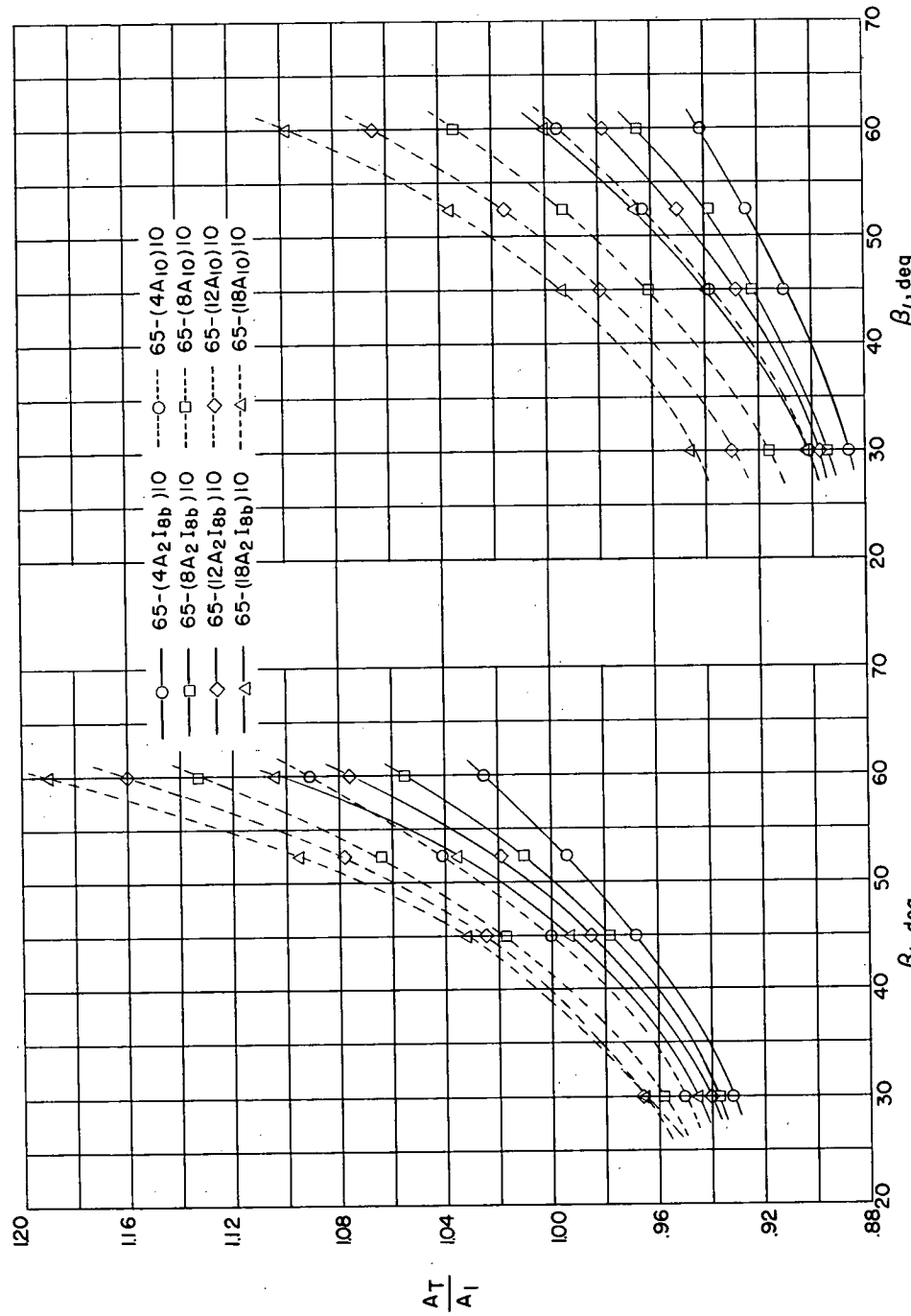

(a) $\sigma = 1.0$. (b) $\sigma = 1.5$.

Figure 4.- Ratio of blade-passage throat area to area of upstream flow over a range of inlet angles for A_{10} and A_2I_{8b} blade sections of various cambers at α_d.

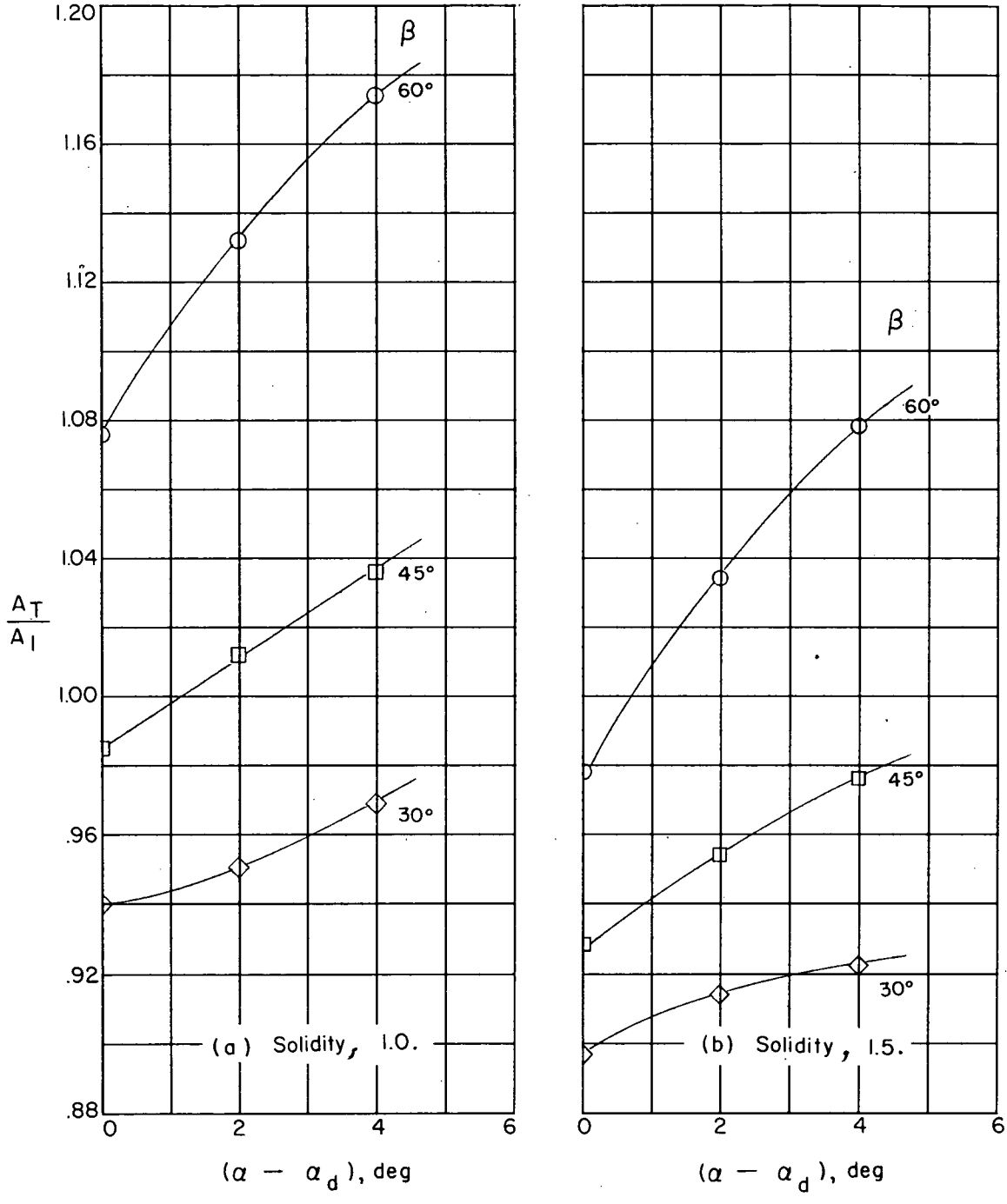

Figure 5.- Variation of ratio of blade-passage throat area to area of upstream flow with angle of attack for NACA 65-$\left(12A_2I_{8b}\right)$10 blade section at several inlet air angles.

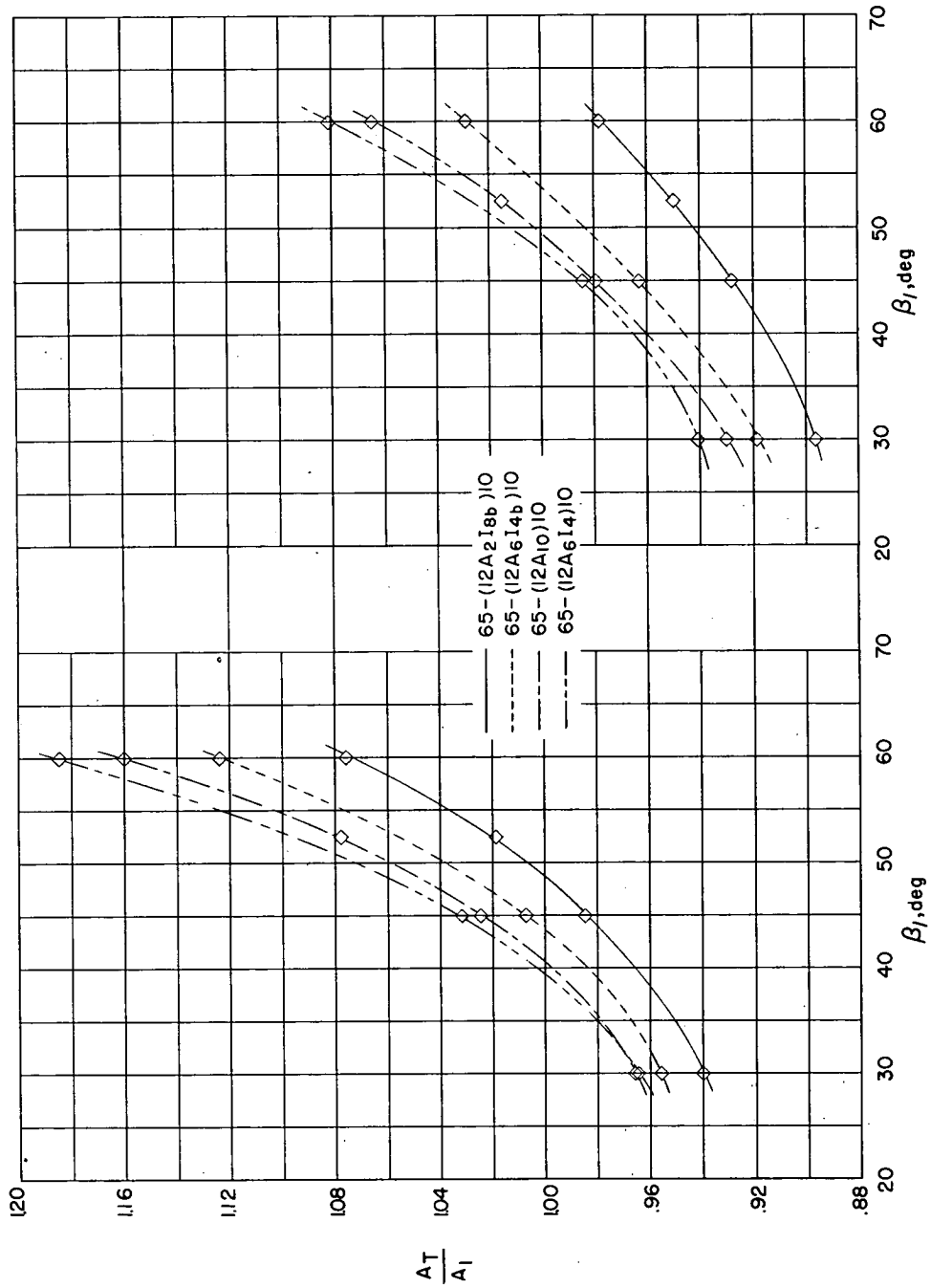

(a) $\sigma = 1.0$. (b) $\sigma = 1.5$.

Figure 6.- Ratio of blade-passage throat area to area of upstream flow over a range of inlet angles for various sections of one camber at α_q.

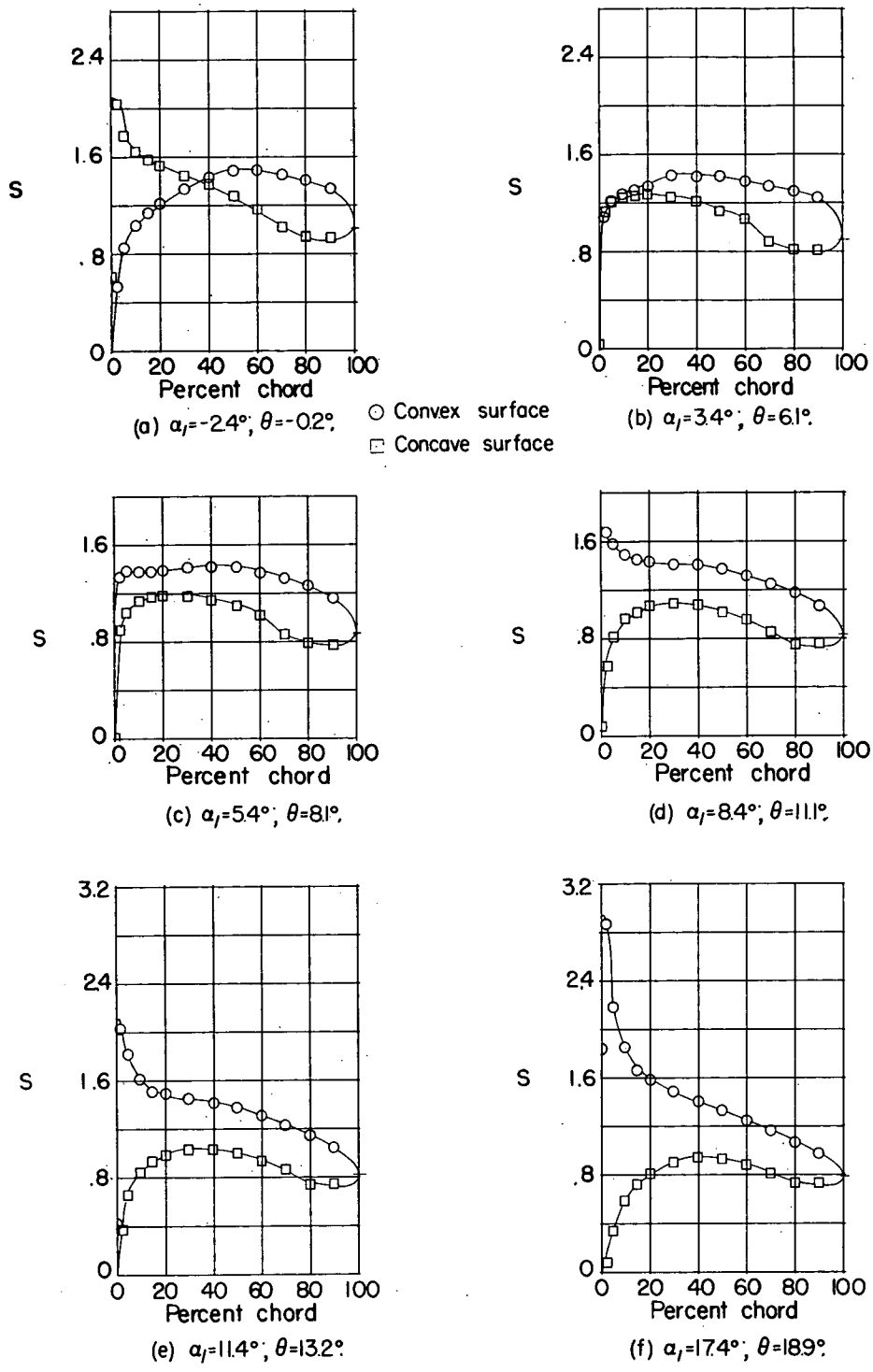

Figure 7.- Blade-surface pressure distributions and blade-section characteristics for the cascade combination $\beta_1 = 30^\circ$ and $\sigma = 1.0$ and NACA 65-$(4A_2I_{8b})$10 blade section.

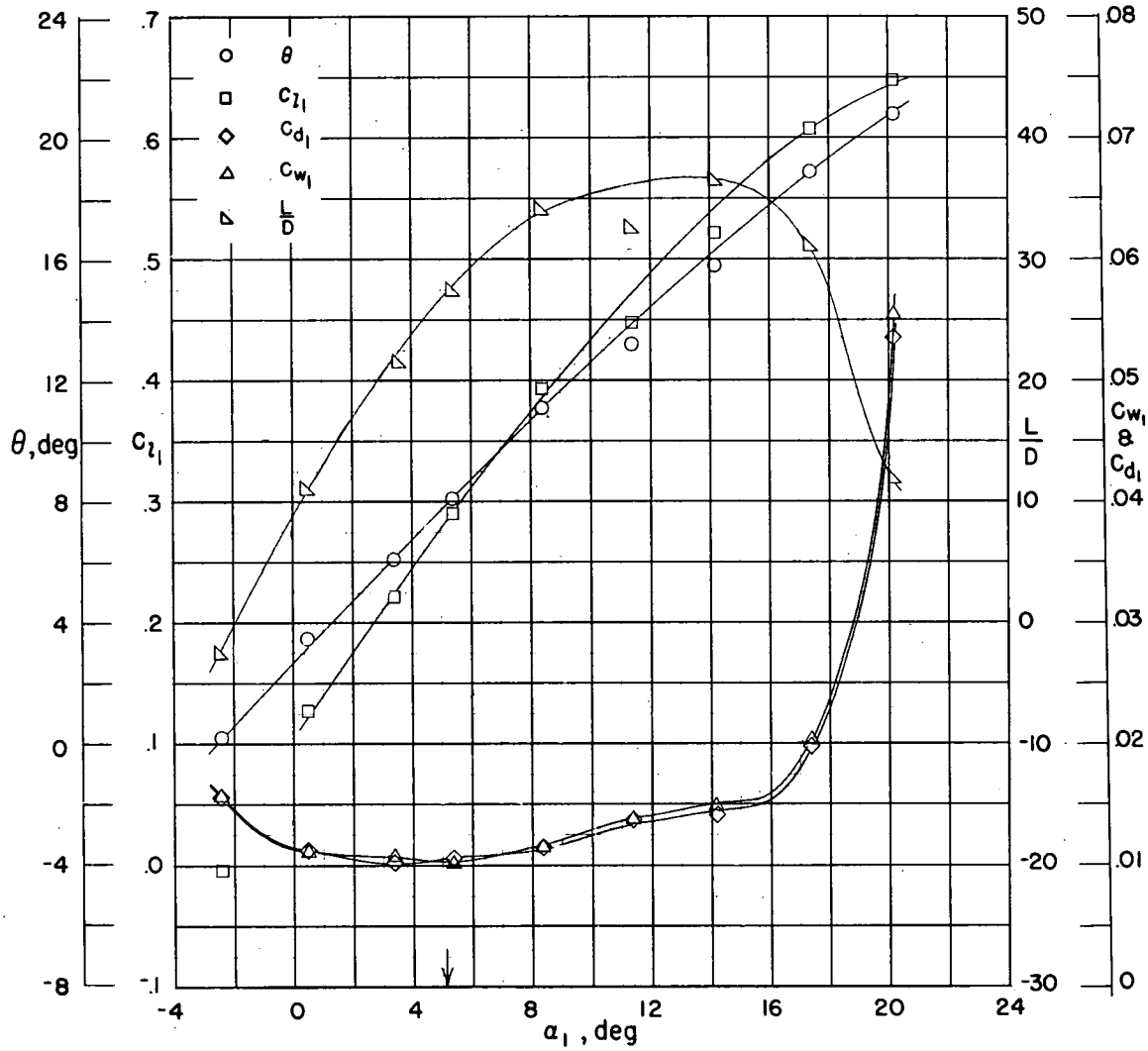

(g) Section characteristics. Arrow shows design angle of attack.

Figure 7.- Concluded.

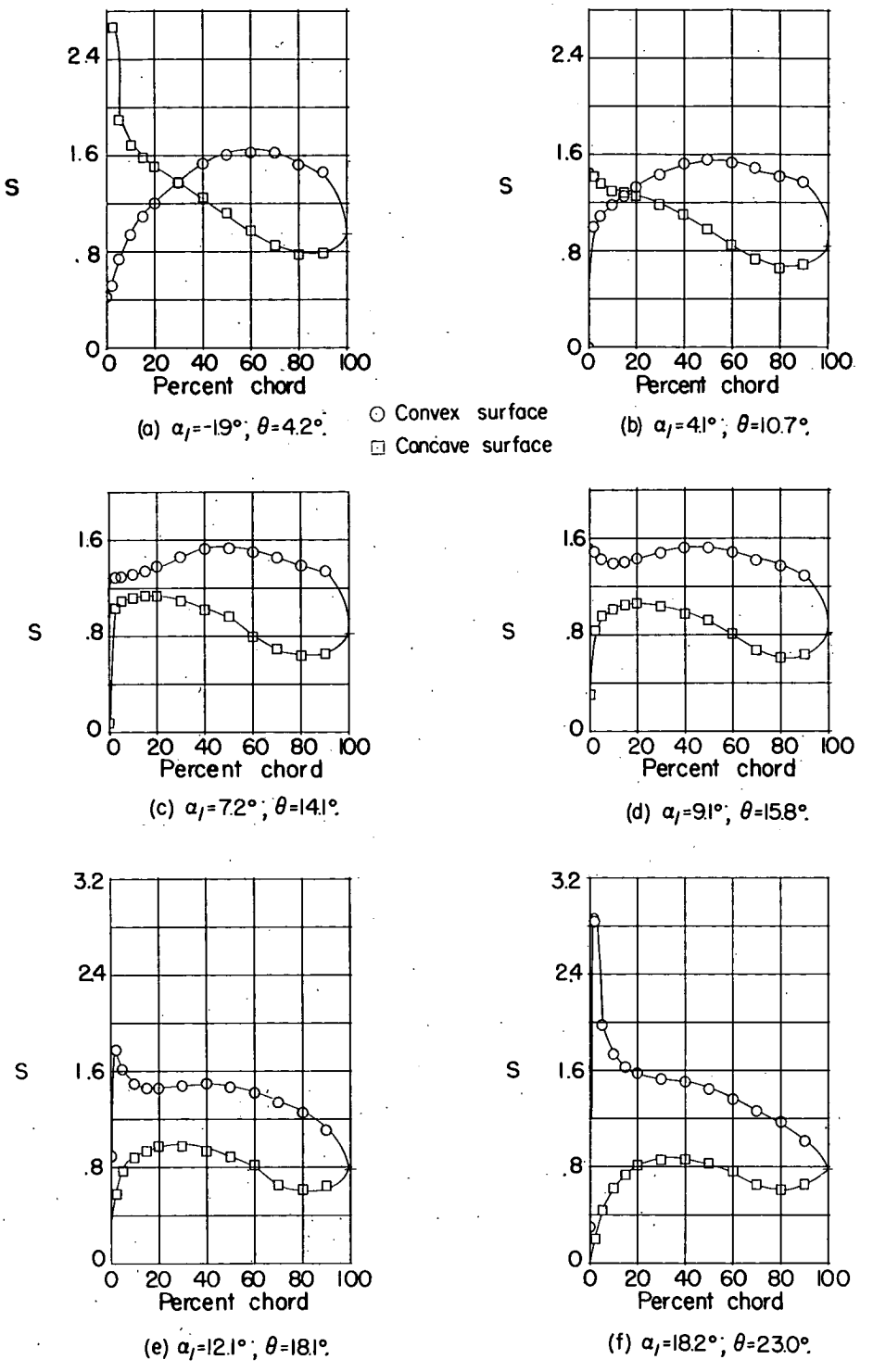

Figure 8.- Blade-surface pressure distributions and blade-section characteristics for the cascade combination $\beta_1 = 30^\circ$ and $\sigma = 1.0$ and NACA 65-$\left(8A_2I_{8b}\right)$10 blade section.

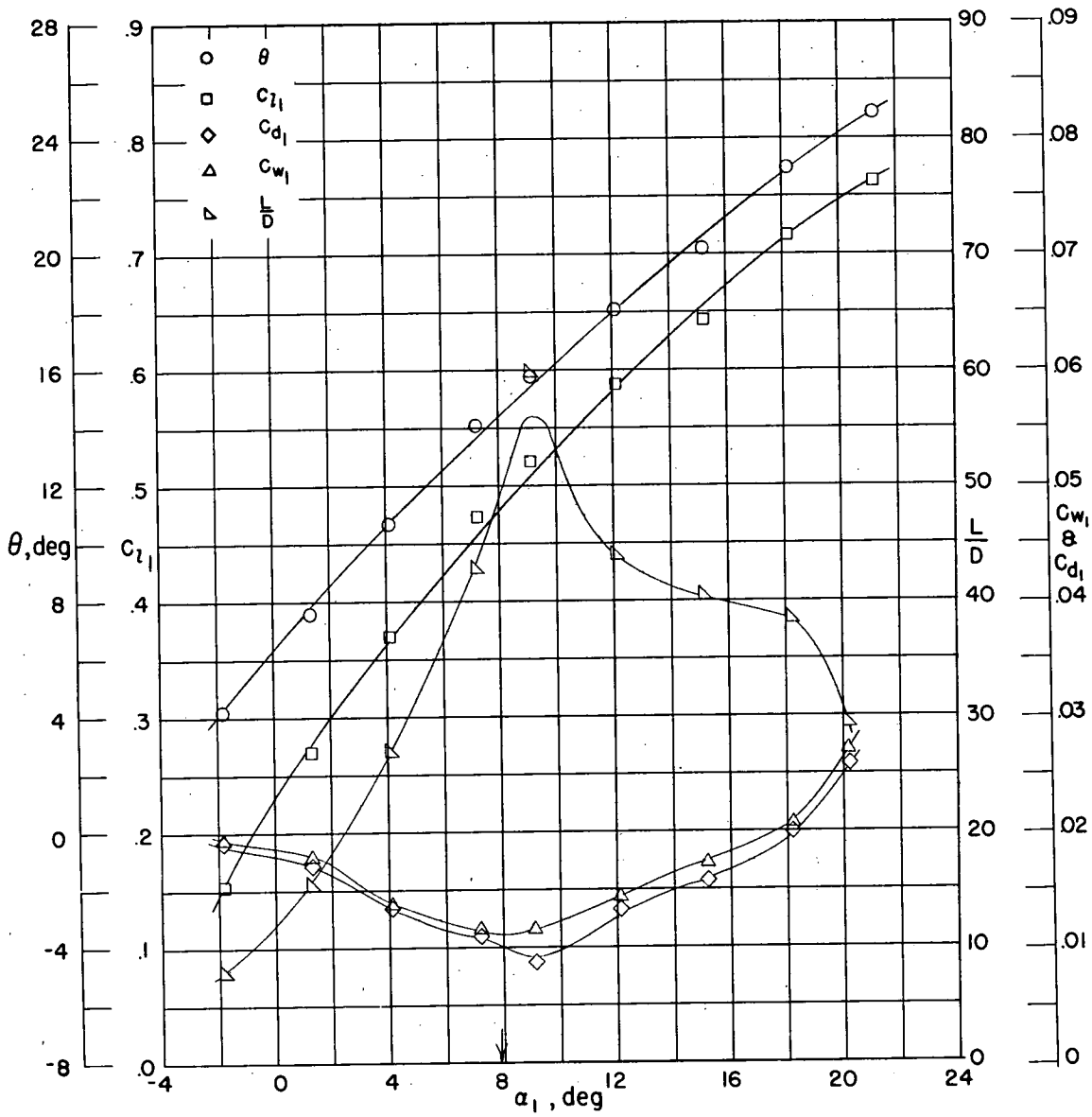

(g) Section characteristics. Arrow shows design angle of attack.

Figure 8.- Concluded.

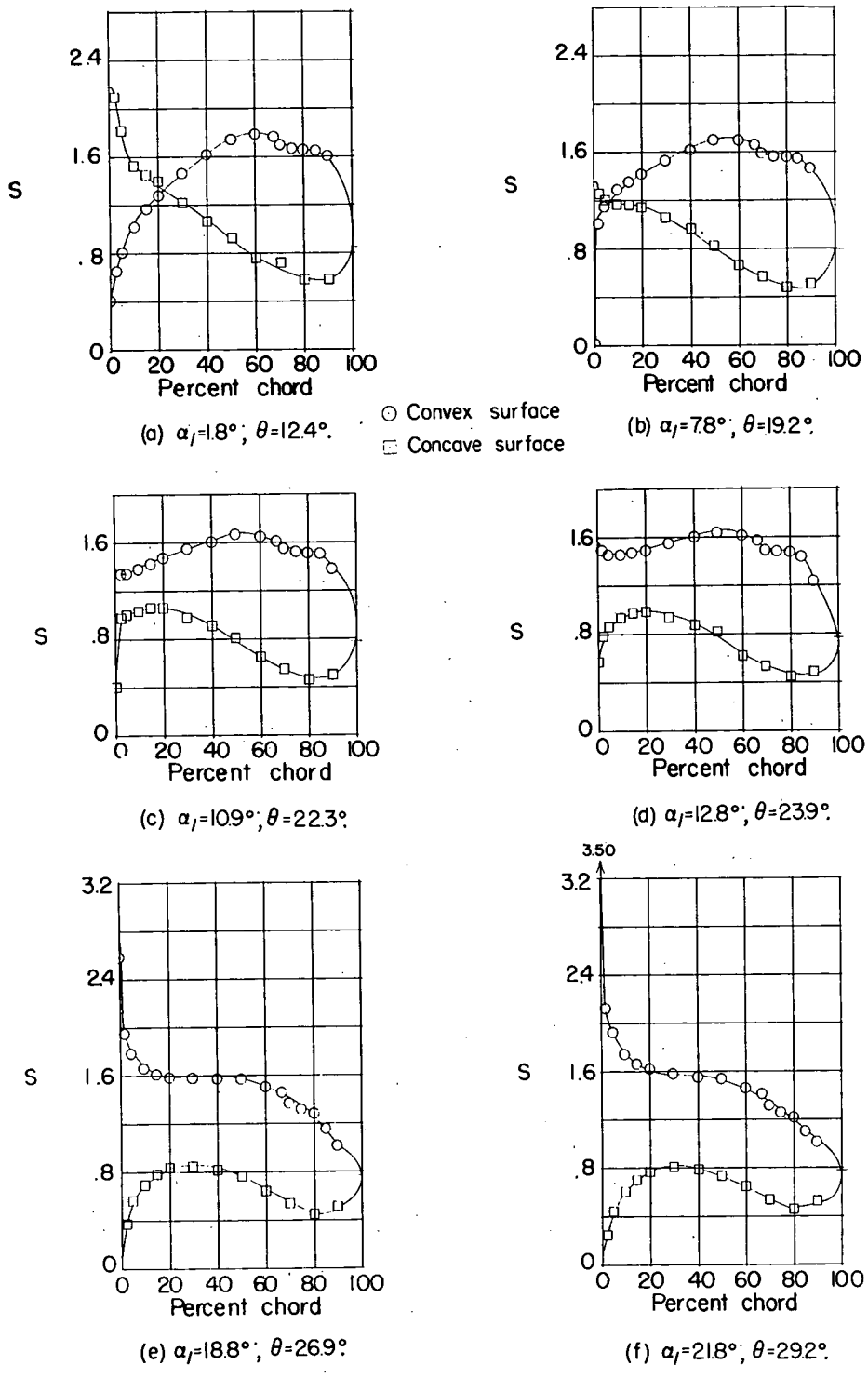

Figure 9.- Blade-surface pressure distributions and blade-section characteristics for the cascade combination $\beta_1 = 30^\circ$ and $\sigma = 1.0$ and NACA 65-$\left(12A_2I_{8b}\right)$10 blade section.

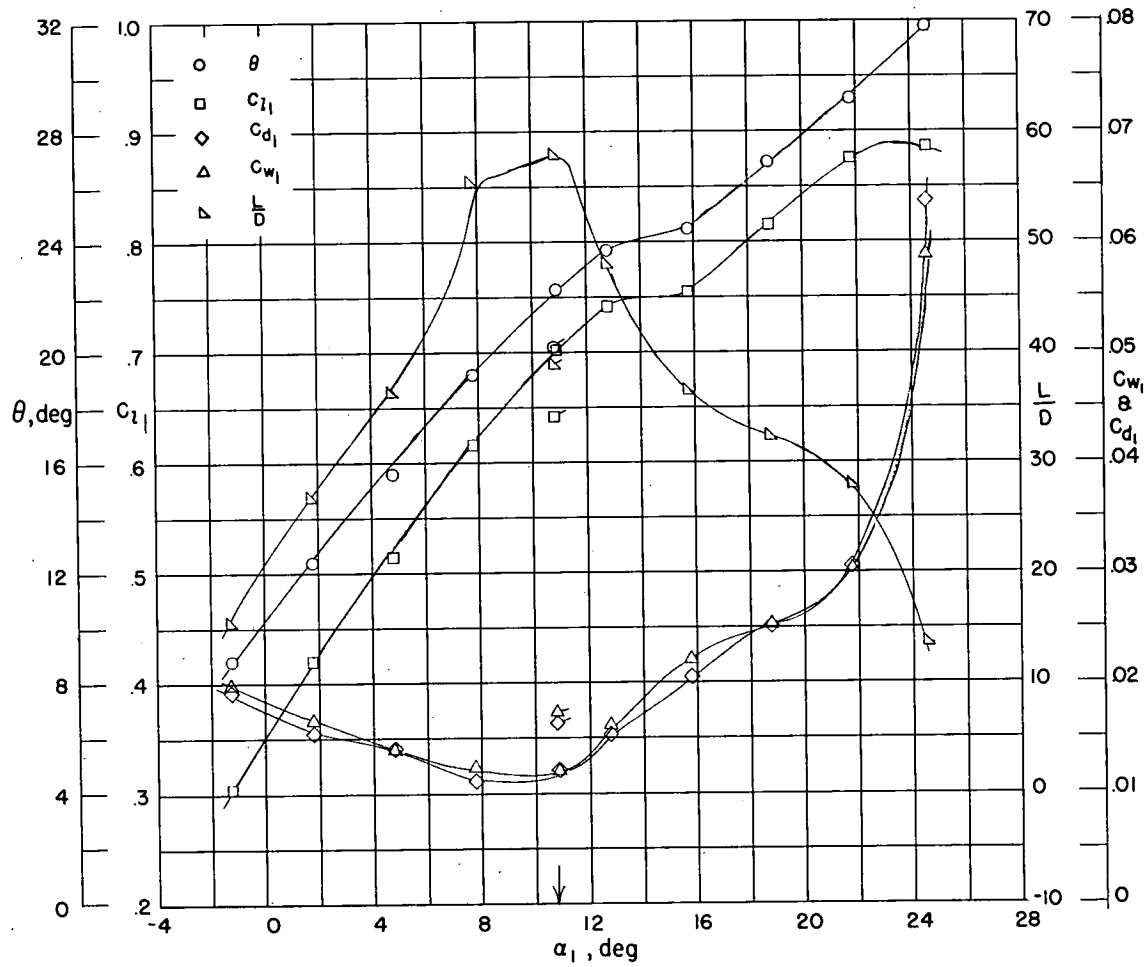

(g) Section characteristics. Arrow shows design angle of attack; flagged symbol indicates roughness.

Figure 9.- Concluded.

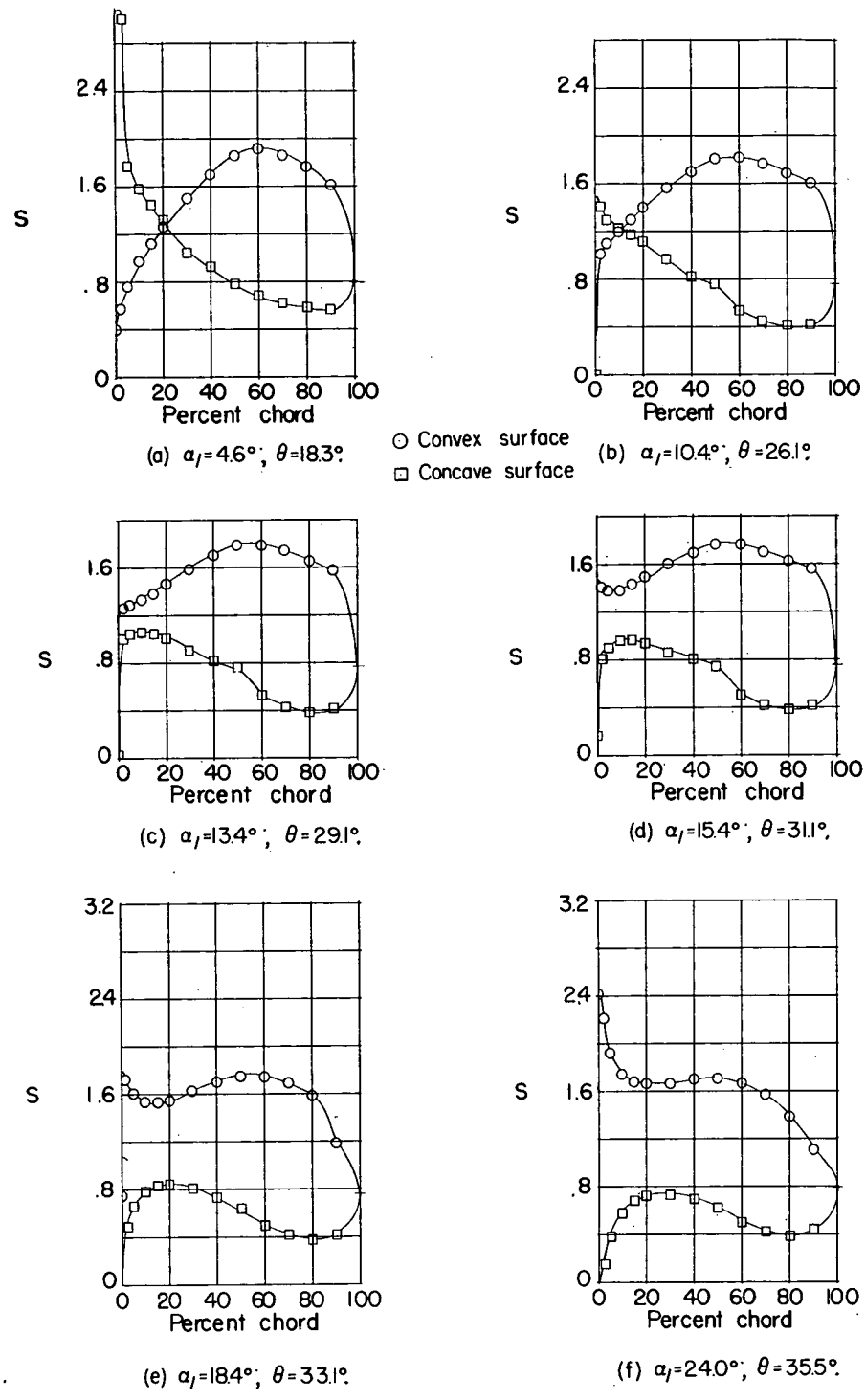

Figure 10.- Blade-surface pressure distributions and blade-section characteristics for the cascade combination $\beta_1 = 30^\circ$ and $\sigma = 1.0$ and NACA 65-$(18A_2I_{8b})$10 blade section.

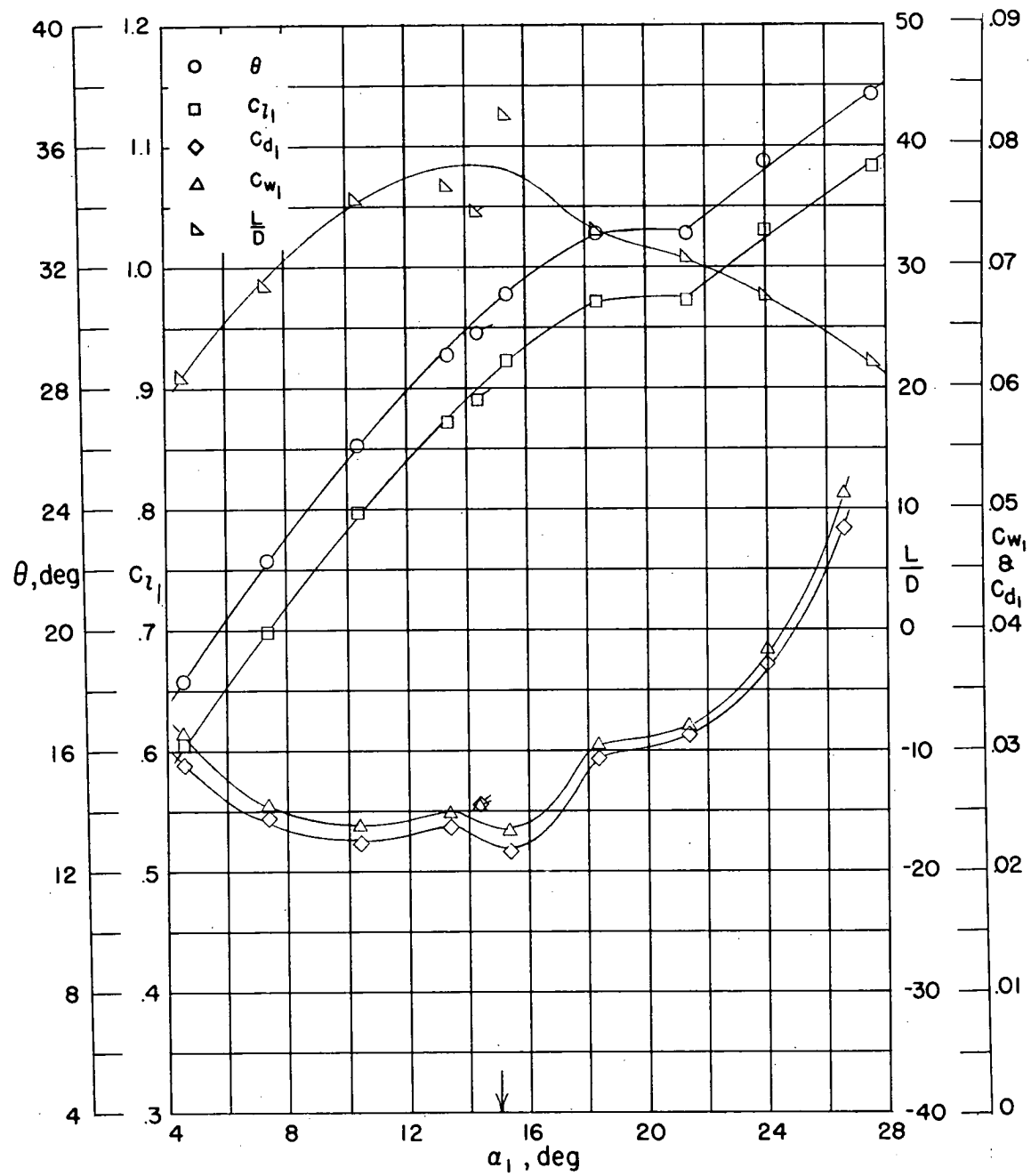

(g) Section characteristics. Arrow shows design angle of attack; flagged symbol indicates roughness.

Figure 10.- Concluded.

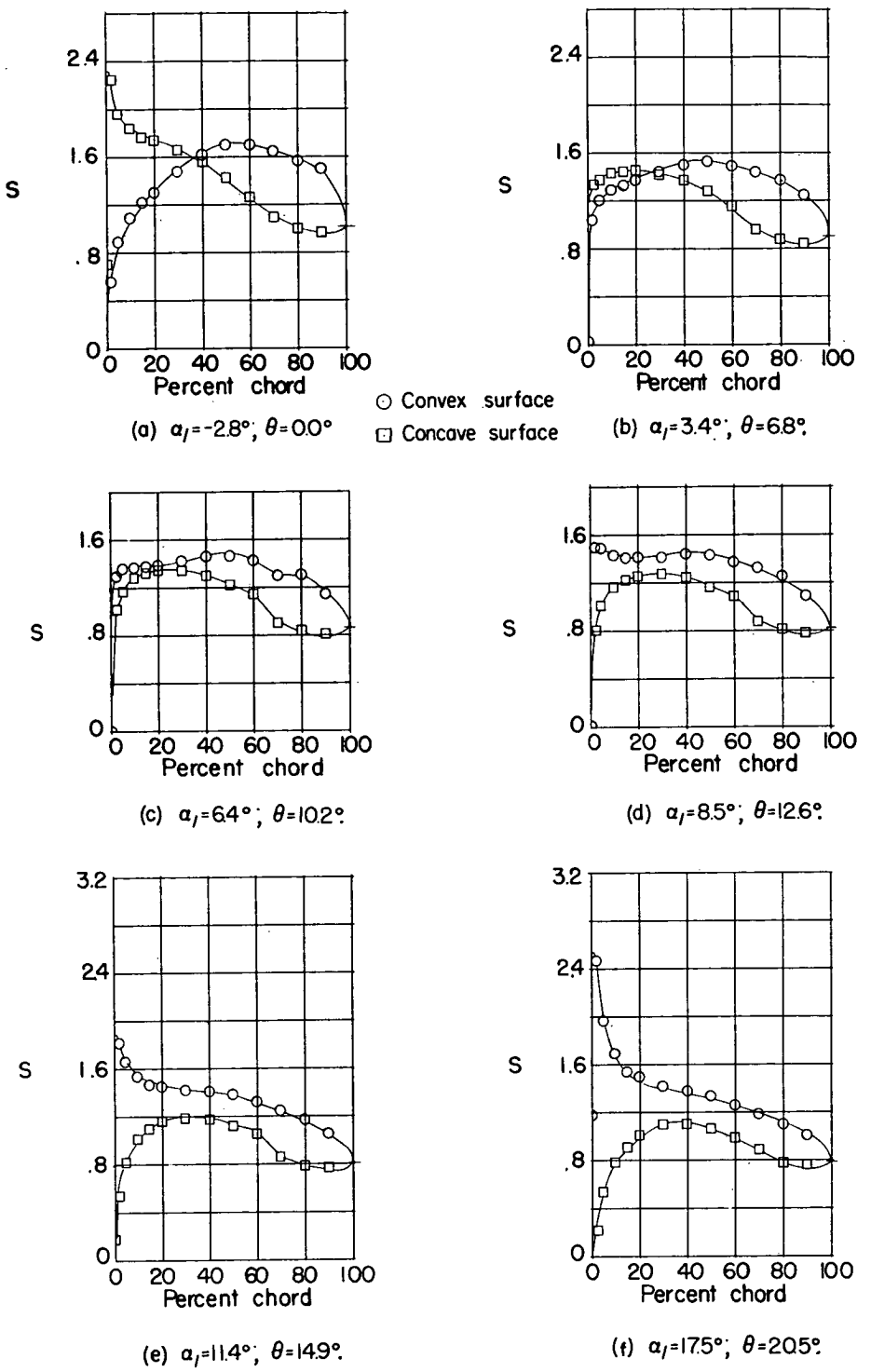

Figure 11.- Blade-surface pressure distributions and blade-section characteristics for the cascade combination $\beta_1 = 30^\circ$ and $\sigma = 1.5$ and NACA 65-$(4A_2I_{8b})$10 blade section.

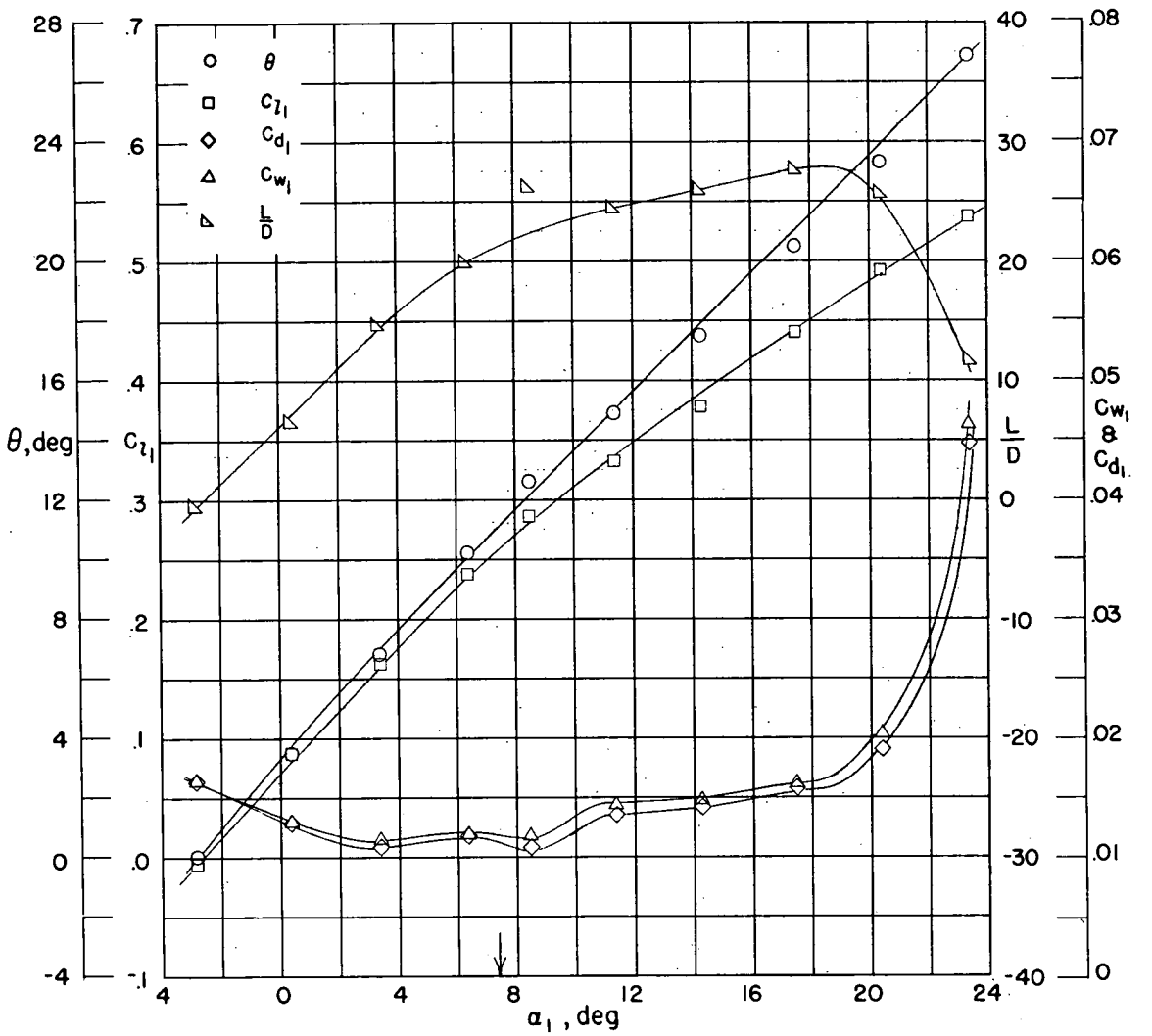

(g) Section characteristics. Arrow shows design angle of attack.

Figure 11.- Concluded.

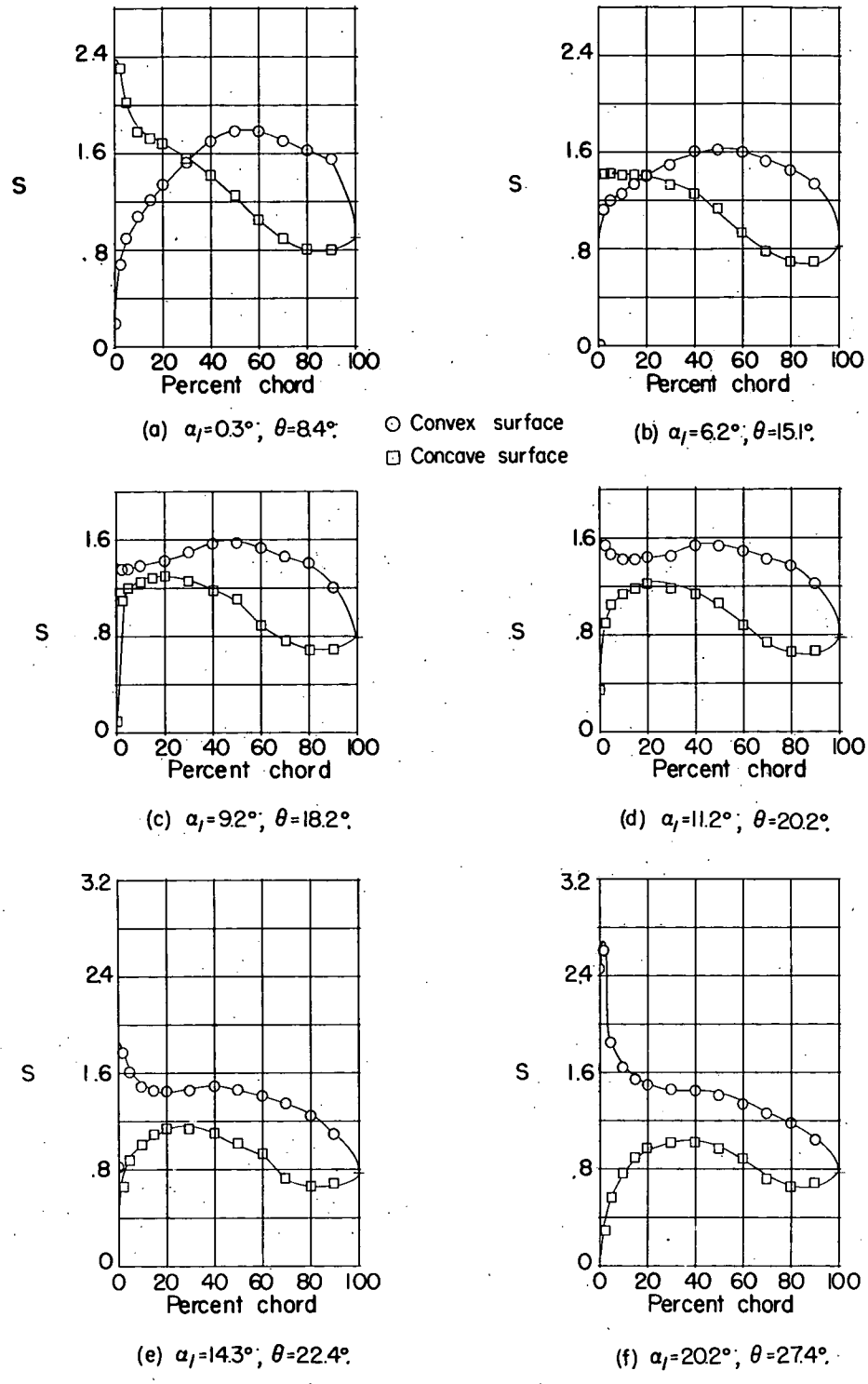

Figure 12.- Blade-surface pressure distributions and blade-section characteristics for the cascade combination $\beta_1 = 30^\circ$ and $\sigma = 1.5$ and NACA 65-$(8A_2I_{8b})$10 blade section.

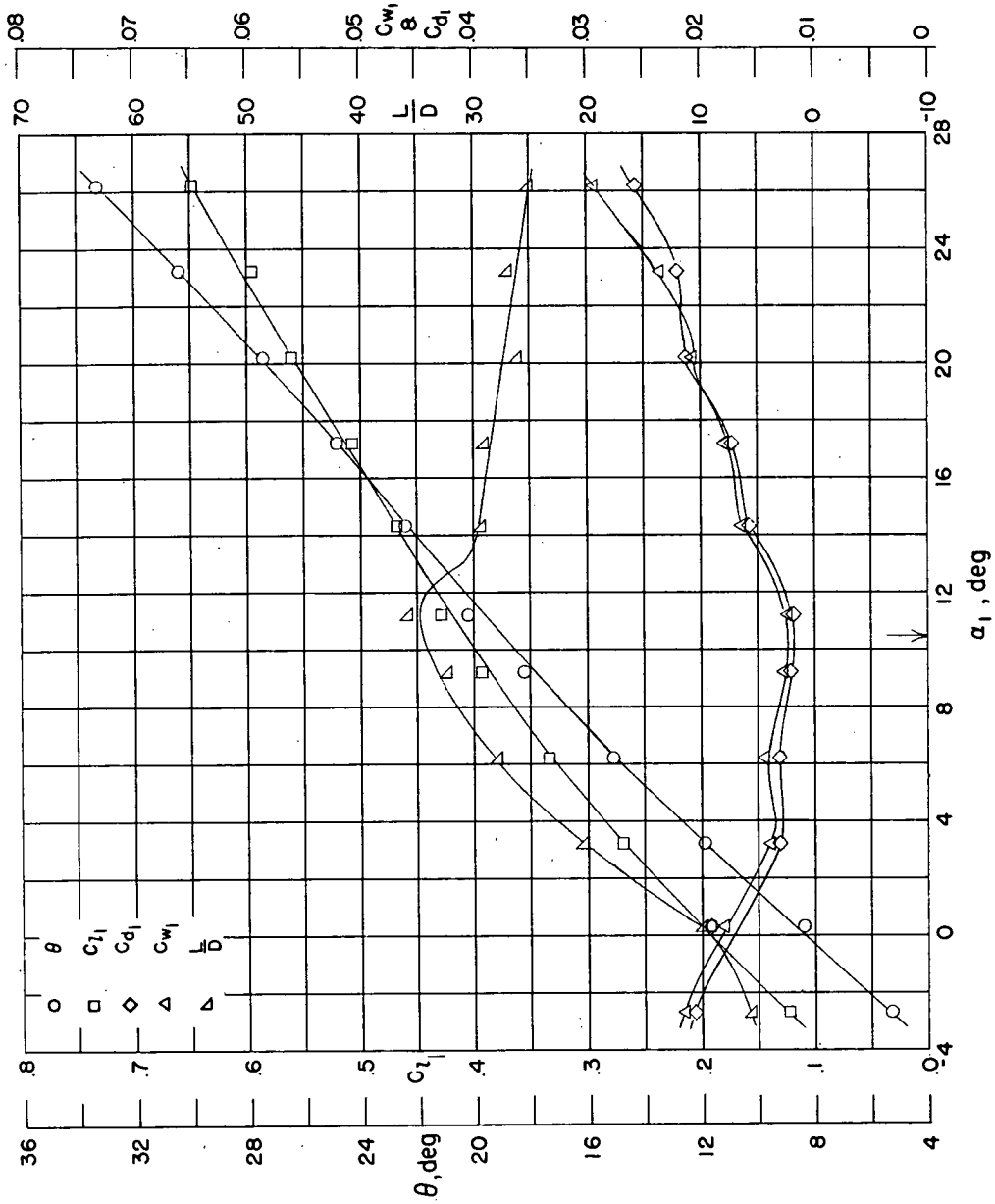

(g) Section characteristics. Arrow shows design angle of attack.

Figure 12.- Concluded.

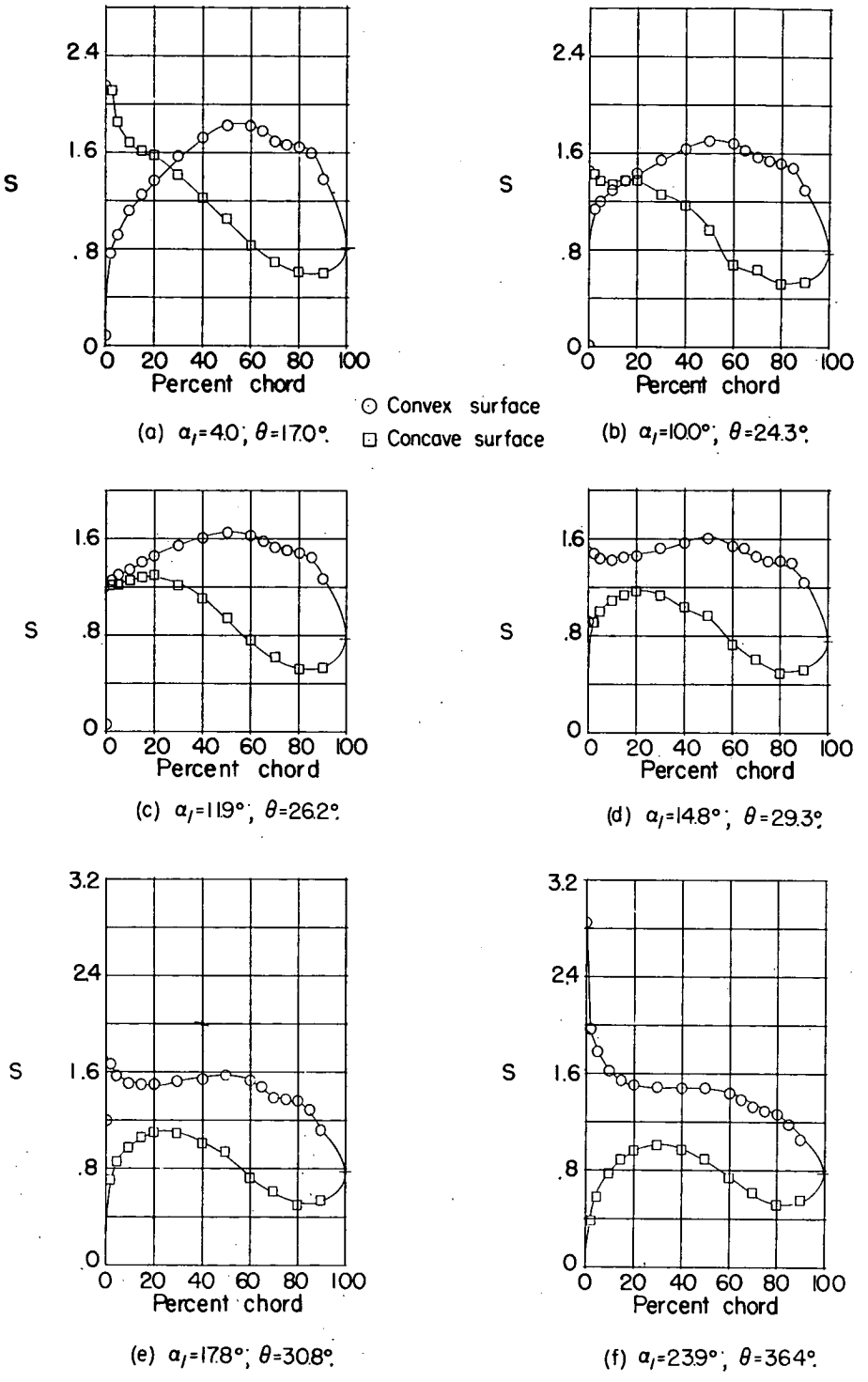

Figure 13.- Blade-surface pressure distributions and blade-section characteristics for the cascade combination $\beta_1 = 30^\circ$ and $\sigma = 1.5$ and NACA 65-$\left(12A_2I_{8b}\right)$10 blade section.

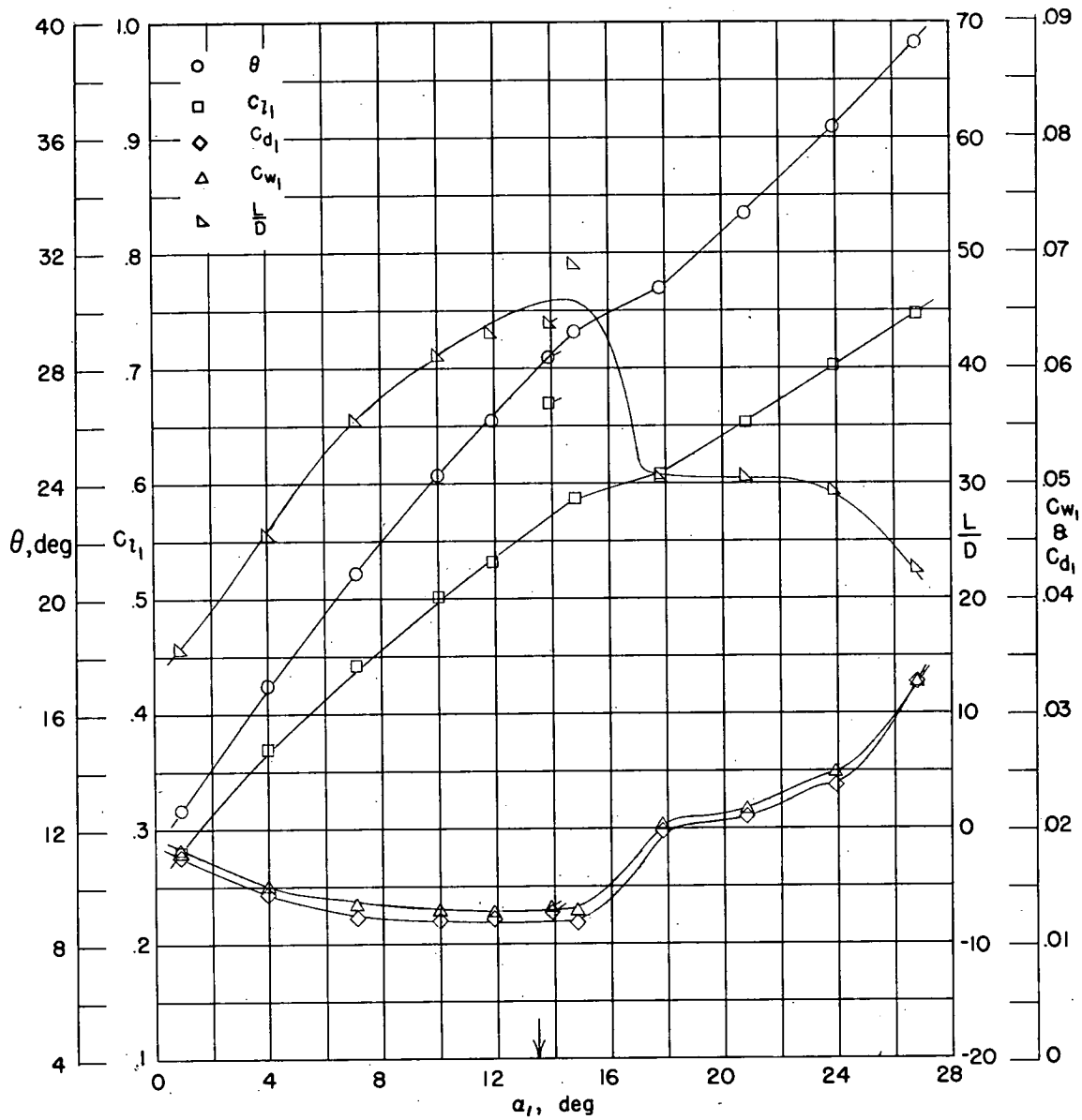

(g) Section characteristics. Arrow shows design angle of attack; flagged symbol indicates roughness.

Figure 13.- Concluded.

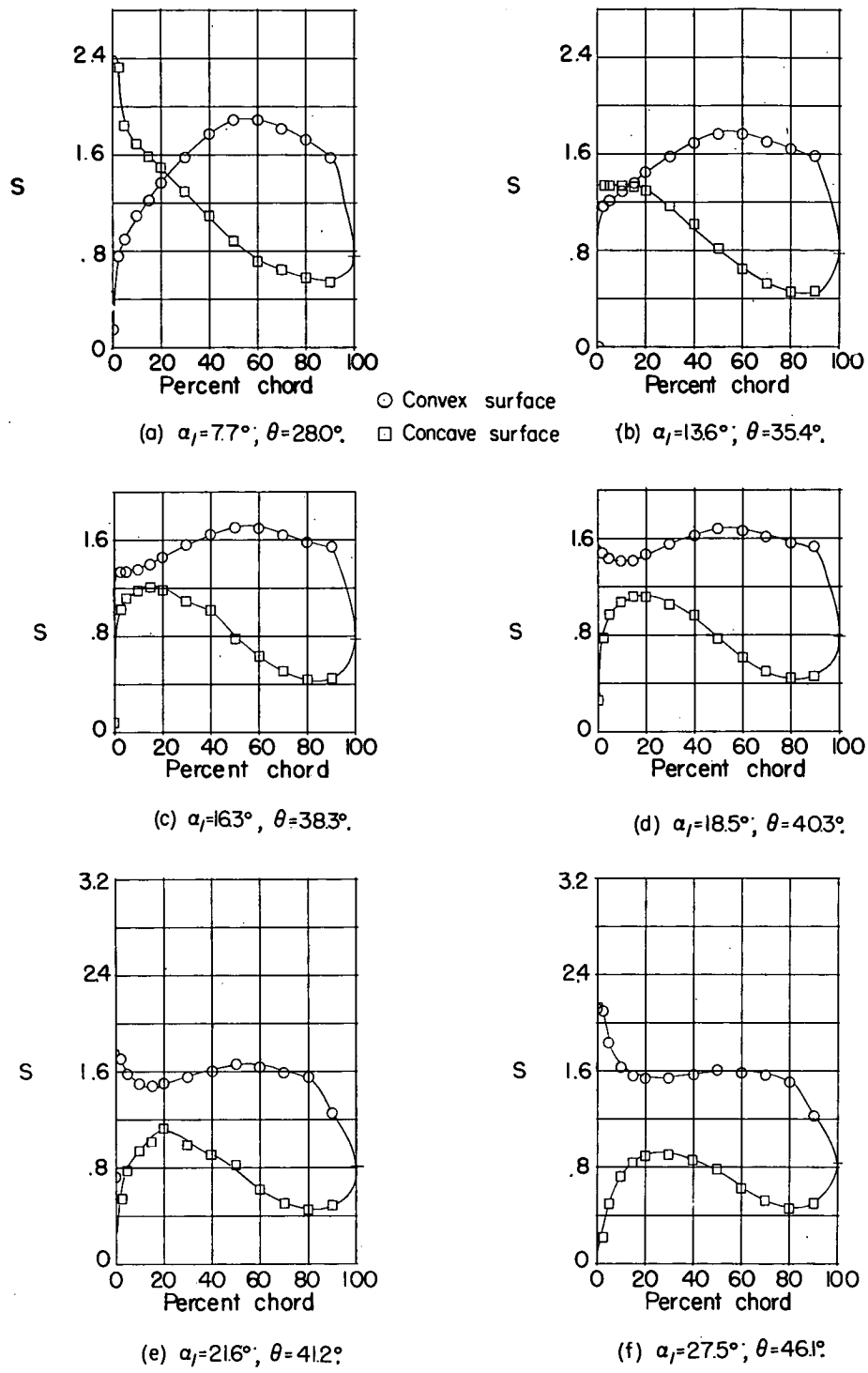

Figure 14.- Blade-surface pressure distributions and blade-section characteristics for the cascade combination $\beta_1 = 30^\circ$ and $\sigma = 1.5$ and NACA 65-$(18A_2I_{8b})$10 blade section.

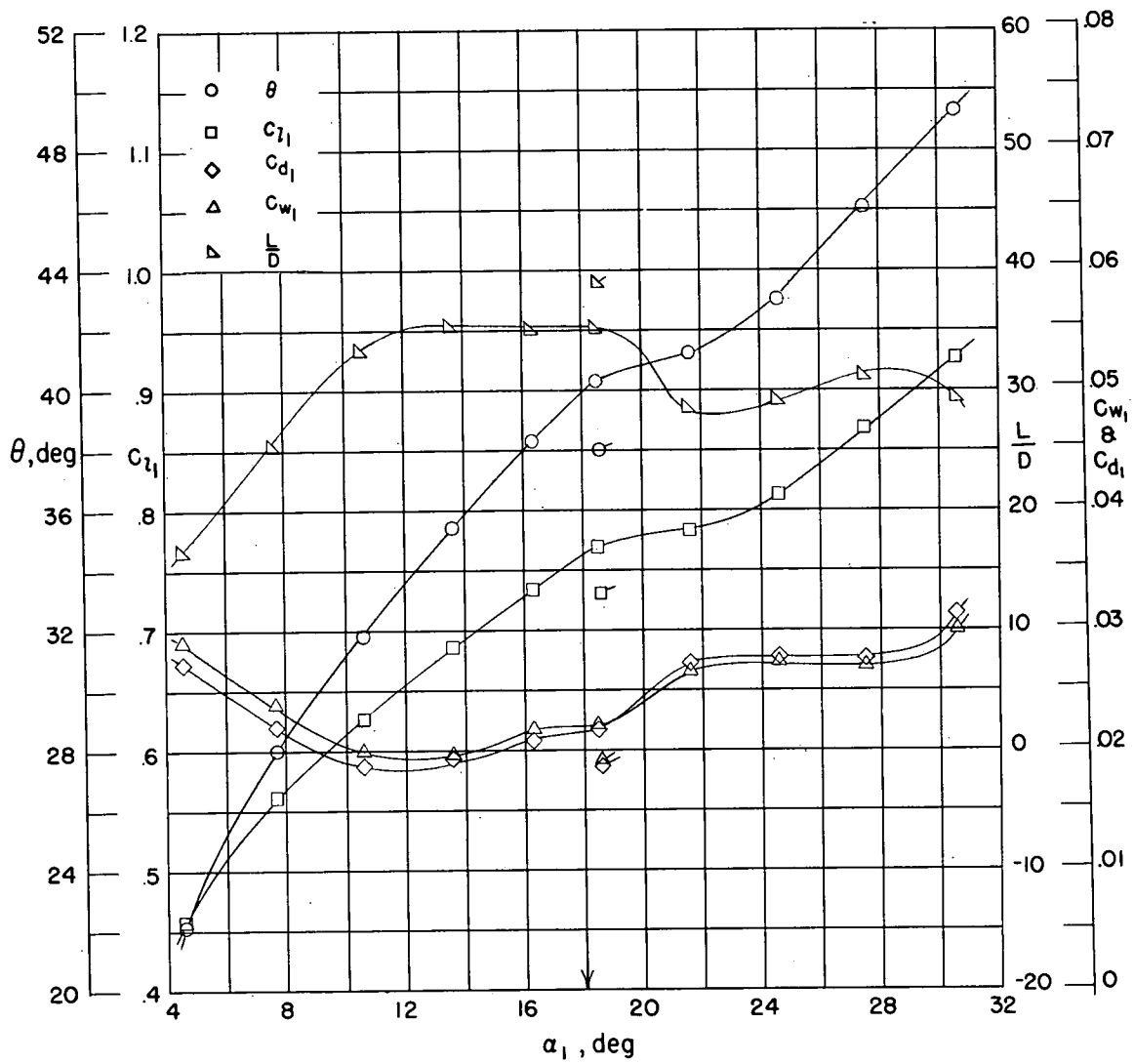

(g) Section characteristics. Arrow shows design angle of attack; flagged symbol indicates roughness.

Figure 14.- Concluded.

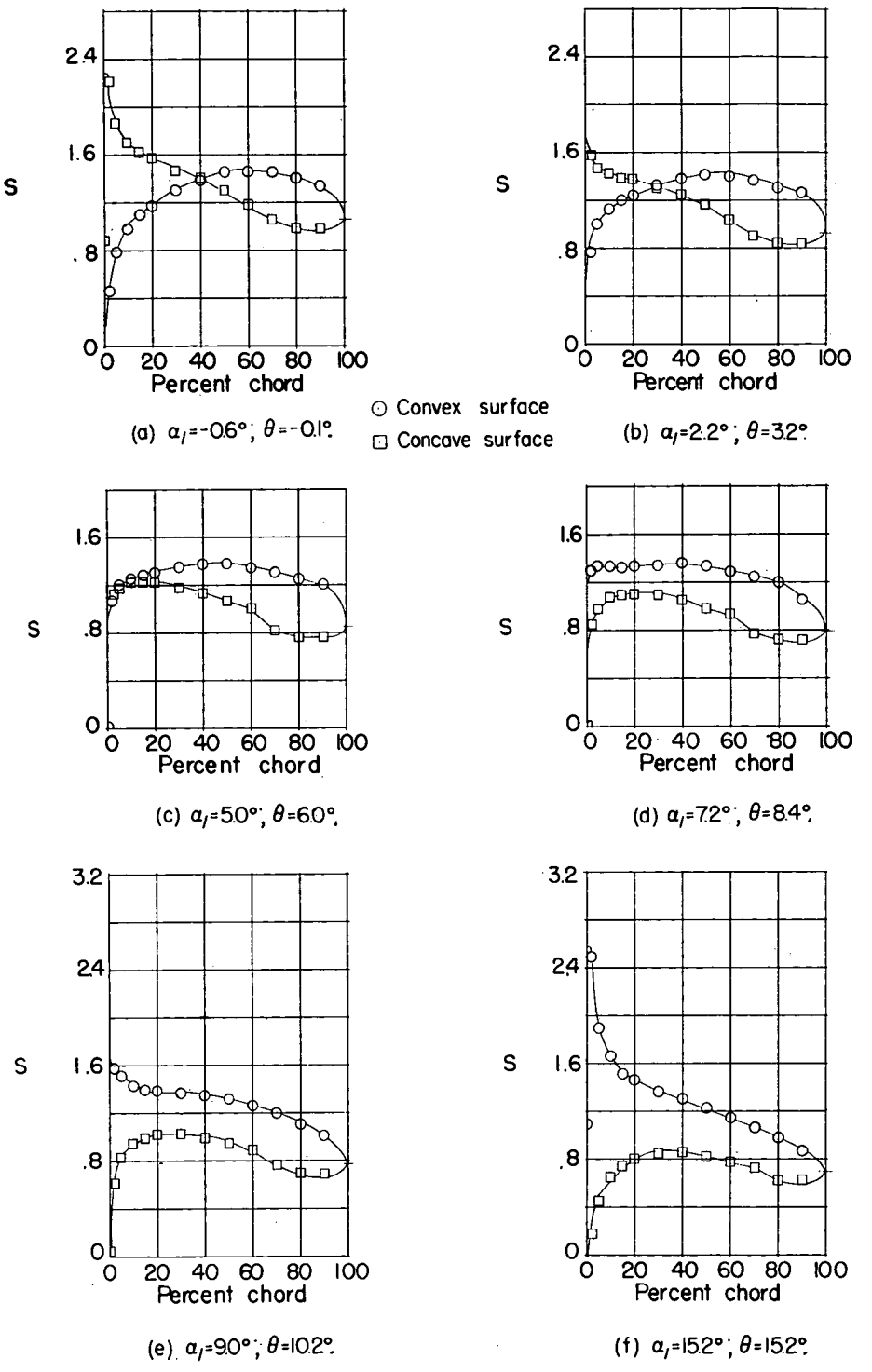

Figure 15.- Blade-surface pressure distributions and blade-section characteristics for the cascade combination $\beta_1 = 45^\circ$ and $\sigma = 1.0$ and NACA 65-$(4A_2I_{8b})$10 blade section.

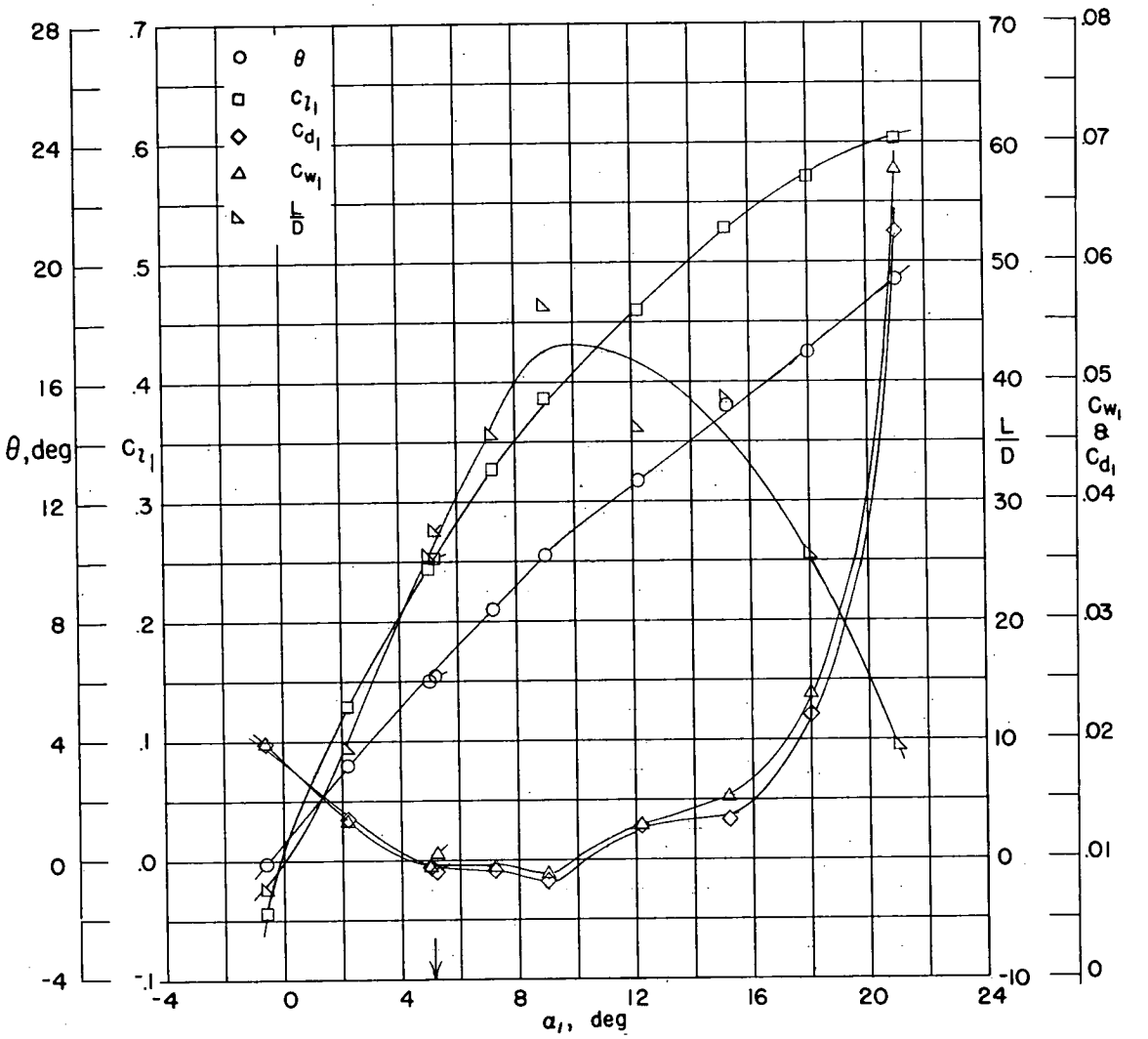

(g) Section characteristics. Arrow shows design angle of attack; flagged symbol indicates roughness.

Figure 15.- Concluded.

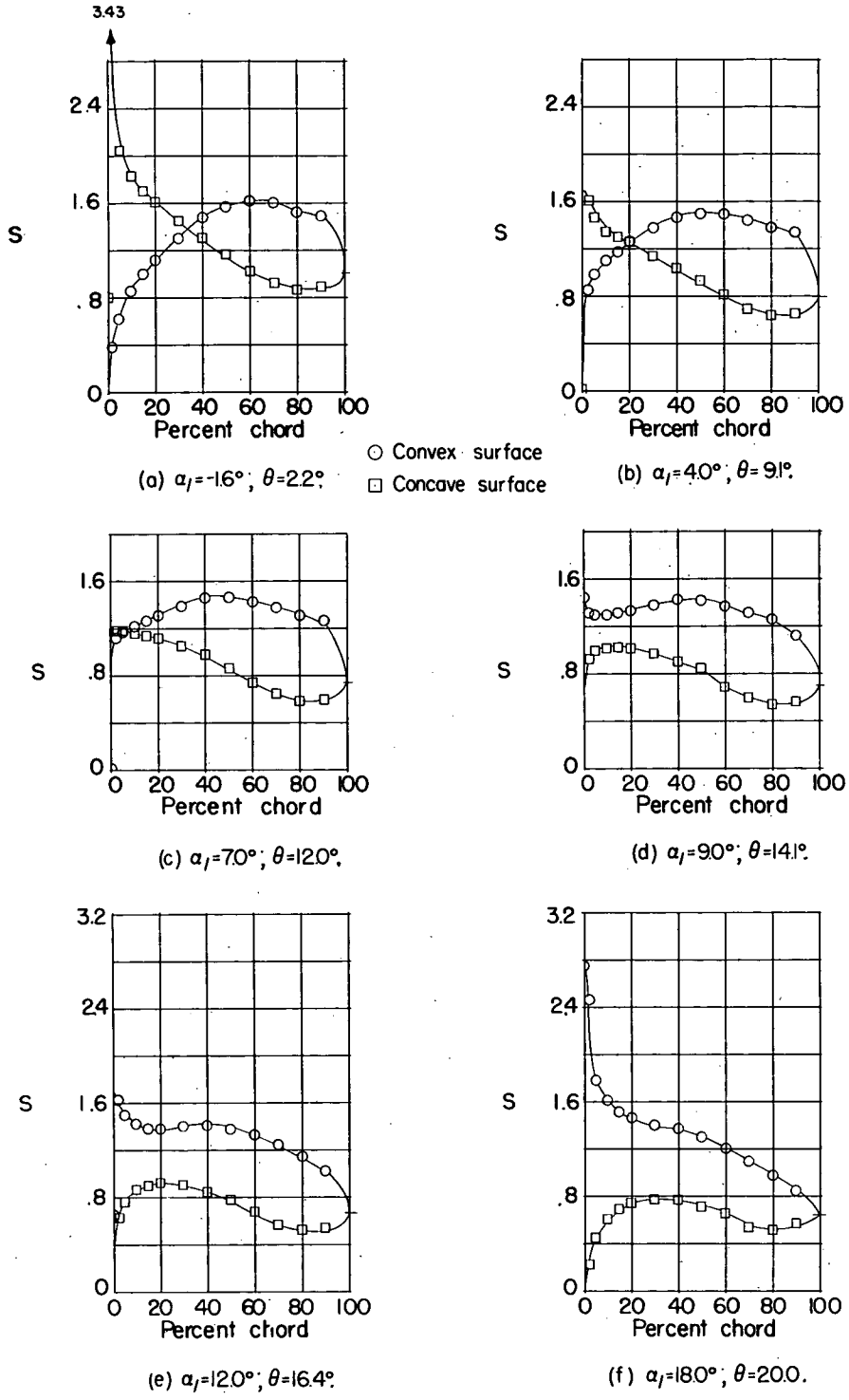

Figure 16.- Blade-surface pressure distributions and blade-section characteristics for the cascade combination $\beta_1 = 45^\circ$ and $\sigma = 1.0$ and NACA 65-$(8A_2I_{8b})$10 blade section.

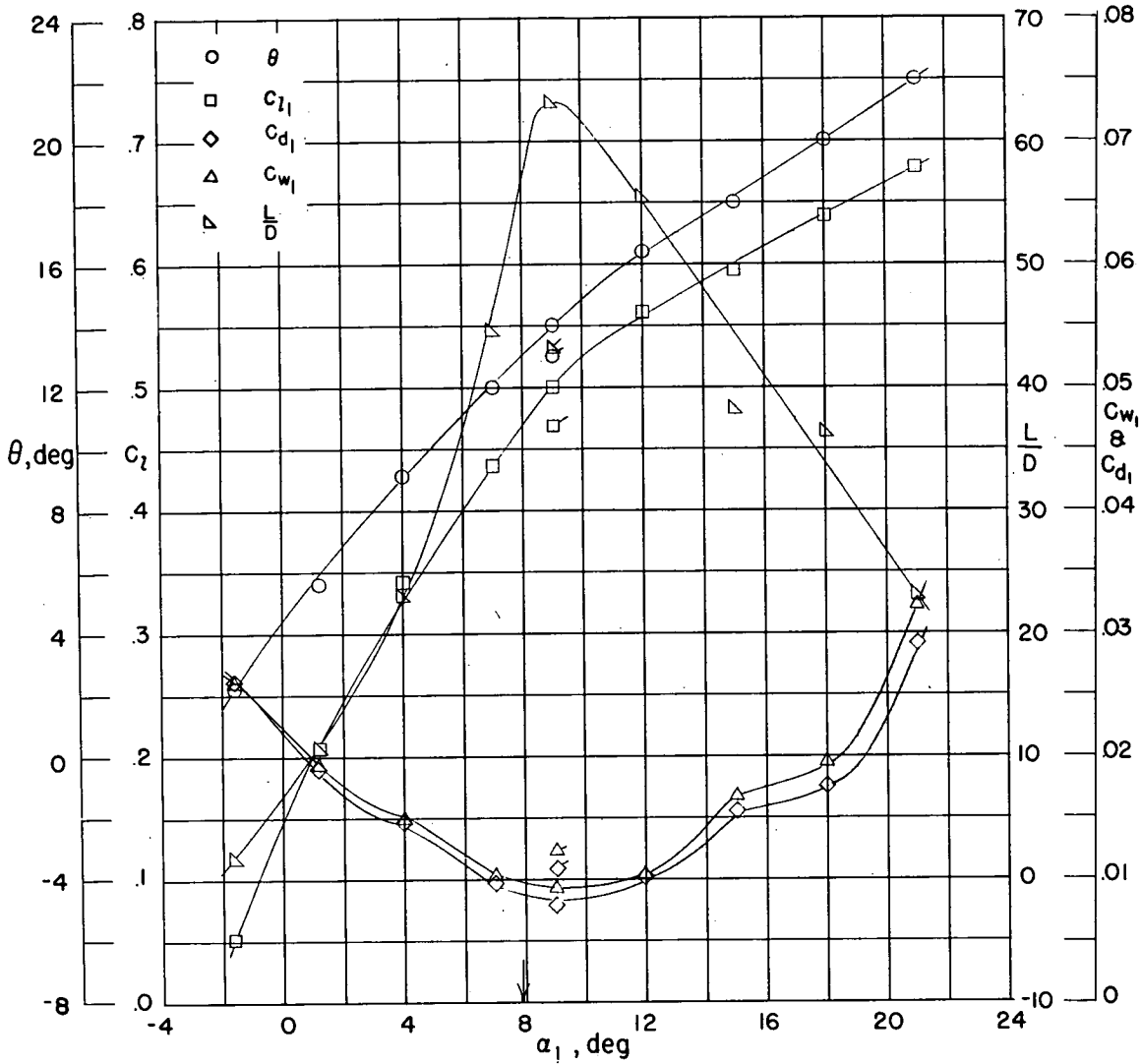

(g) Section characteristics. Arrow shows design angle of attack; flagged symbol indicates roughness.

Figure 16.- Concluded.

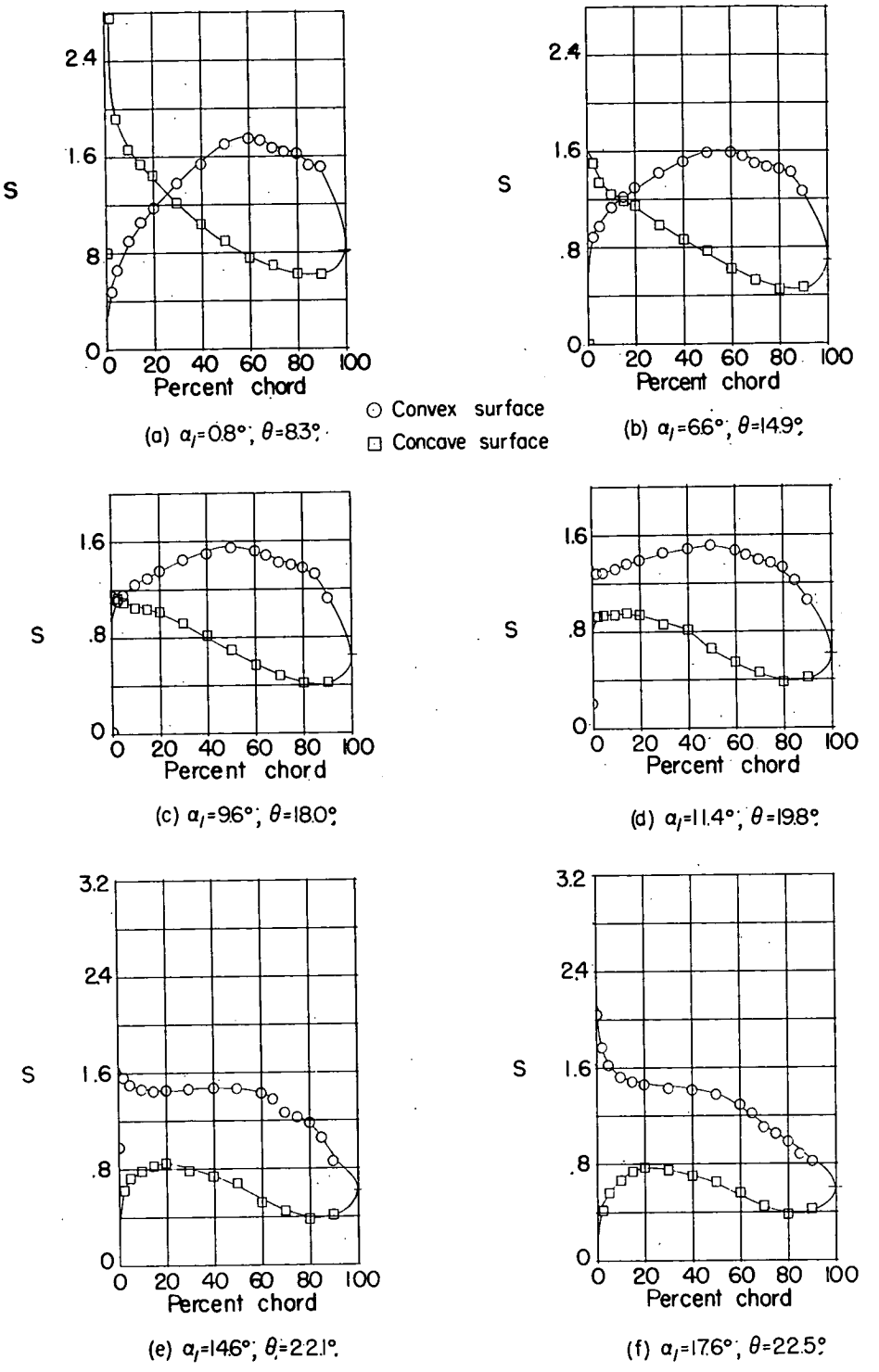

Figure 17.- Blade-surface pressure distributions and blade-section characteristics for the cascade combination $\beta_1 = 45°$ and $\sigma = 1.0$ and NACA 65-$(12A_2I_{8b})$10 blade section.

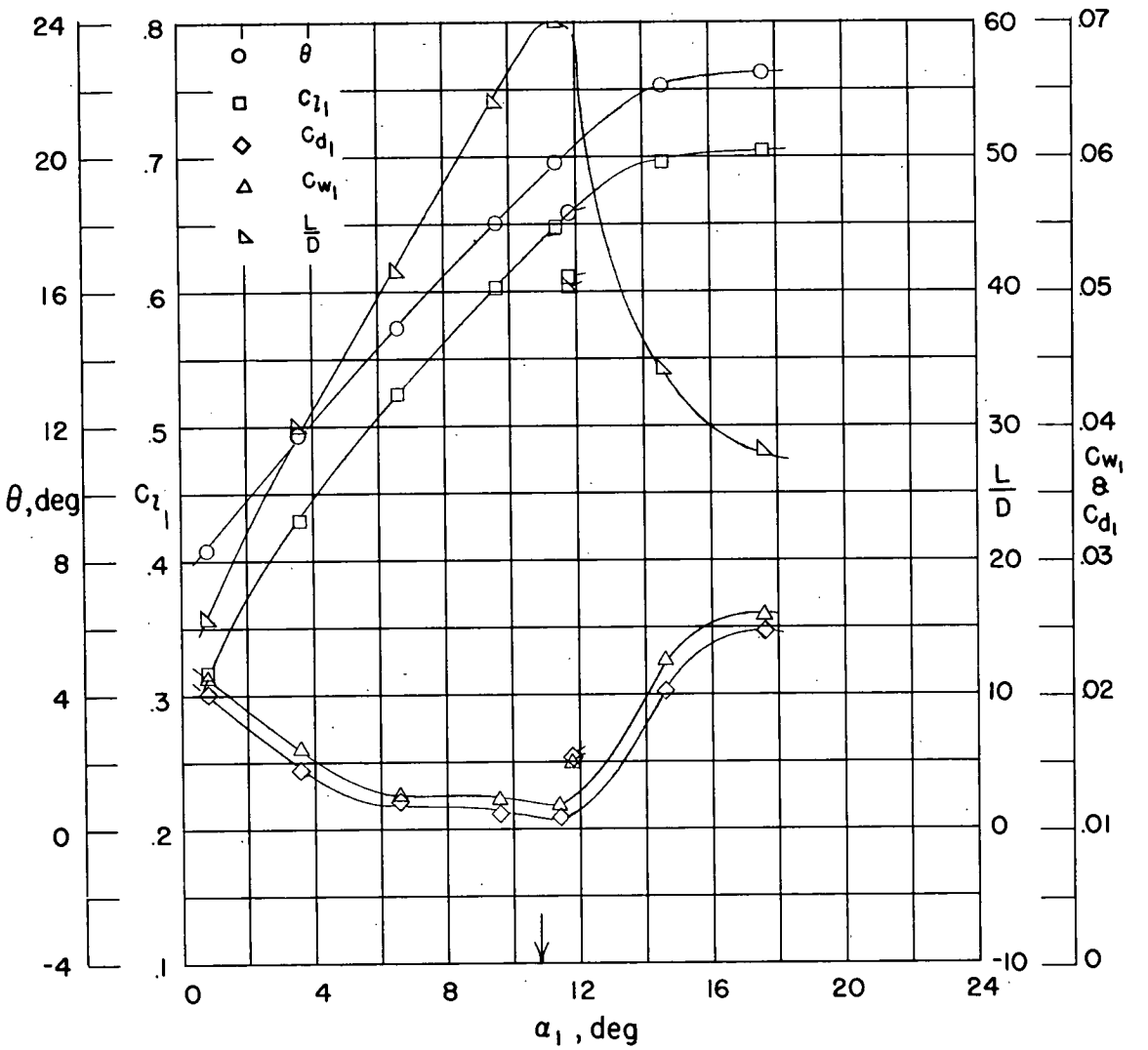

(g) Section characteristics. Arrow shows design angle of attack; flagged symbol indicates roughness.

Figure 17.- Concluded.

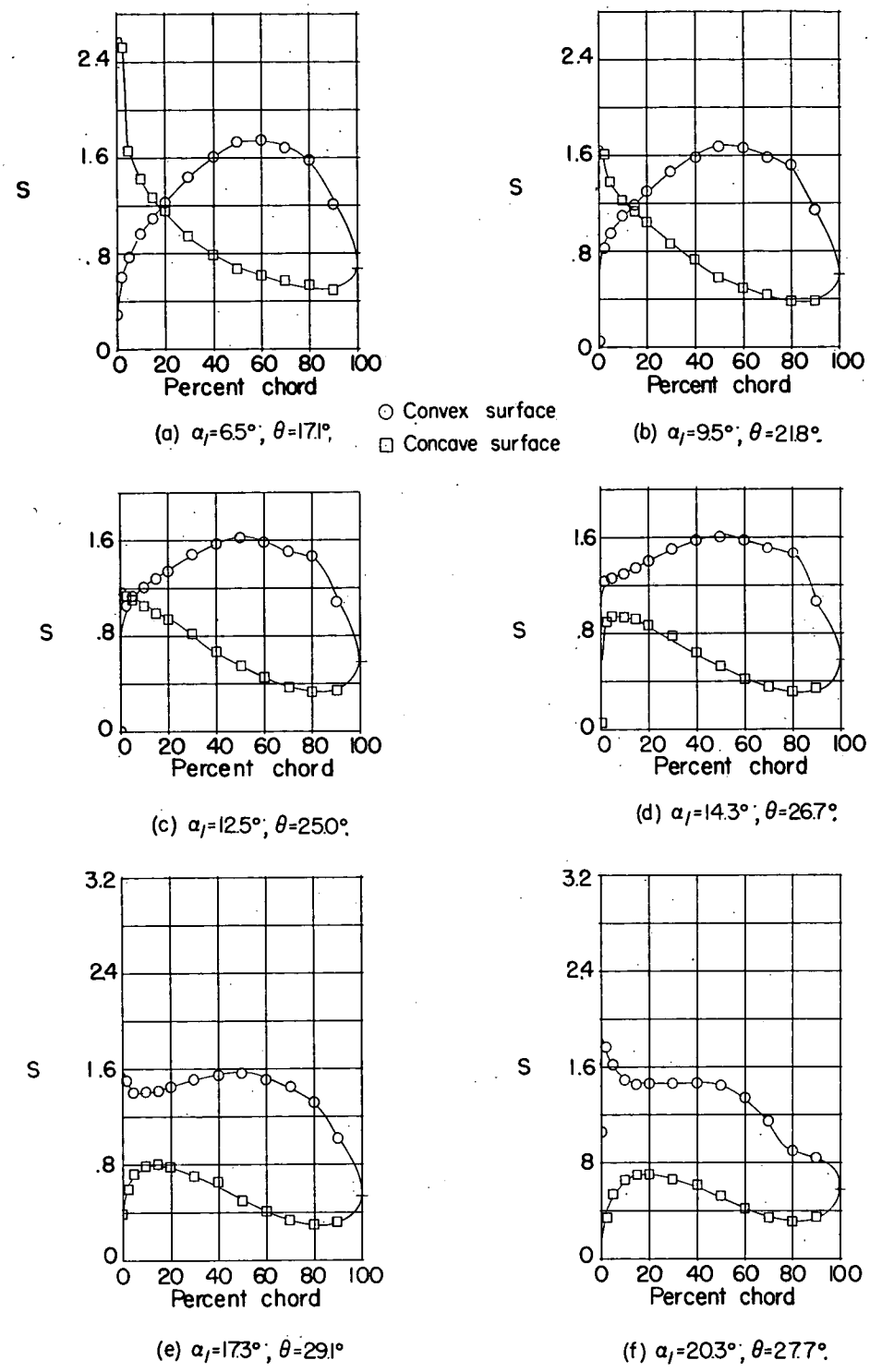

Figure 18.- Blade-surface pressure distributions and blade-section characteristics for the cascade combination $\beta_1 = 45^\circ$ and $\sigma = 1.0$ and NACA 65-$(18A_2I_{8b})$10 blade section.

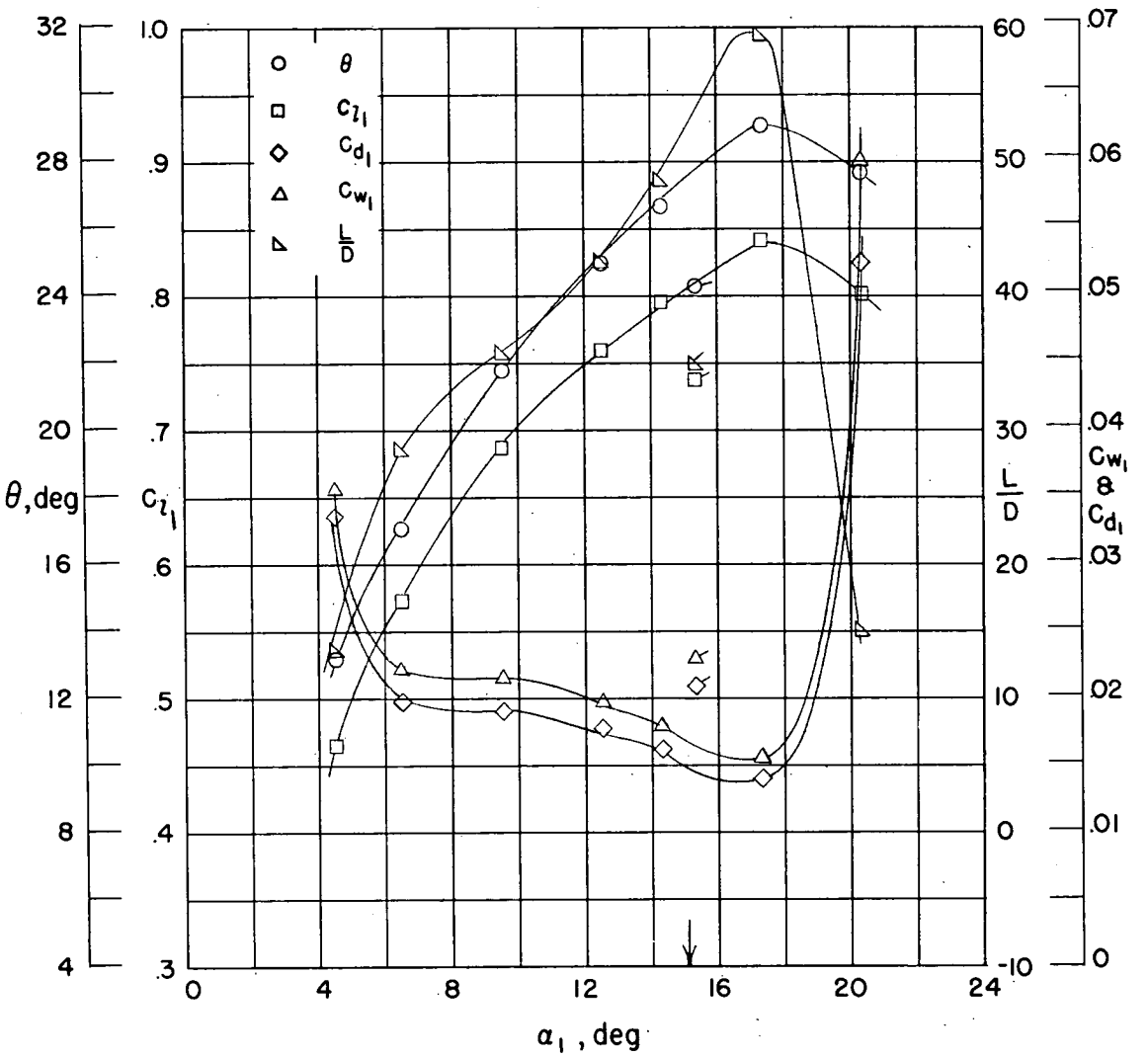

(g) Section characteristics. Arrow shows design angle of attack; flagged symbol indicates roughness.

Figure 18.- Concluded.

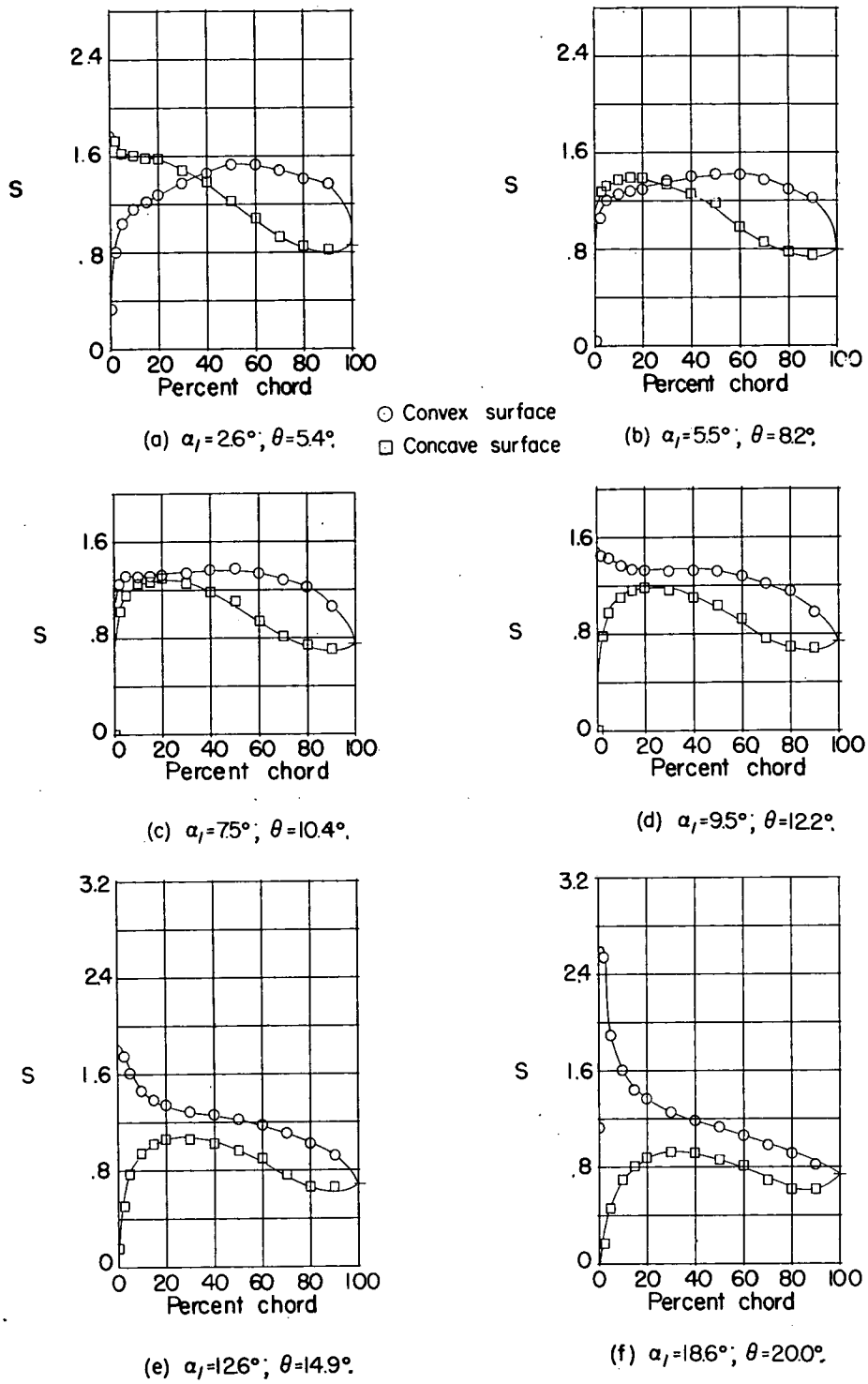

Figure 19.- Blade-surface pressure distributions and blade-section characteristics for the cascade combination $\beta_1 = 45^\circ$ and $\sigma = 1.5$ and NACA 65-$(4A_2I_{8b})$10 blade section.

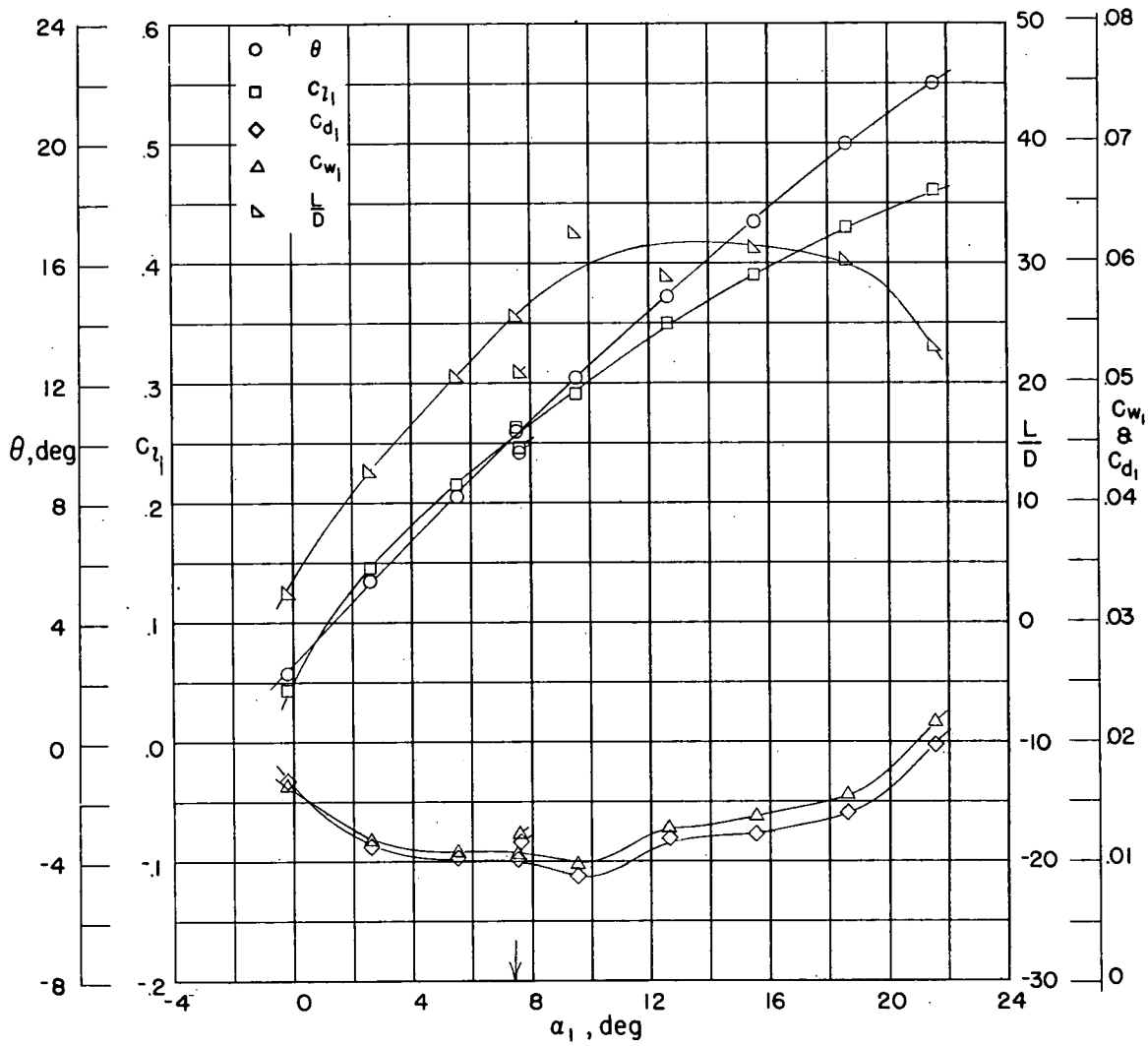

(g) Section characteristics. Arrow shows design angle of attack; flagged symbol indicates roughness.

Figure 19.- Concluded.

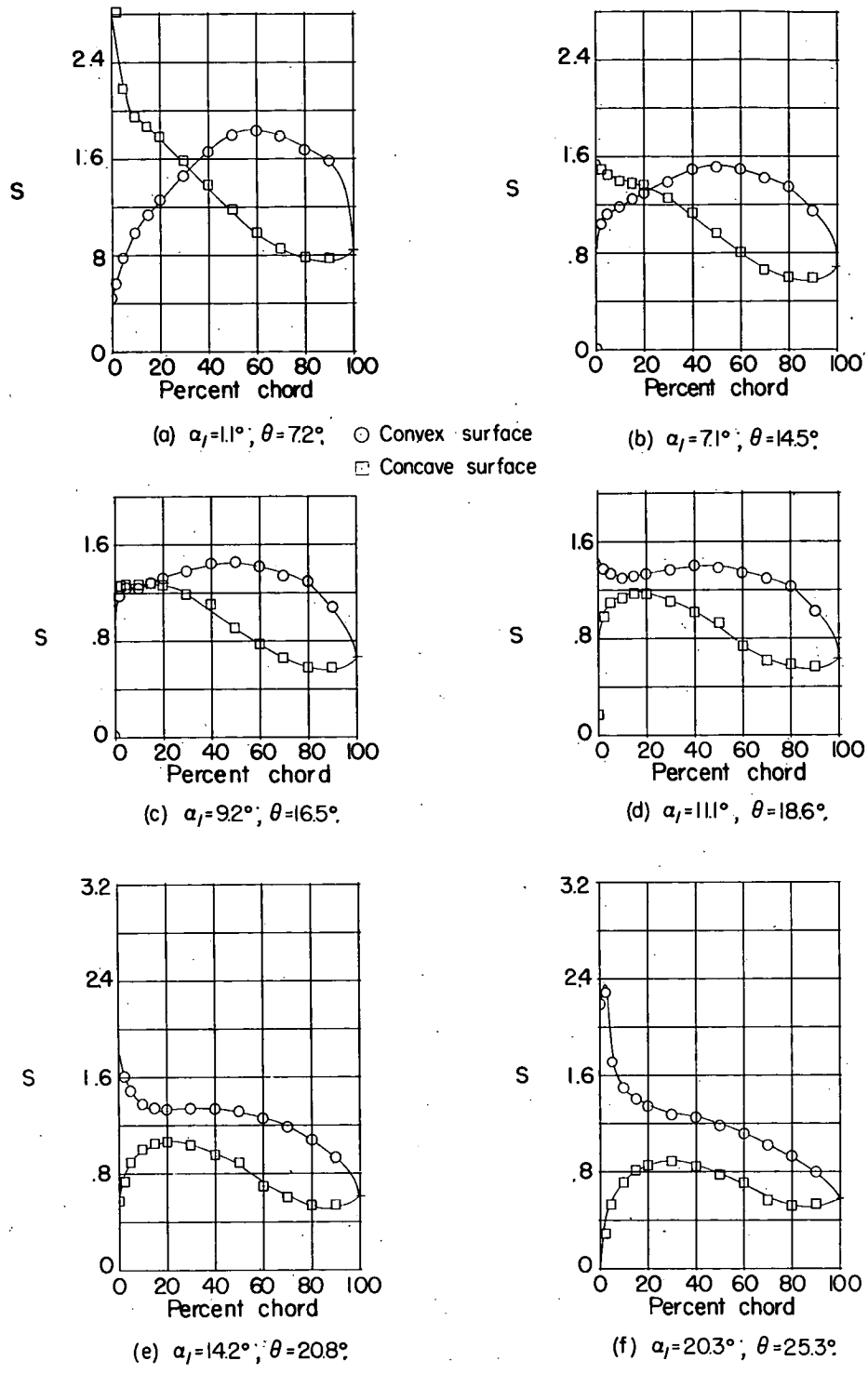

Figure 20. Blade-surface pressure distributions and blade-section characteristics for the cascade combination $\beta_1 = 45^\circ$ and $\sigma = 1.5$ and NACA 65-$(8A_2I_{8b})$10 blade section.

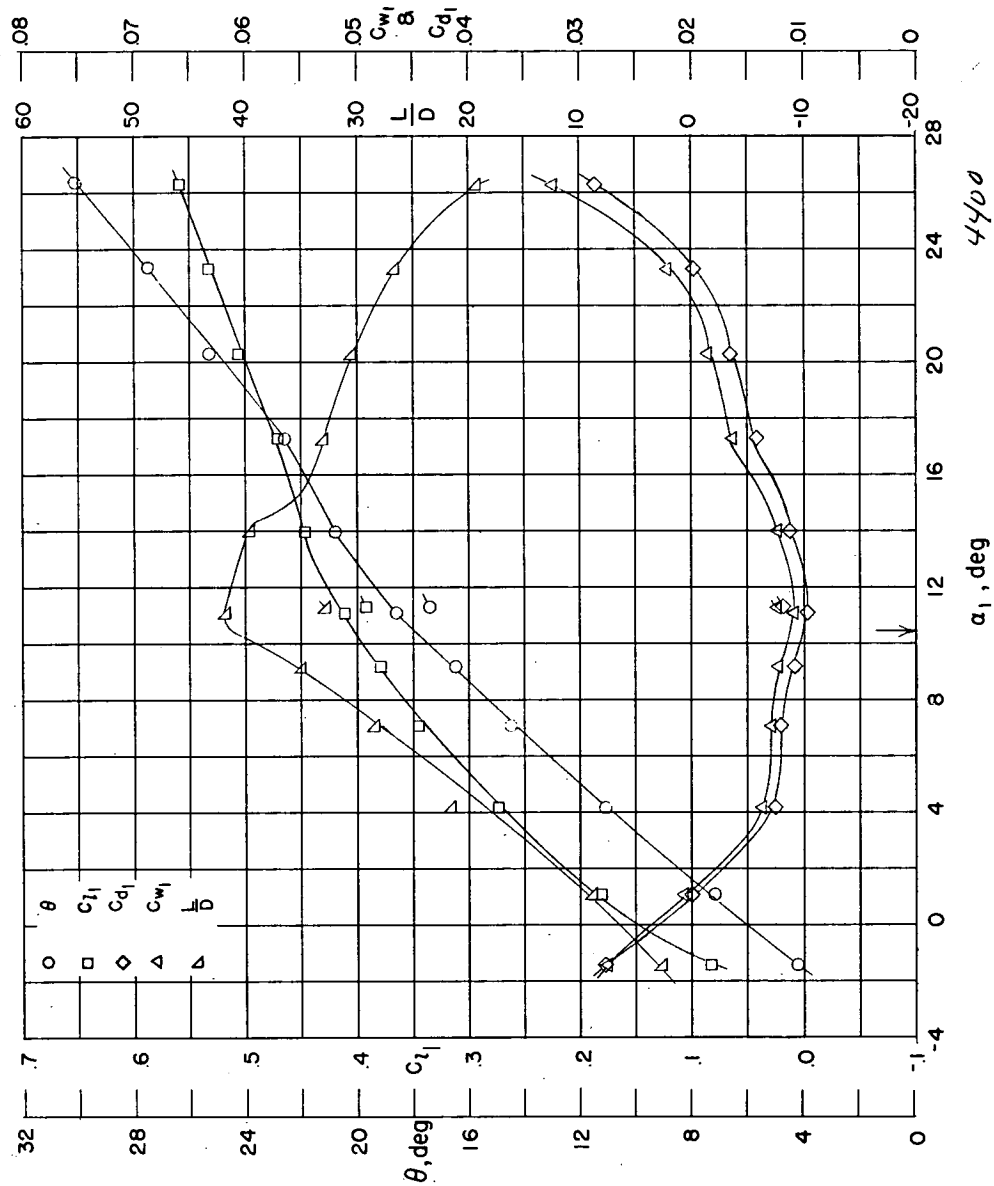

(g) Section characteristics. Arrow shows design angle of attack; flagged symbol indicates roughness.

Figure 20.- Concluded.

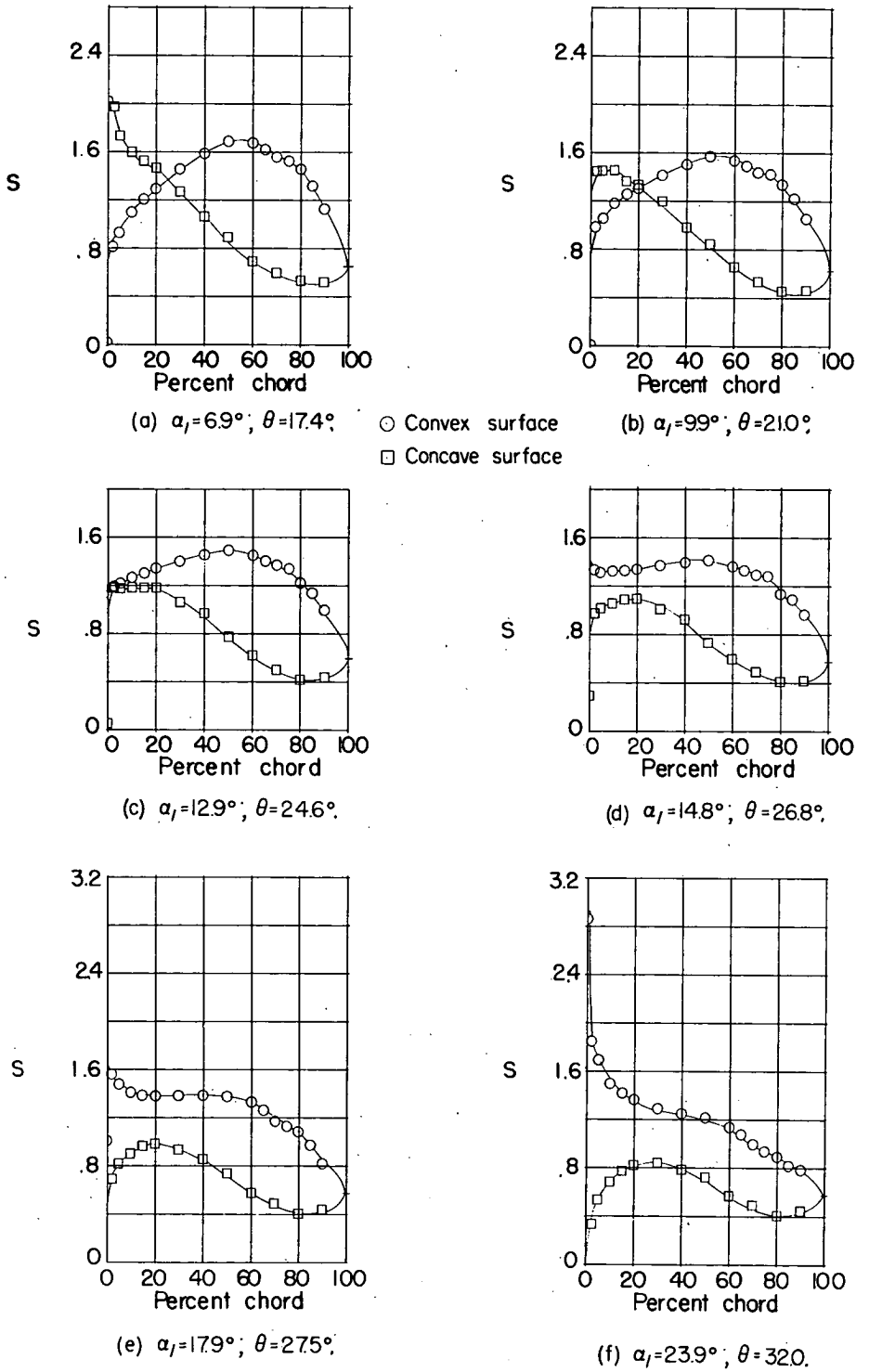

Figure 21.- Blade-surface pressure distributions and blade-section characteristics for the cascade combination $\beta_1 = 45^\circ$ and $\sigma = 1.5$ and NACA 65-$(12A_2I_{8b})$10 blade section.

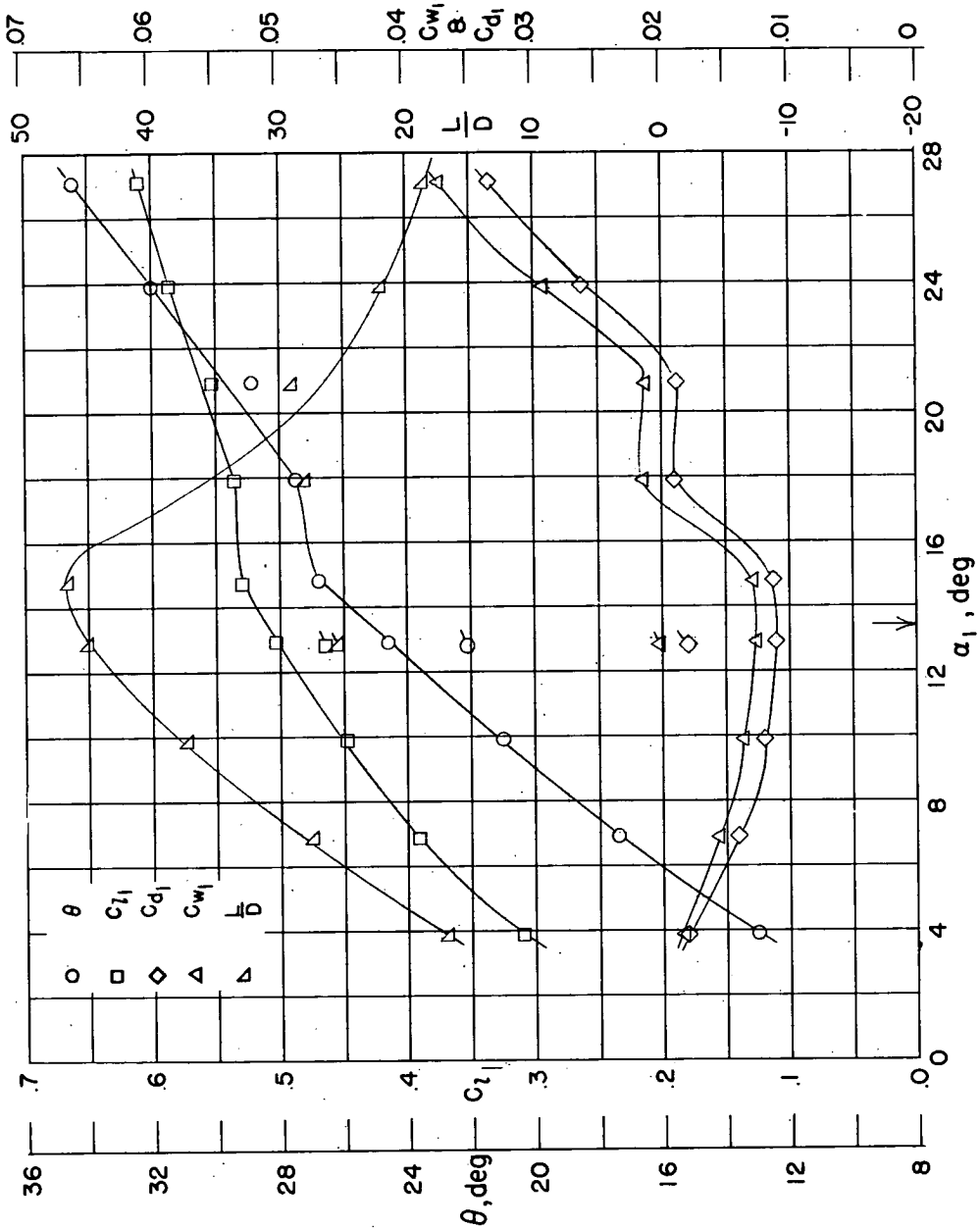

(g) Section characteristics. Arrow shows design angle of attack; flagged symbol indicates roughness.

Figure 21.- Concluded.

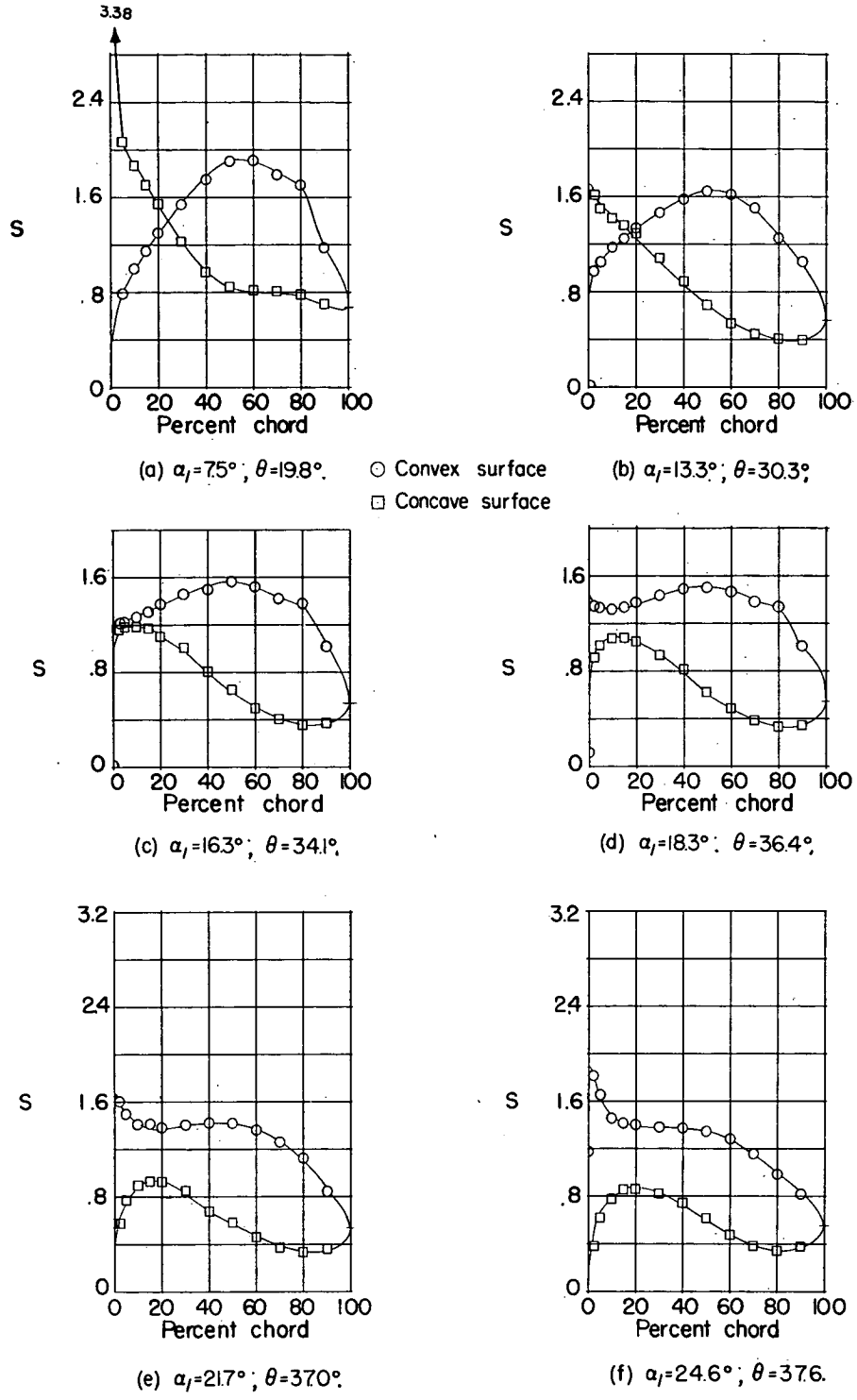

Figure 22.- Blade-surface pressure distributions and blade-section characteristics for the cascade combination $\beta_1 = 45^\circ$ and $\sigma = 1.5$ and NACA 65-$\left(18A_2I8_b\right)$10 blade section.

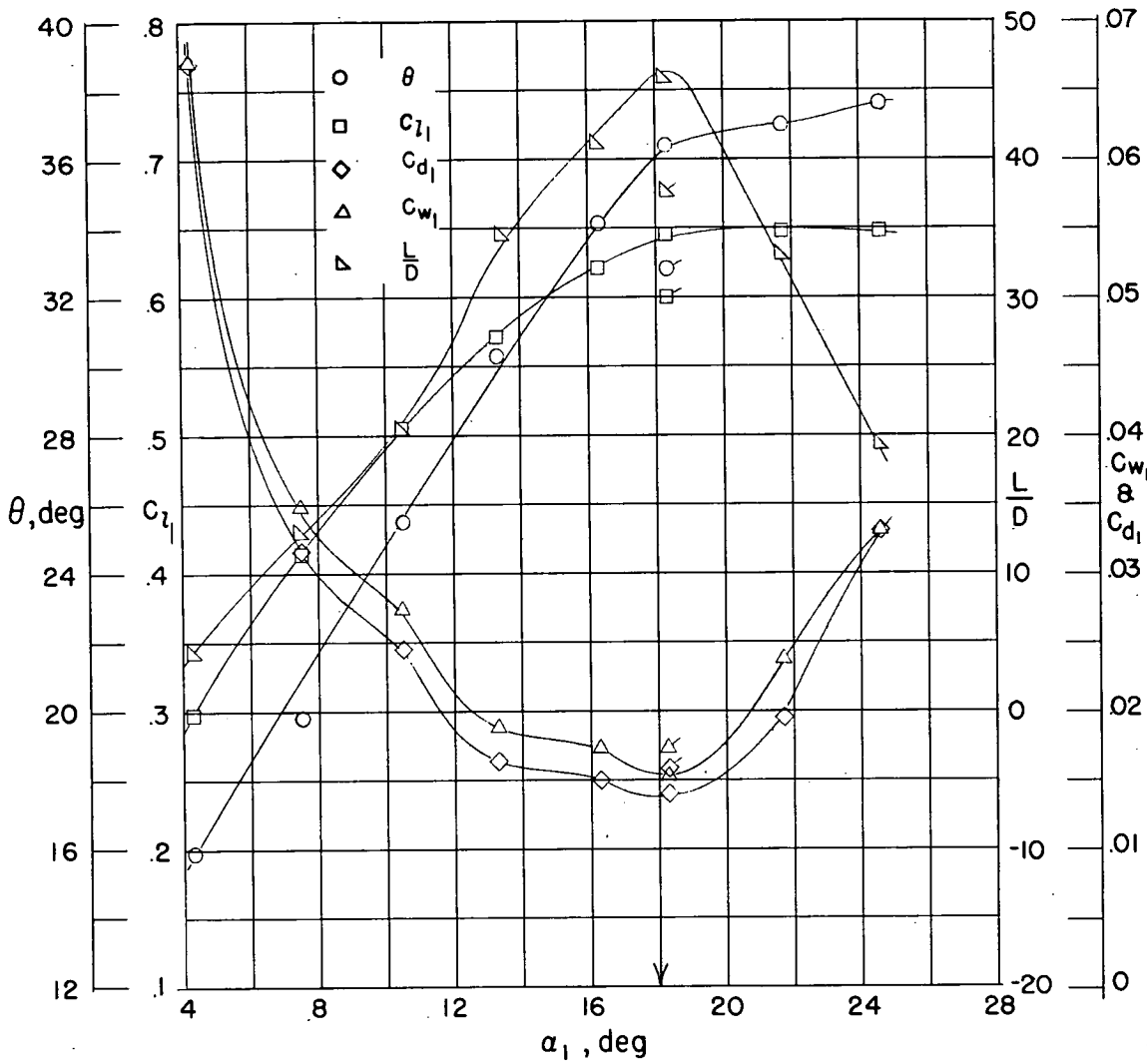

(g) Section characteristics. Arrow shows design angle of attack; flagged symbol indicates roughness.

Figure 22.- Concluded.

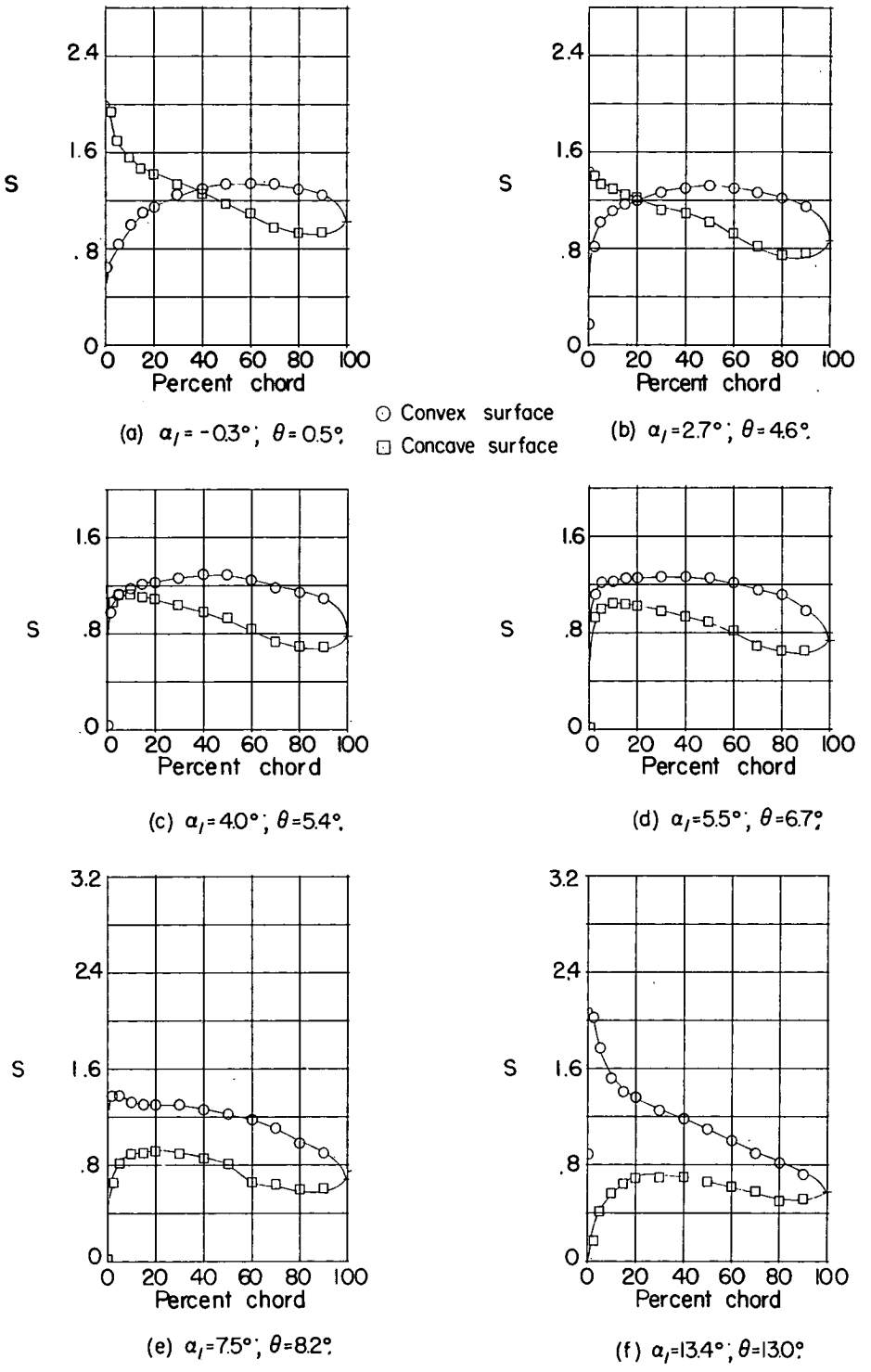

Figure 23.- Blade-surface pressure distributions and blade-section characteristics for the cascade combination $\beta_1 = 60^\circ$ and $\sigma = 1.0$ and NACA 65-$(4A_2I_{8b})$10 blade section.

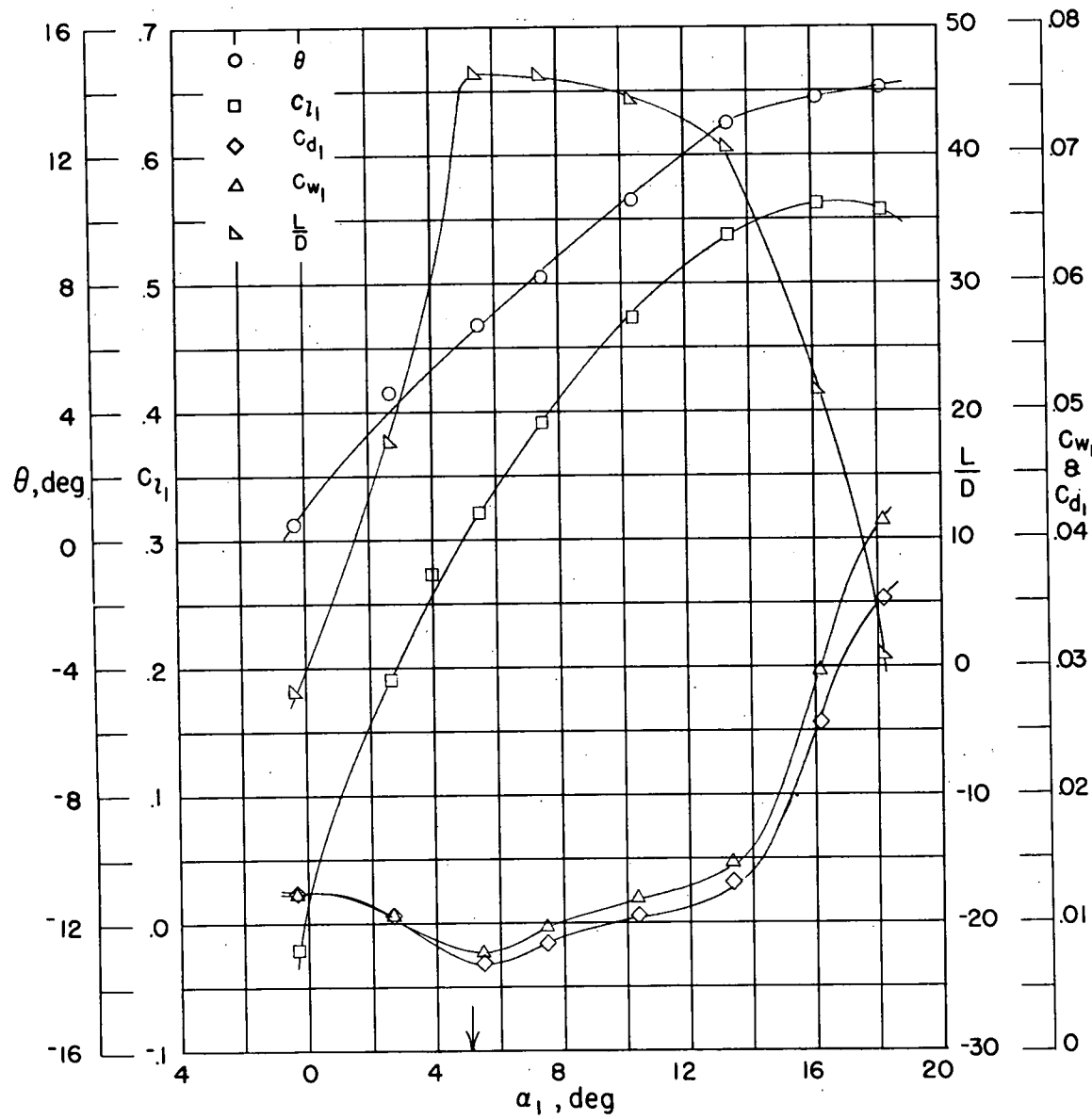

(g) Section characteristics. Arrow shows design angle of attack.

Figure 23.- Concluded.

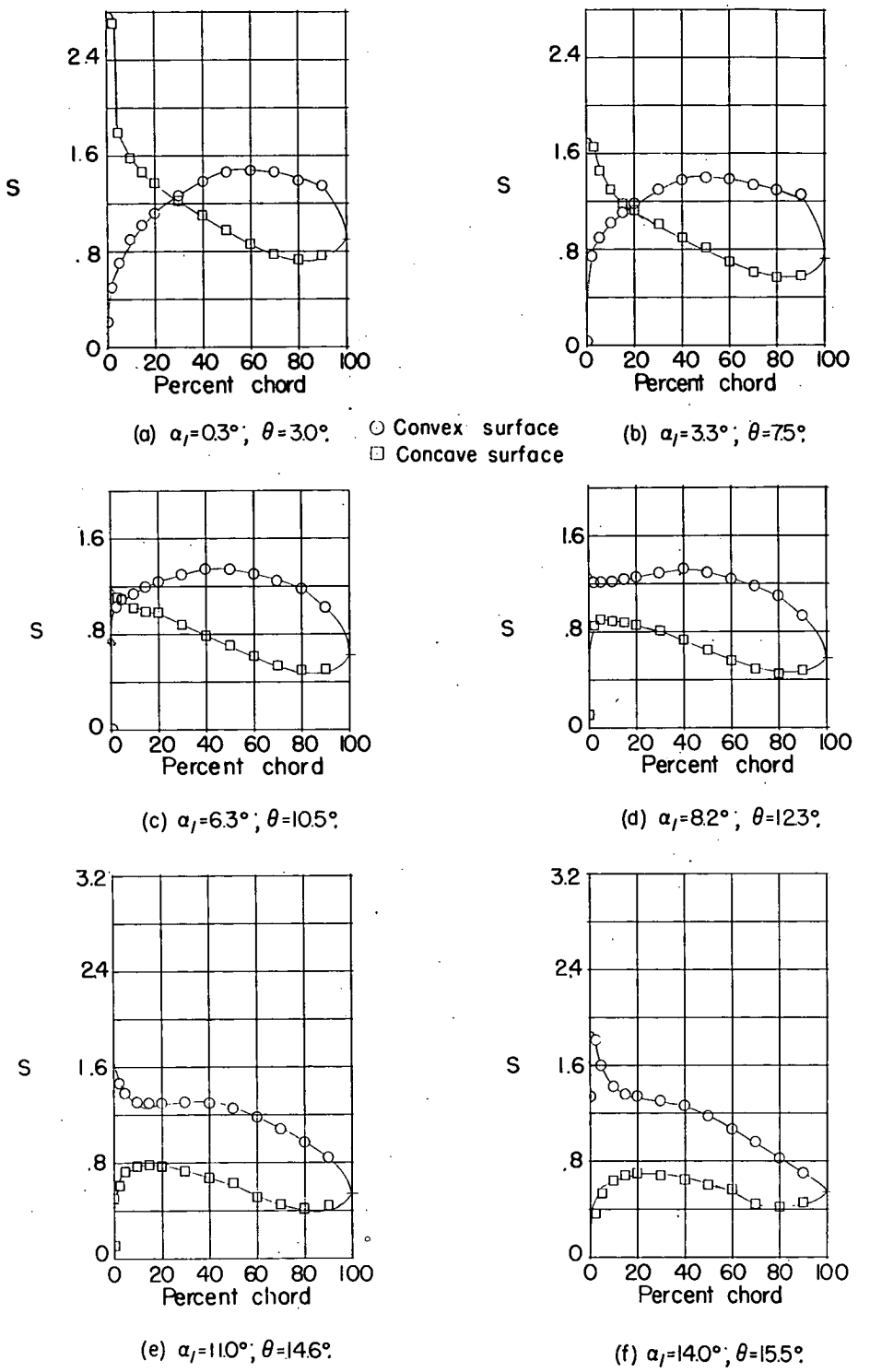

Figure 24.- Blade-surface pressure distributions and blade-section characteristics for the cascade combination $\beta_1 = 60^\circ$ and $\sigma = 1.0$ and NACA 65-$(8A_2I_{8b})$10 blade section.

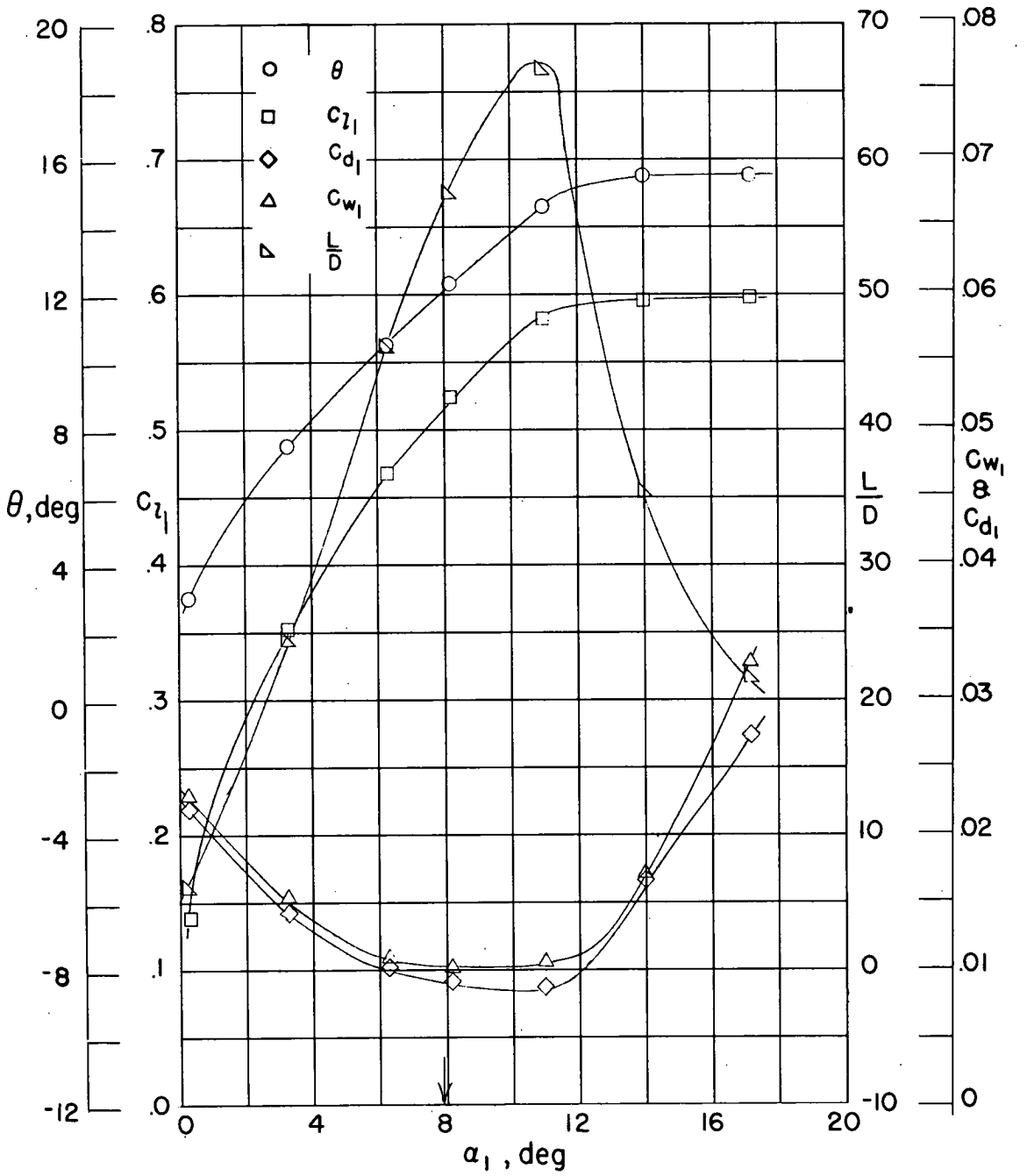

(g) Section characteristics. Arrow shows design angle of attack.

Figure 24.- Concluded.

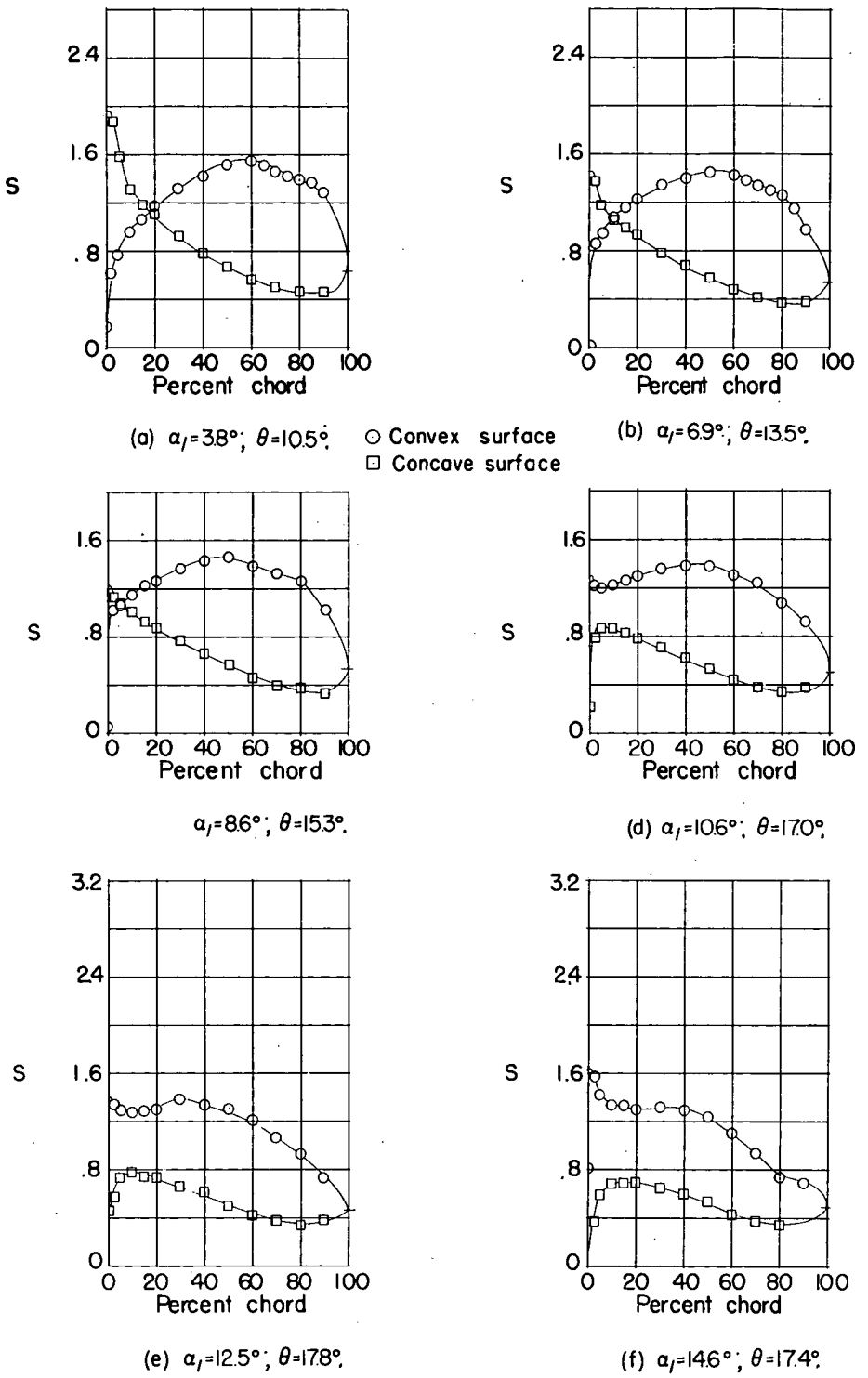

Figure 25.- Blade-surface pressure distributions and blade-section characteristics for the cascade combination $\beta_1 = 60^\circ$ and $\sigma = 1.0$ and NACA 65-$(12A_2I_{8b})$10 blade section.

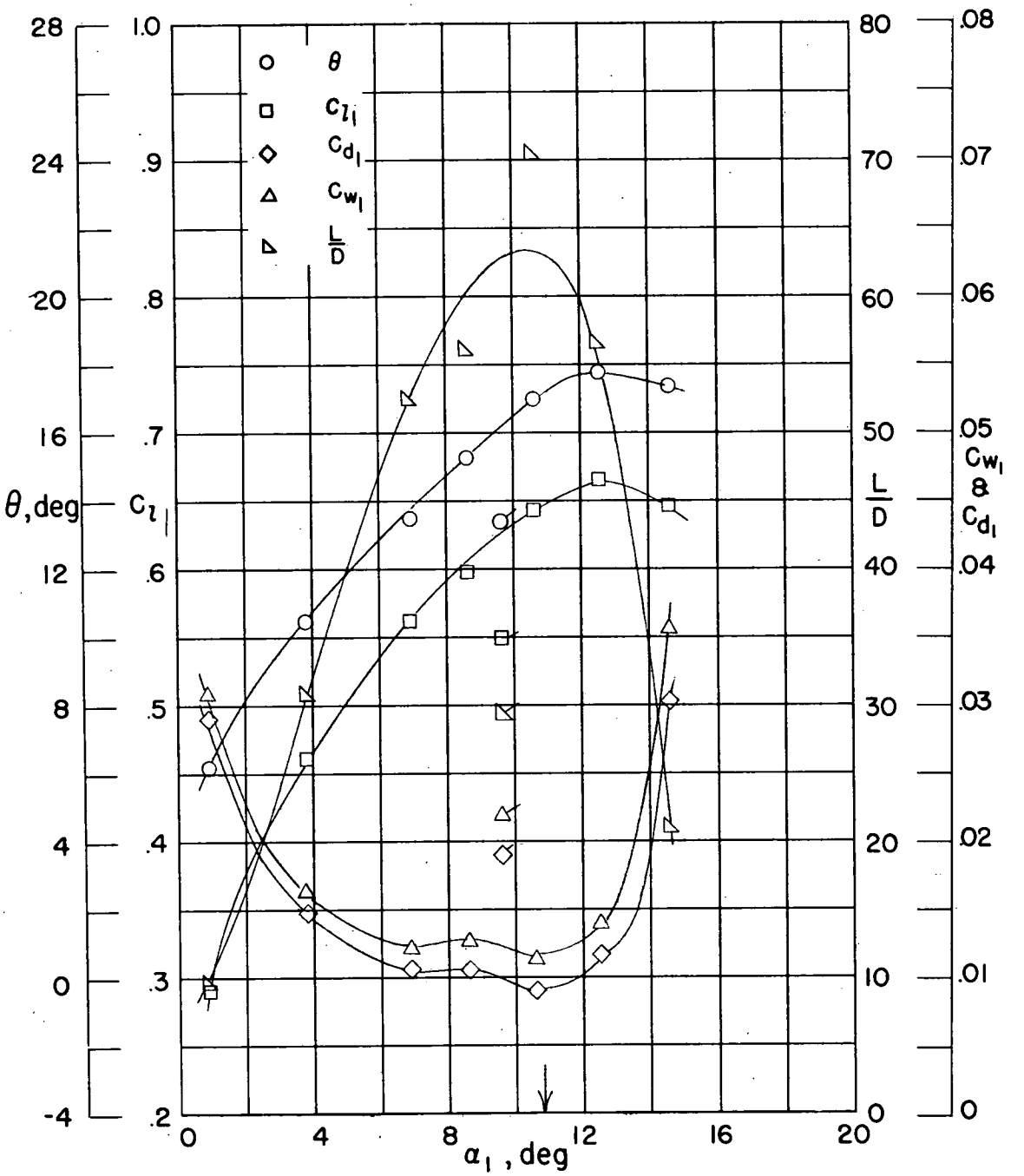

(g) Section characteristics. Arrow shows design angle of attack; flagged symbol indicates roughness.

Figure 25.- Concluded.

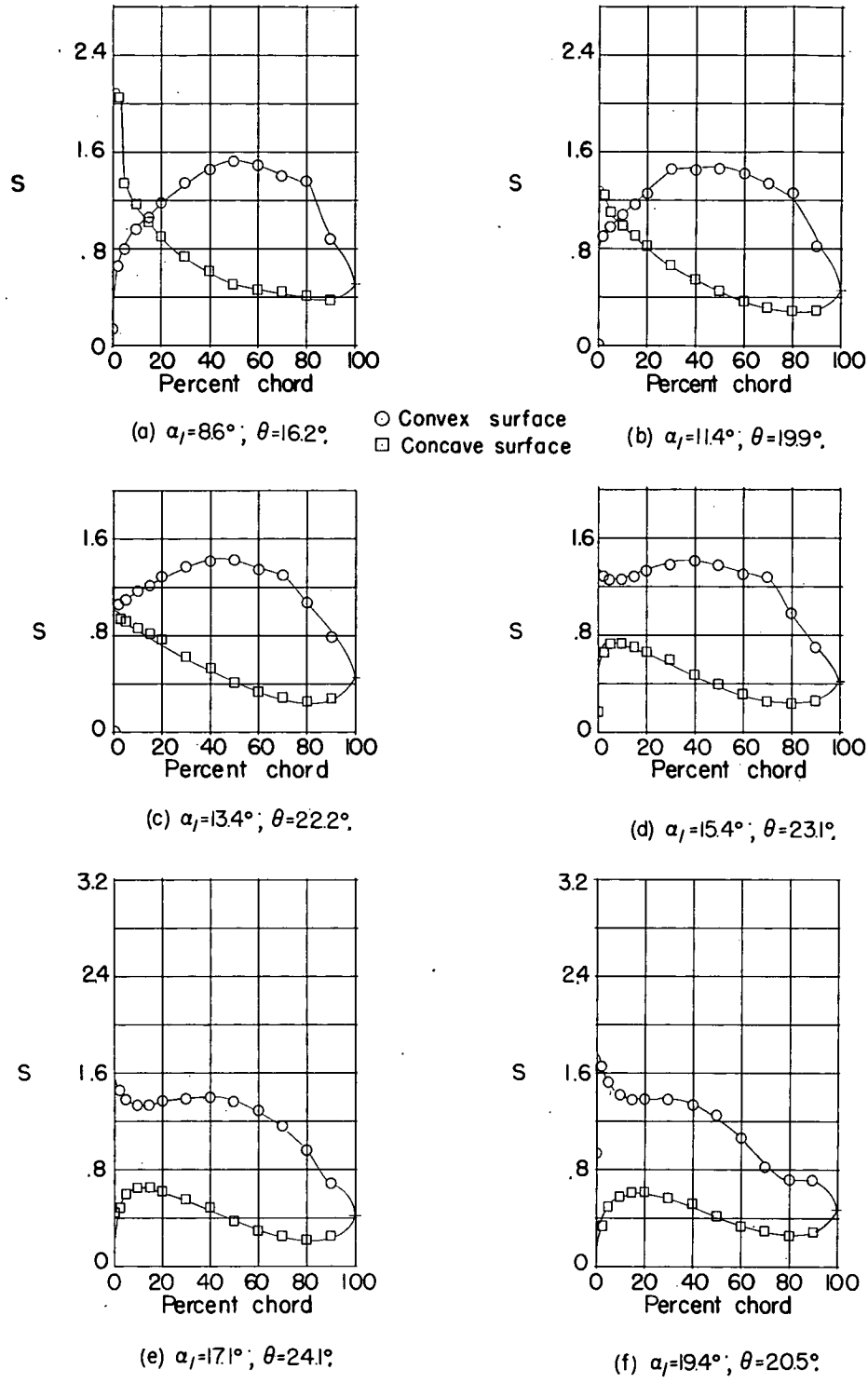

Figure 26.- Blade-surface pressure distributions and blade-section characteristics for the cascade combination $\beta_1 = 60^\circ$ and $\sigma = 1.0$ and NACA 65-$(18A_2I_{8b})$10 blade section.

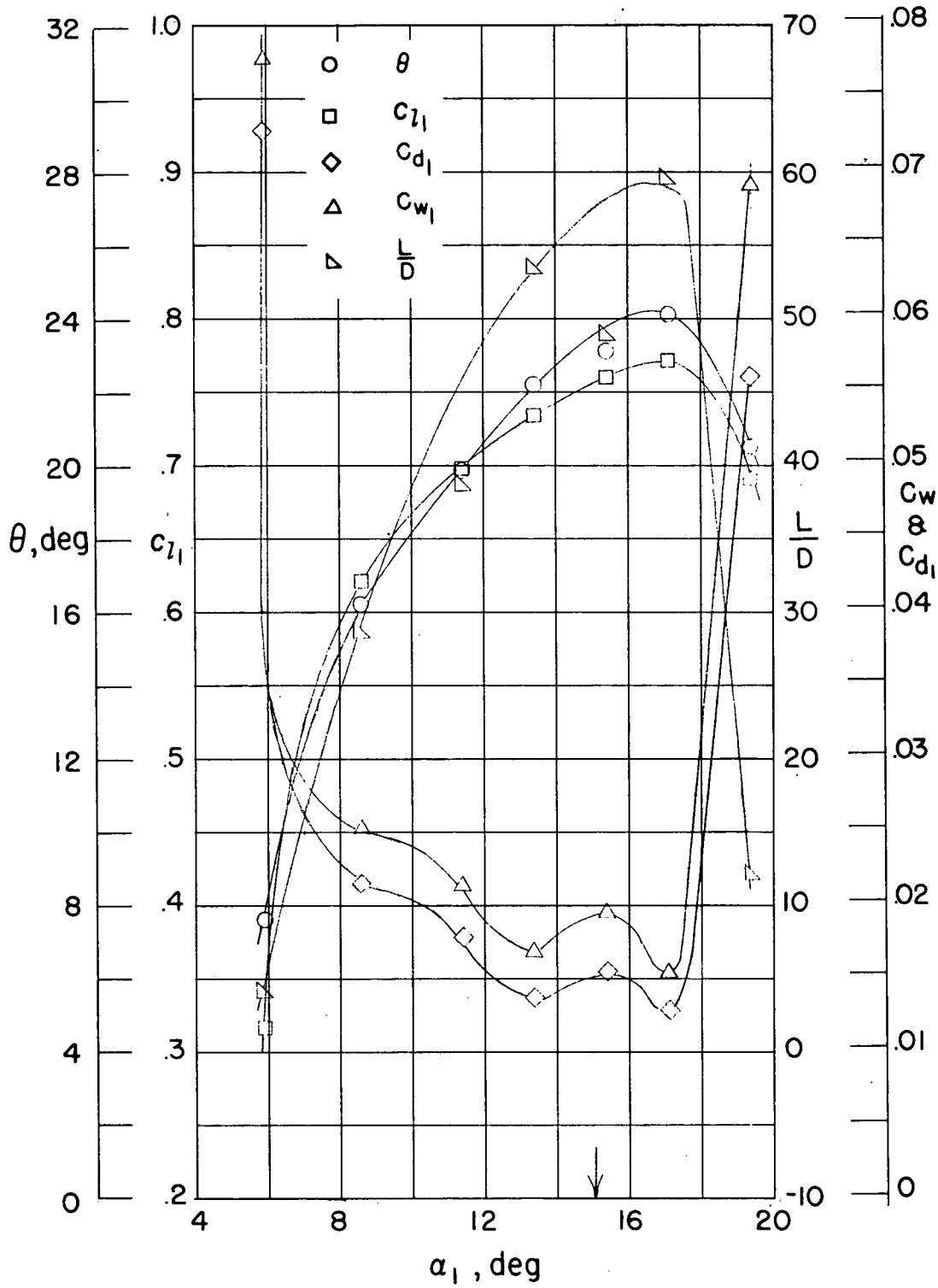

(g) Section characteristics. Arrow shows design angle of attack.

Figure 26.- Concluded.

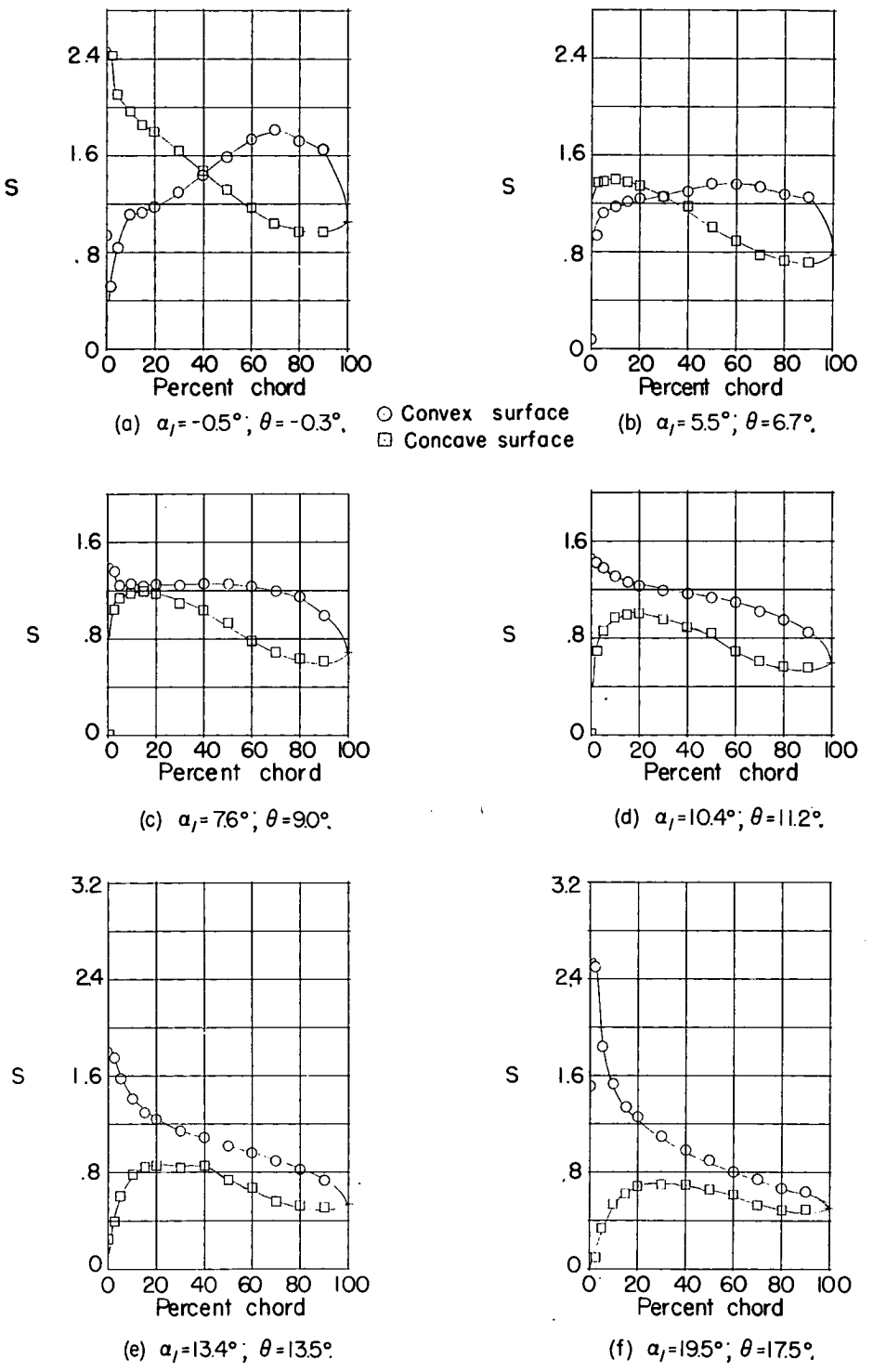

Figure 27.- Blade-surface pressure distributions and blade-section characteristics for the cascade combination $\beta_1 = 60^\circ$ and $\sigma = 1.5$ and NACA 65-$(4A_2I_{8b})$10 blade section.

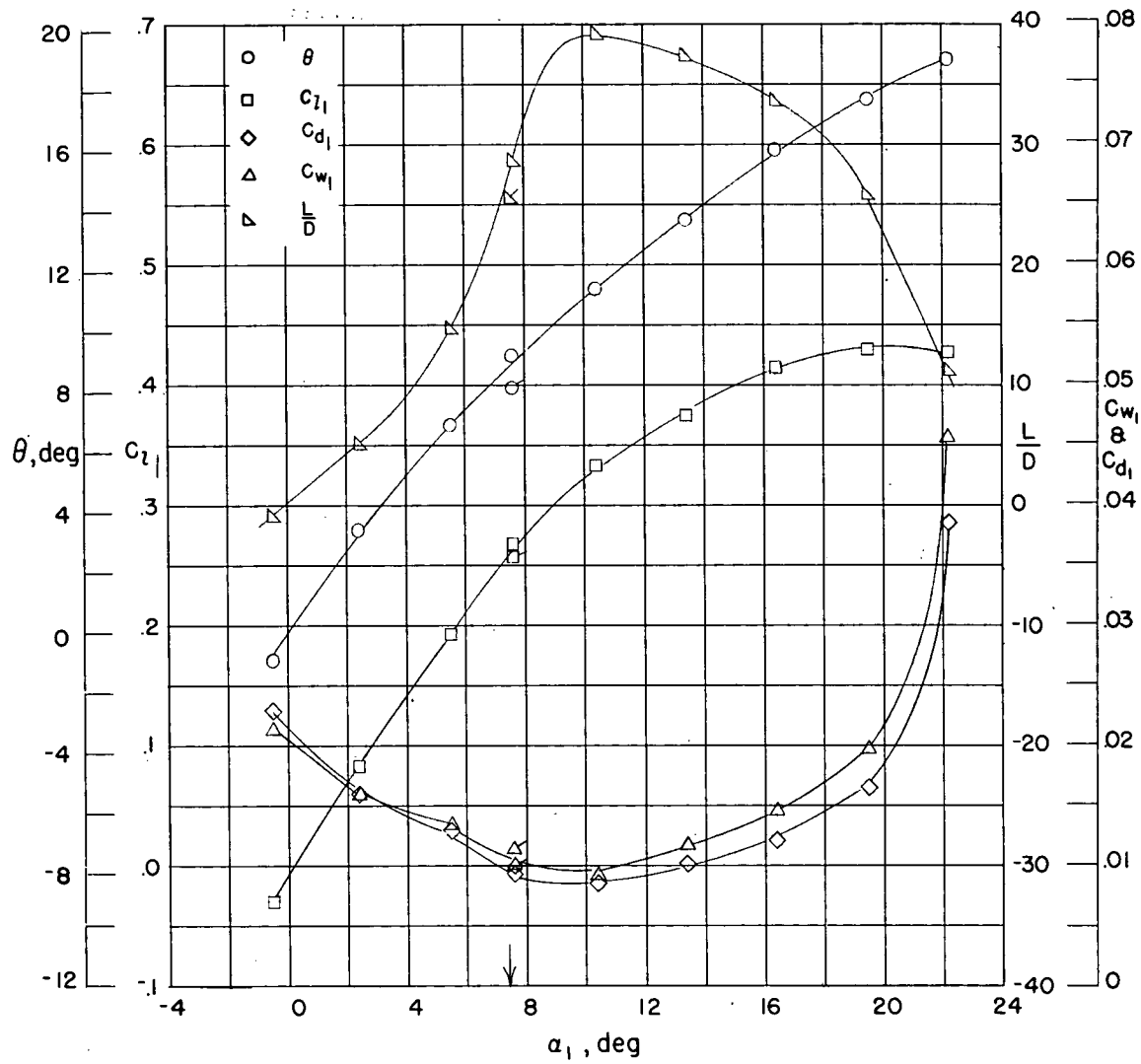

(g) Section characteristics. Arrow shows design angle of attack; flagged symbol indicates roughness.

Figure 27.- Concluded.

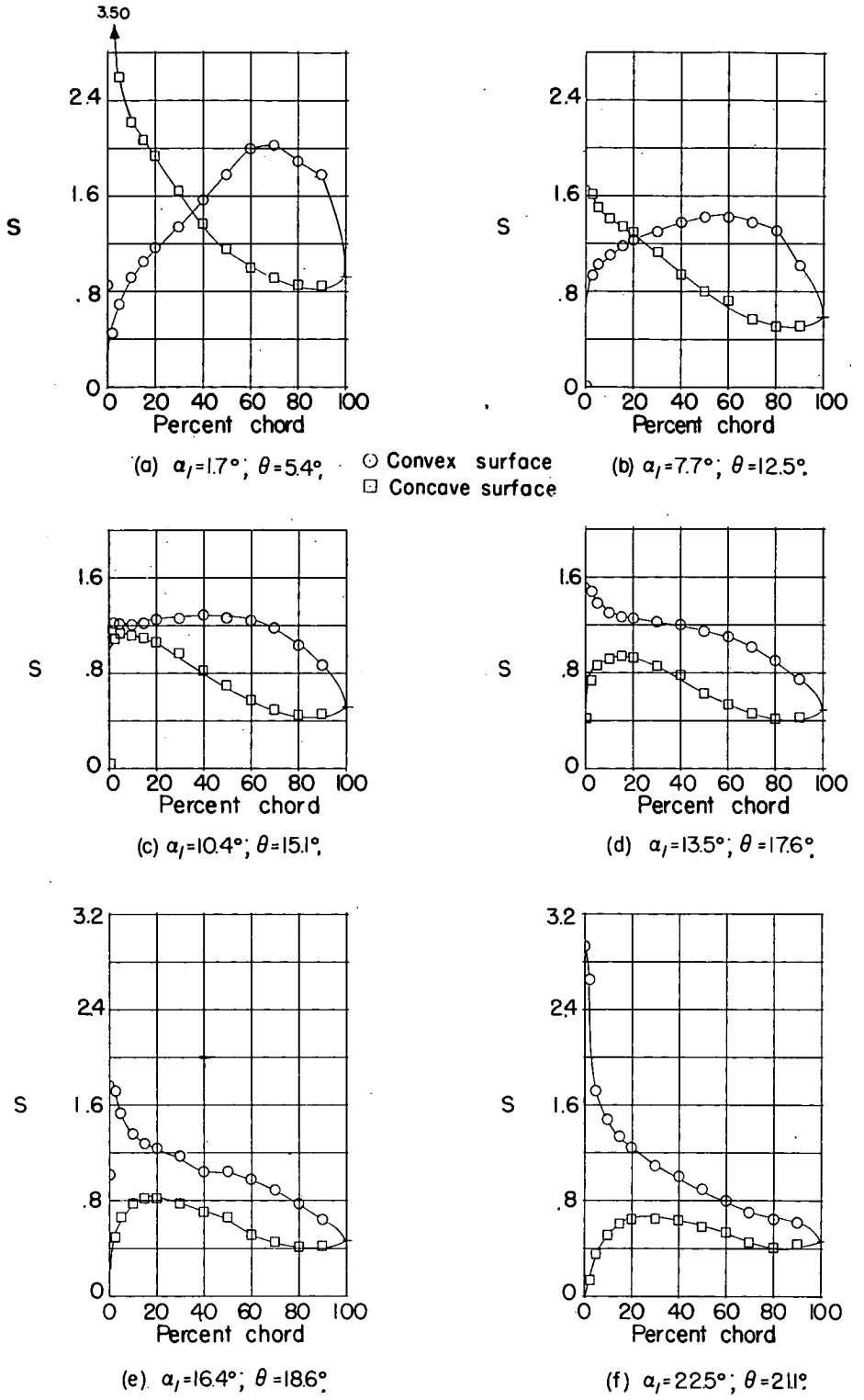

Figure 28.- Blade-surface pressure distributions and blade-section characteristics for the cascade combination $\beta_1 = 60^\circ$ and $\sigma = 1.5$ and NACA 65-$(8A_2I_{8b})$10 blade section.

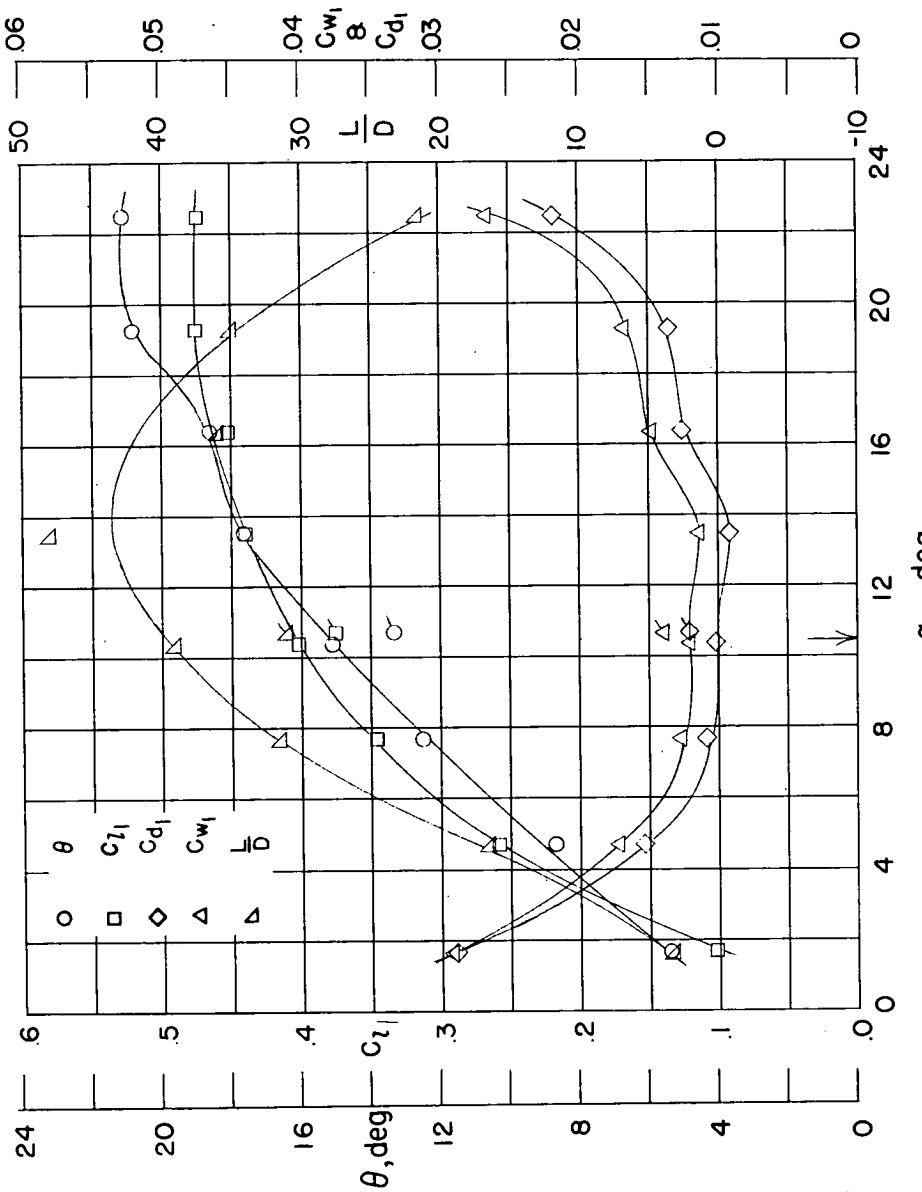

(g) Section characteristics. Arrow shows design angle of attack; flagged symbol indicates roughness.

Figure 28.- Concluded.

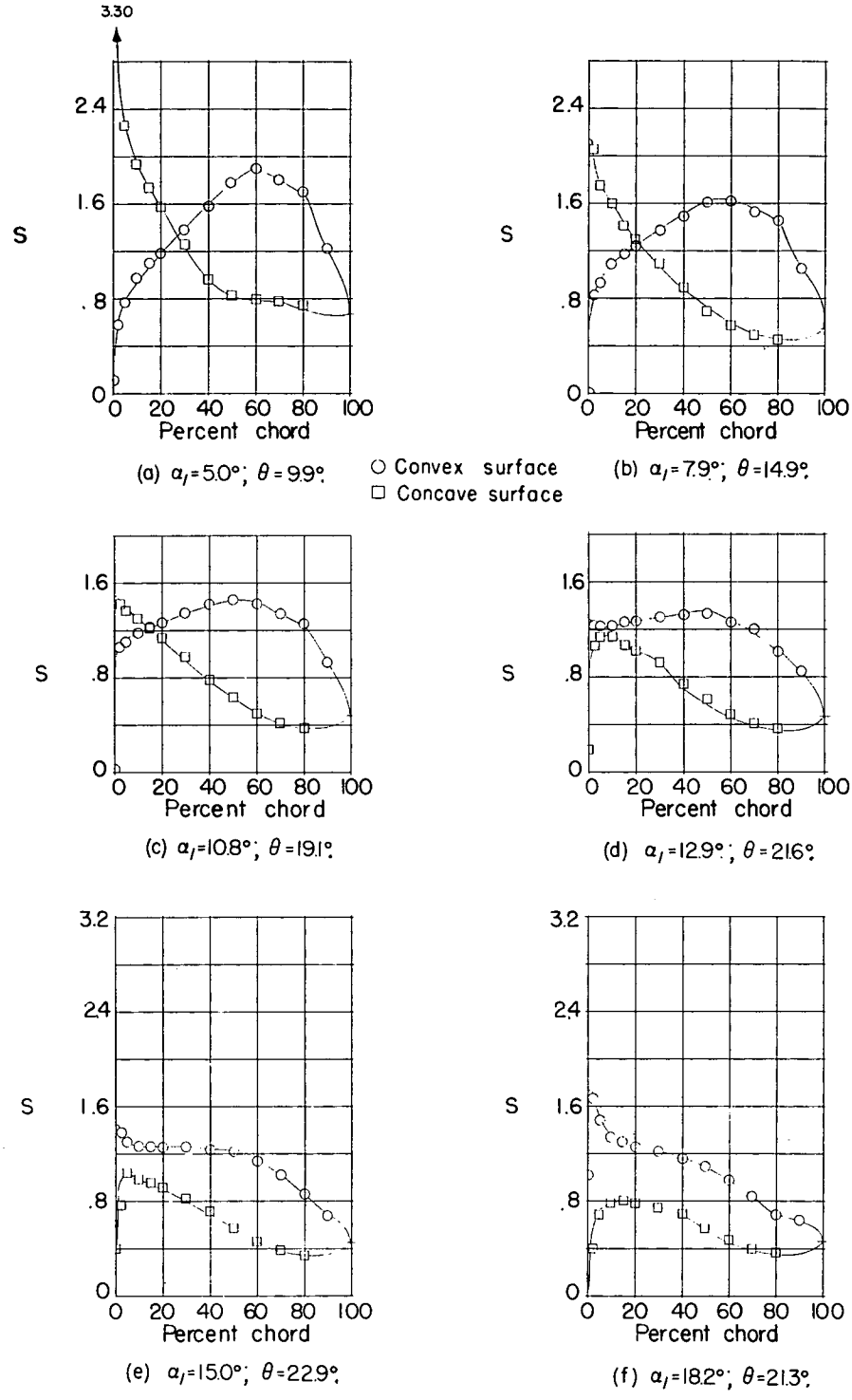

Figure 29.- Blade-surface pressure distributions and blade-section characteristics for the cascade combination $\beta_1 = 60^\circ$ and $\sigma = 1.5$ and NACA 65-$(12A_2I_{8b})$ 10 blade section.

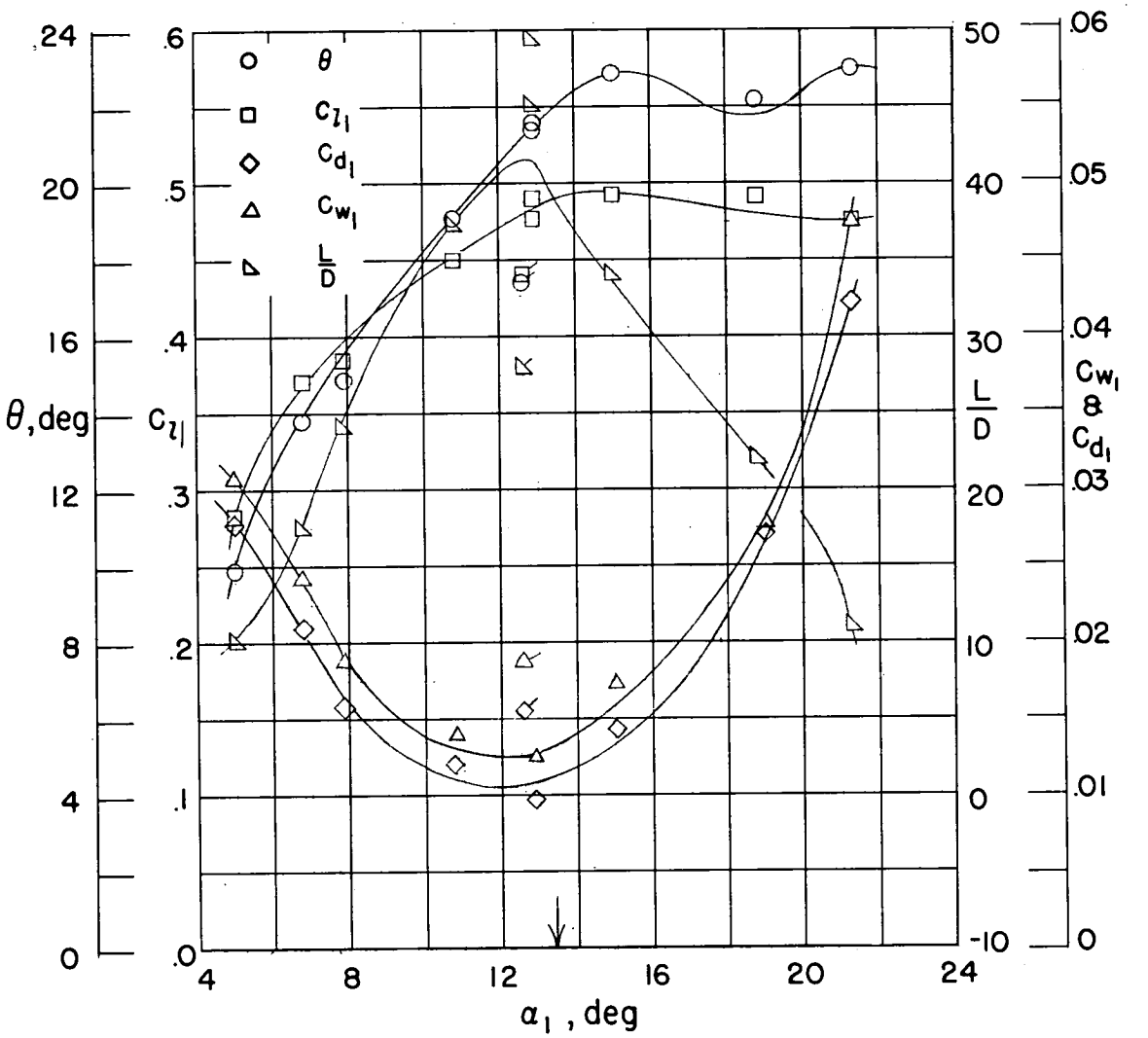

(g) Section characteristics. Arrow shows design angle of attack; flagged symbol indicates roughness.

Figure 29.- Concluded.

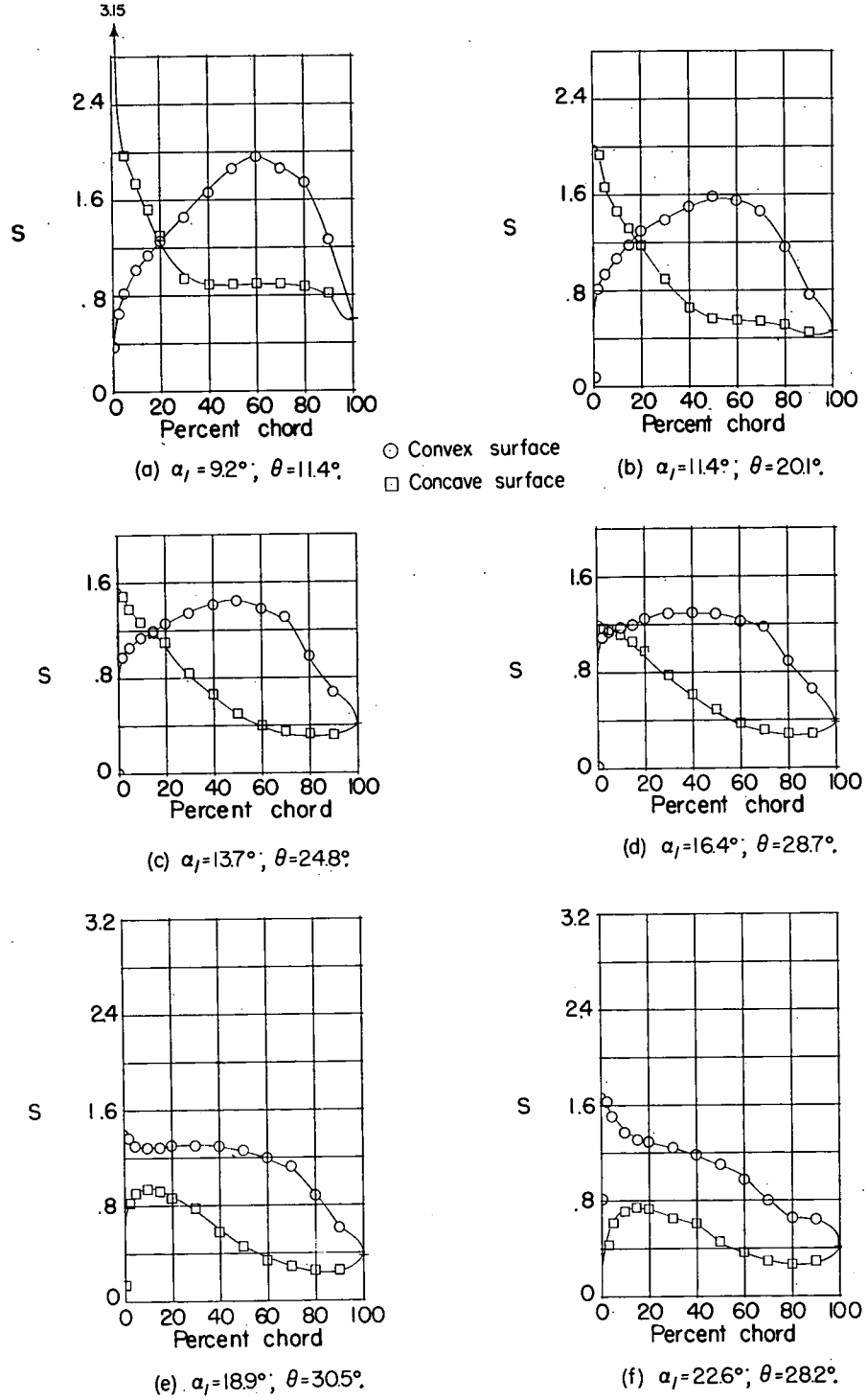

Figure 30.- Blade-surface pressure distributions and blade-section characteristics for the cascade combination $\beta_1 = 60^\circ$ and $\sigma = 1.5$ and NACA 65-$\left(18A_2I_{8b}\right)$10 blade section.

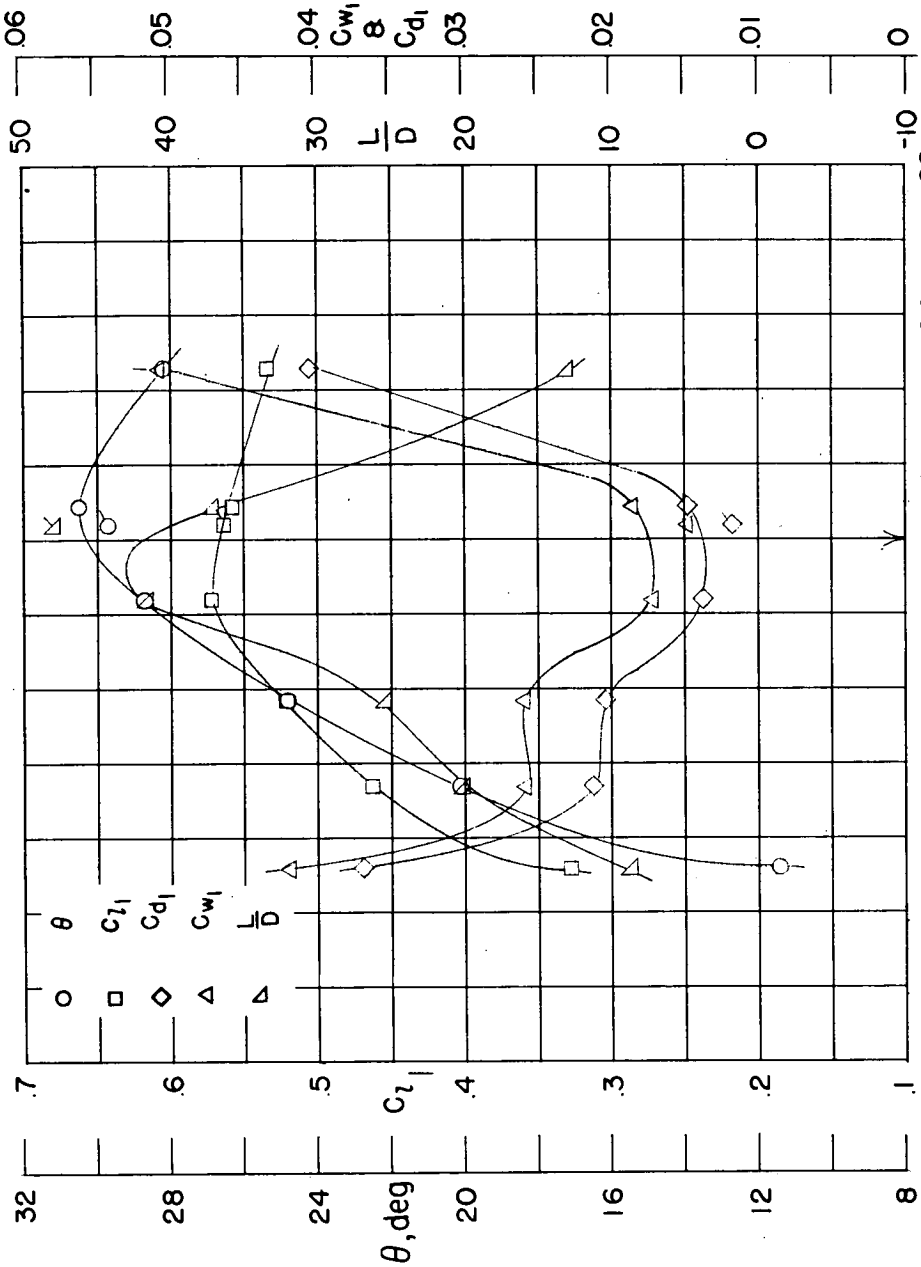

(g) Section characteristics. Arrow shows design angle of attack; flagged symbol indicates roughness.

Figure 30.- Concluded.

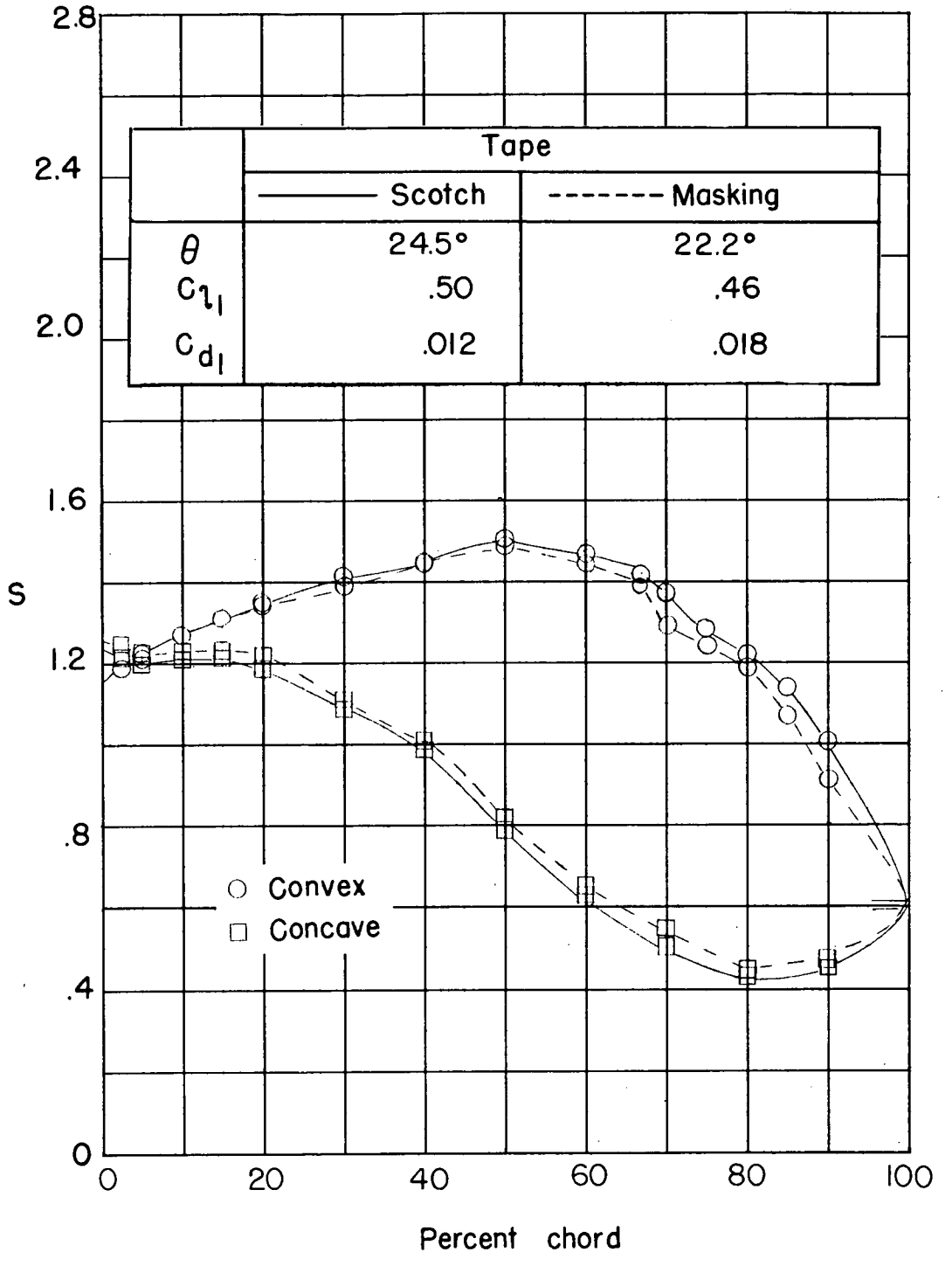

Figure 31.- Comparison of blade-surface pressure distribution and performance data for the NACA 65-$(12A_2I_{8b})$10 blade section at $\beta = 45^\circ$ and $\sigma = 1.5$ at $\alpha = 12.9^\circ$ with 1/16-inch Scotch tape or 1/16-inch masking tape at 35-percent-chord station on convex surface as surface roughness.

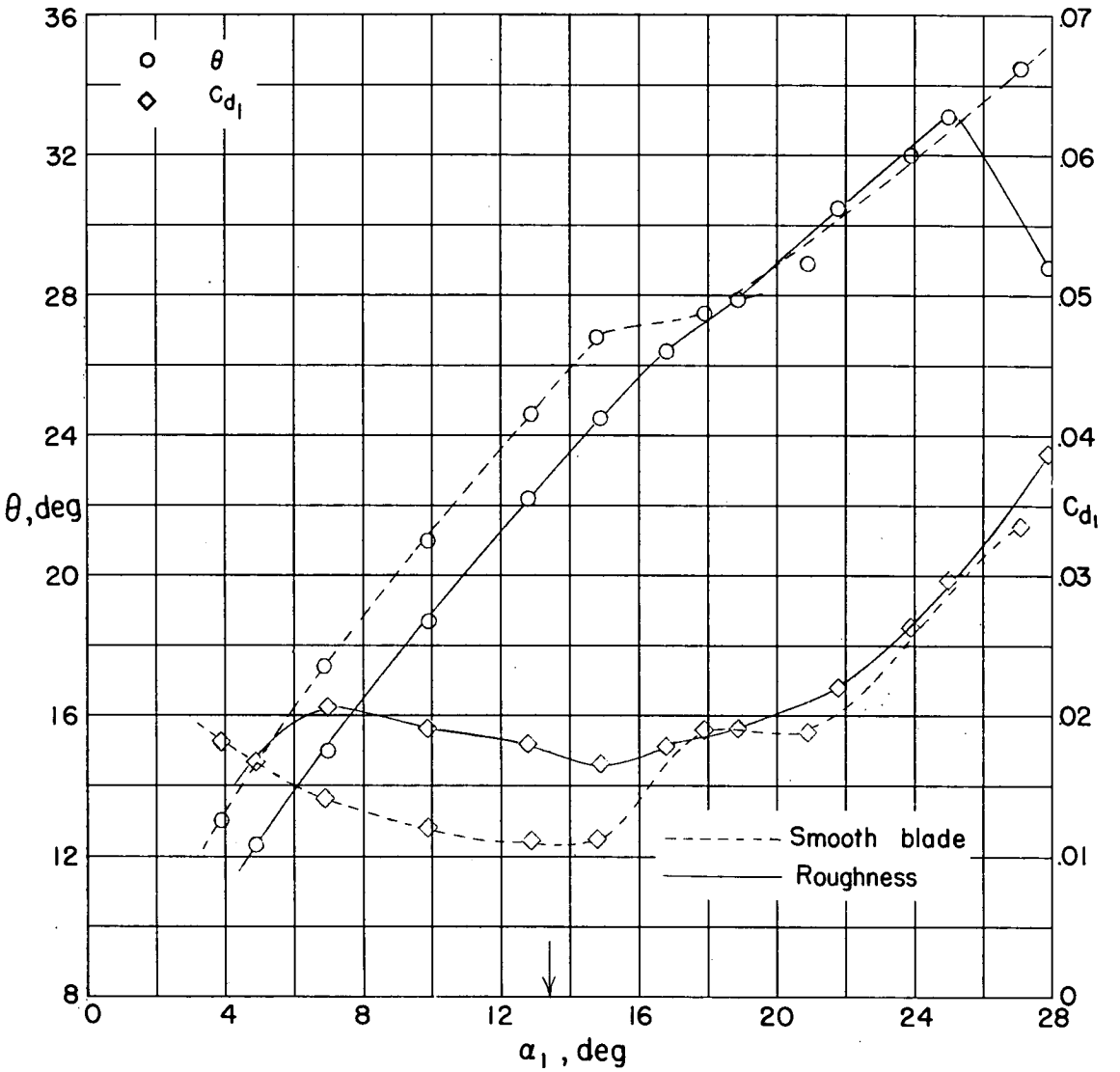

Figure 32.- Section characteristics for the cascade combination $\beta = 45^\circ$ and $\sigma = 1.5$ and NACA 65-$(12A_2I_{8b})$10 blade section with roughness in the form of a 1/16-inch strip of masking tape at 35-percent-chord station on the convex surface added.

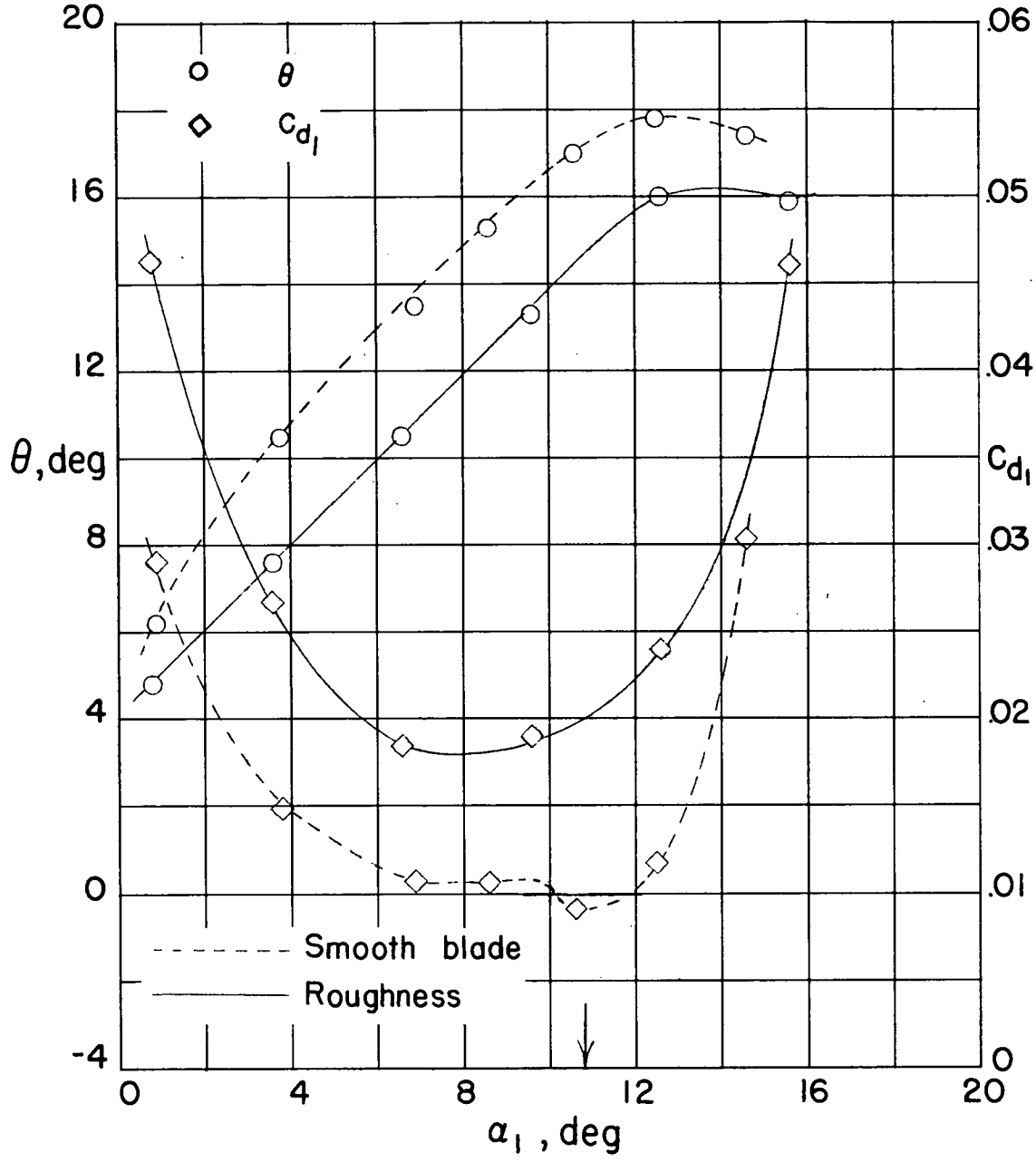

Figure 33.- Section characteristics for the cascade combination $\beta = 60^\circ$ and $\sigma = 1.0$ and NACA 65-$(12A_2I_{8b})$10 blade section with roughness in the form of a 1/16-inch strip of masking tape at 35-percent-chord station on the convex surface added.

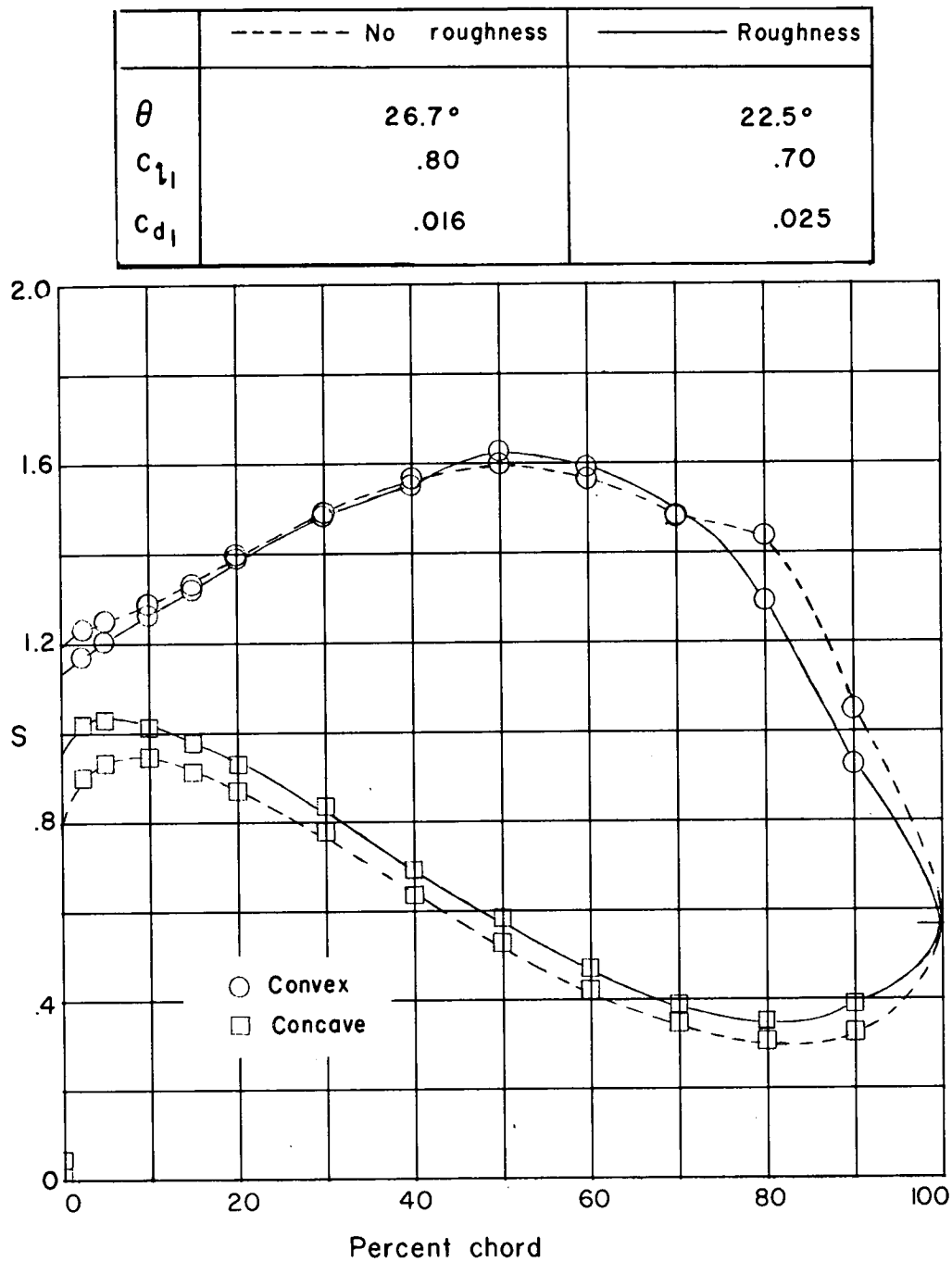

Figure 34.- Comparison of blade-surface pressure distributions and performance data for the NACA 65-$\left(18A_2I_{8b}\right)$10 blade section at $\beta = 45^\circ$ and $\sigma = 1.0$ at $\alpha = 14.3^\circ$ with no roughness and at $\alpha = 13.5^\circ$ with 1/16-inch strip of masking tape at 35-percent-chord station on the convex surface as surface roughness.

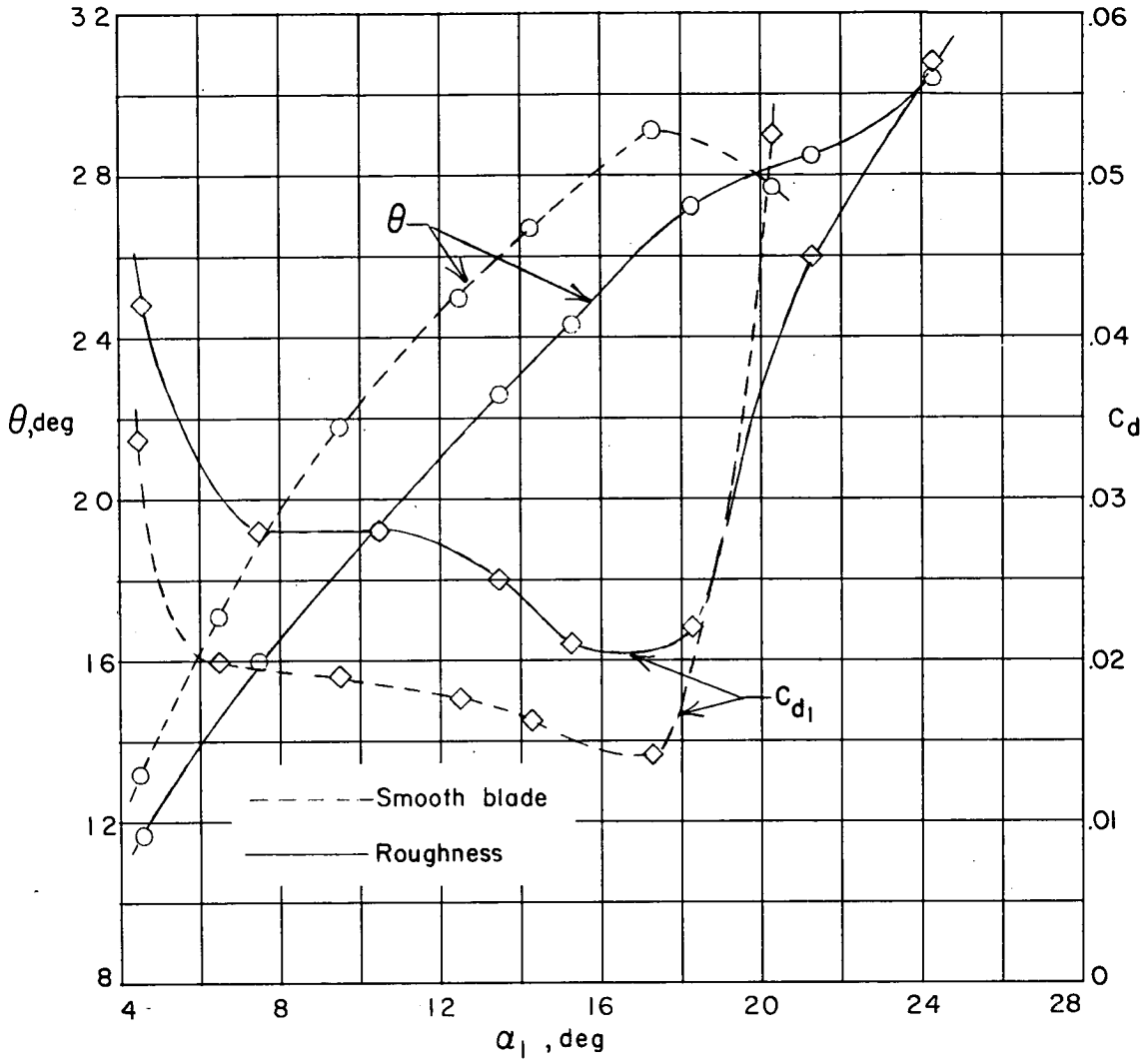

Figure 35.- Section characteristics for the cascade combination $\beta = 45^\circ$ and $\sigma = 1.0$ and NACA 65-$(18A_2I_{8b})$10 blade section with roughness in the form of a 1/16-inch strip of masking tape at 35-percent-chord station on the convex surface as surface roughness.

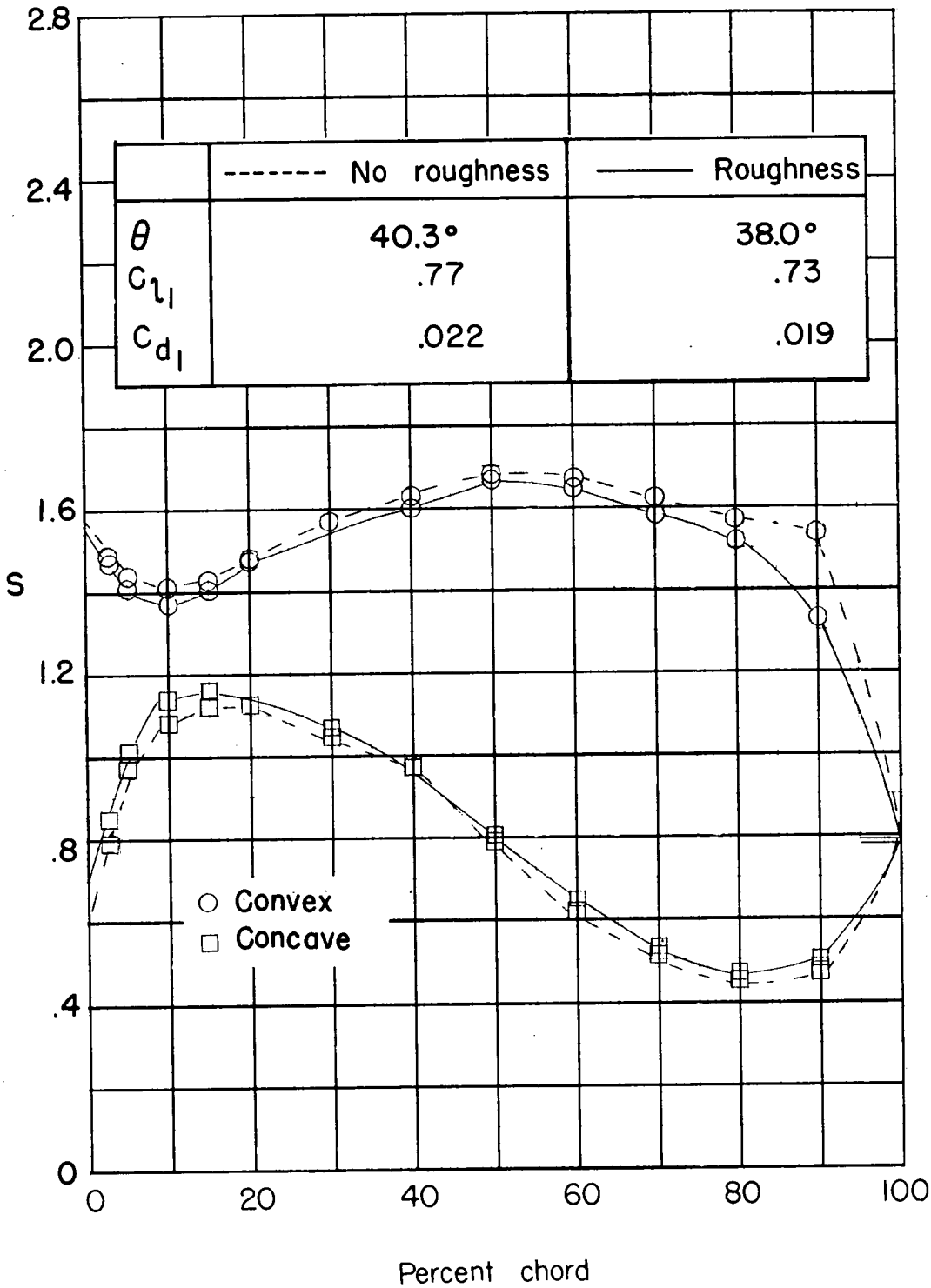

Figure 36.- Comparison of blade-surface pressure distributions and performance data for the NACA 65-$(18A_2I_{8b})$10 blade section at $\beta = 30^\circ$ and $\sigma = 1.5$ at $\alpha = 18.5$ with no roughness and $\alpha = 18.6$ with No. 600 carborundum paper draped over the forward 35 percent of the blade.

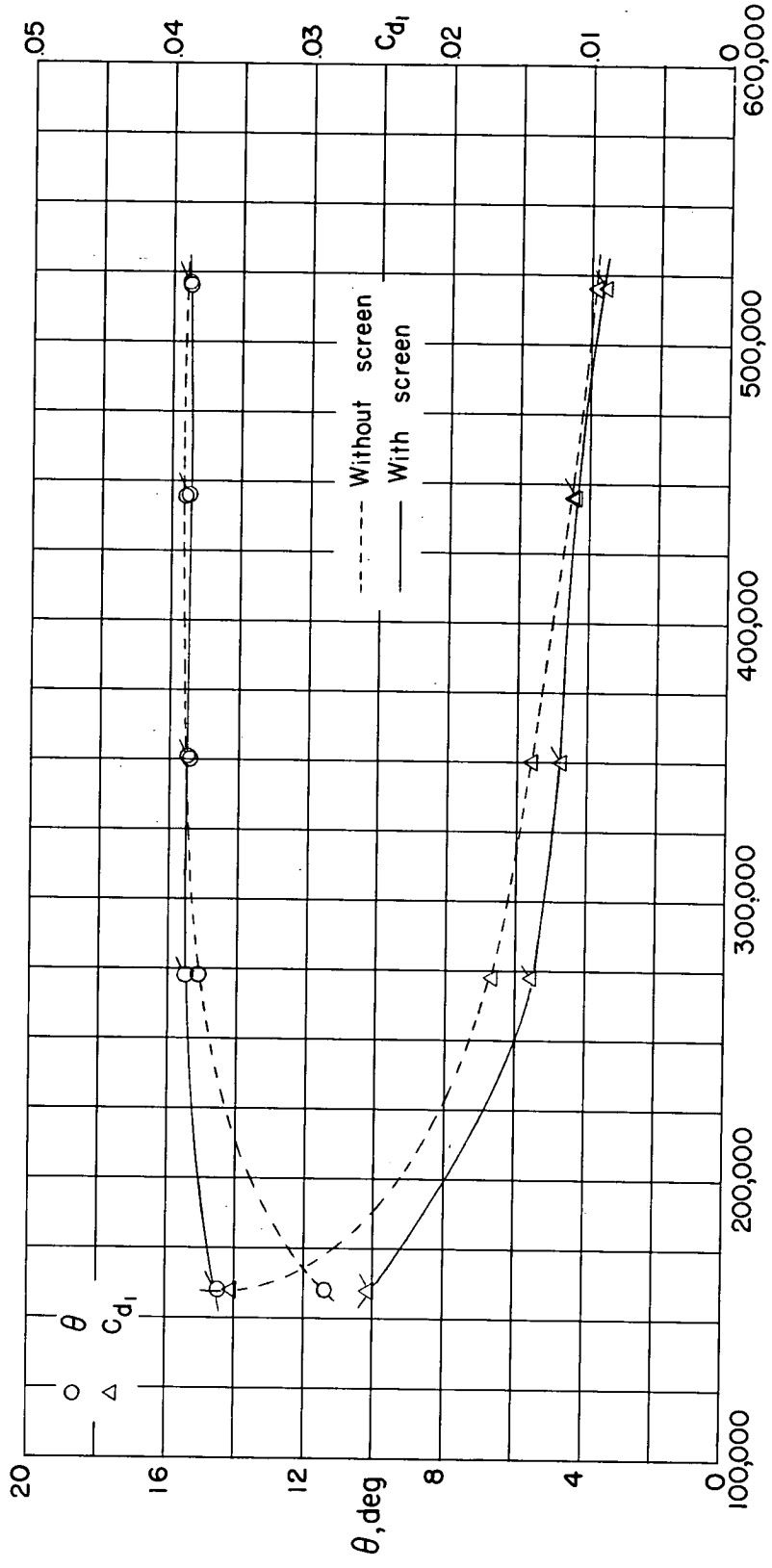

Figure 37.- Effect of Reynolds number on turning angle and drag coefficient for the cascade combination $\beta = 60^{\circ}$ and $\sigma = 1.0$ and NACA $65\text{-}(12A_2I_{8b})10$ blade section with and without turbulence screen at $\alpha = 9.6^{\circ}$.

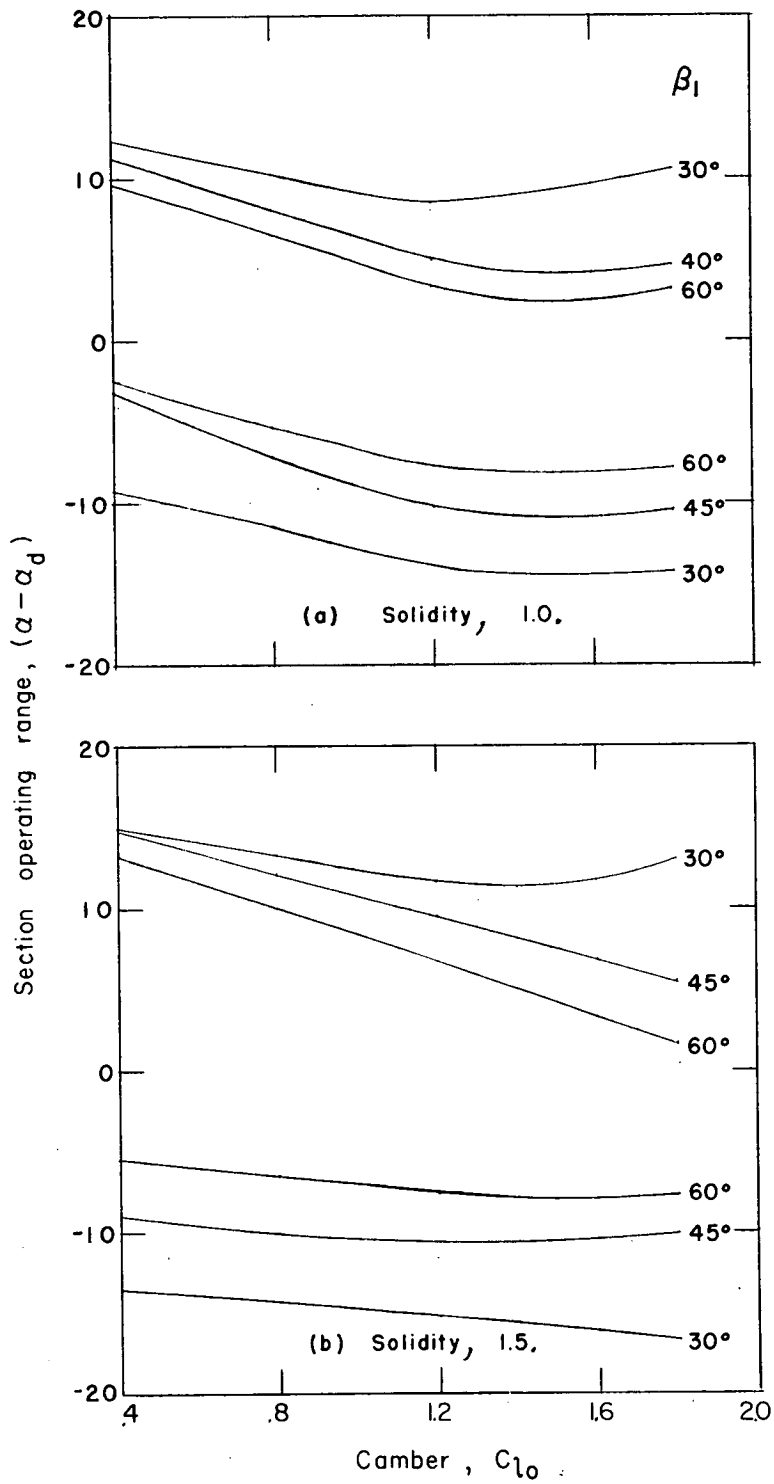

Figure 38.- Variation of estimated angle-of-attack operating range with camber for inlet angles of 30°, 45°, and 60° at $\sigma = 1.0$ and 45° and 60° at $\sigma = 1.5$ for the A_2I_{8b} blades.

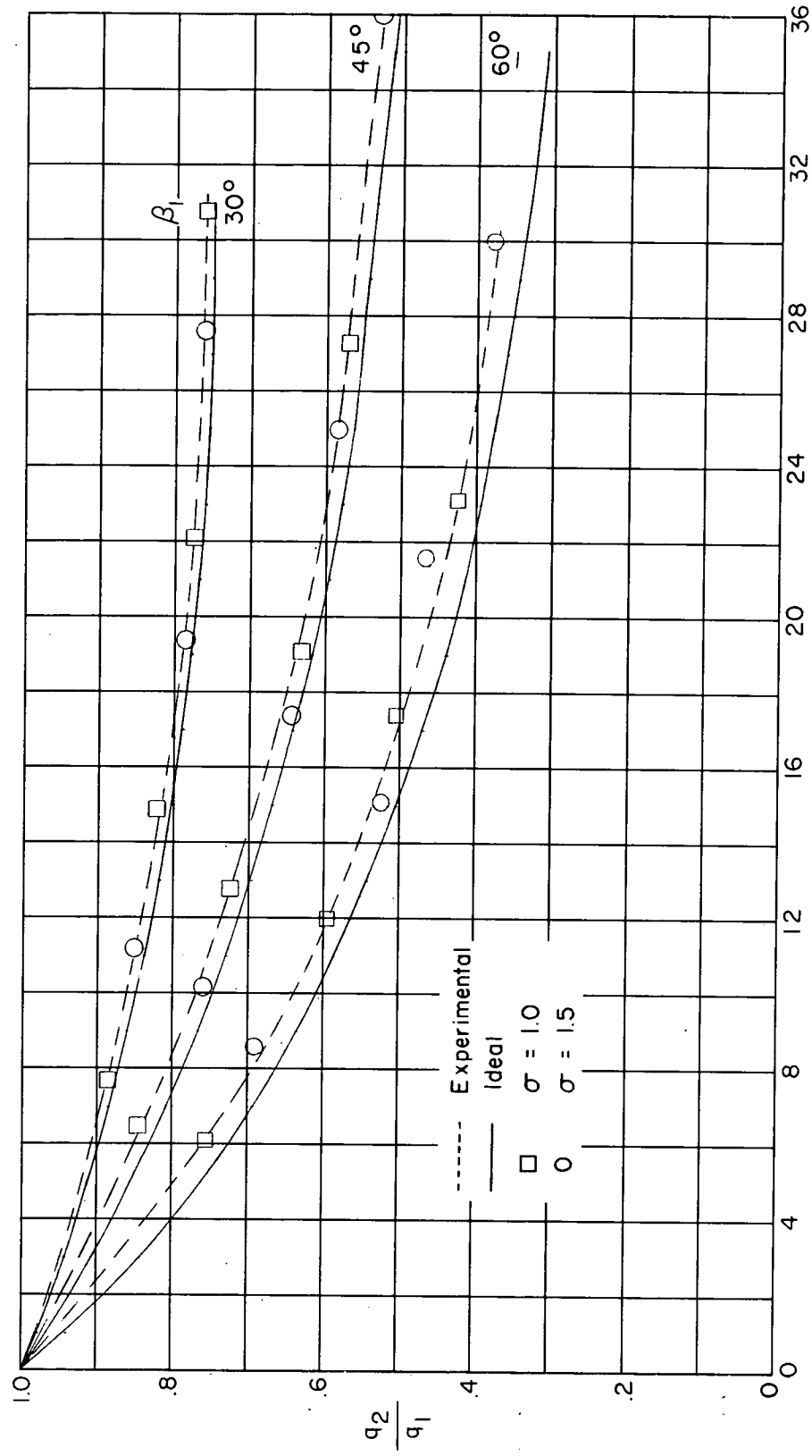

Figure 39.- Variation of experimental and ideal dynamic-pressure ratios across the cascade at α_d.

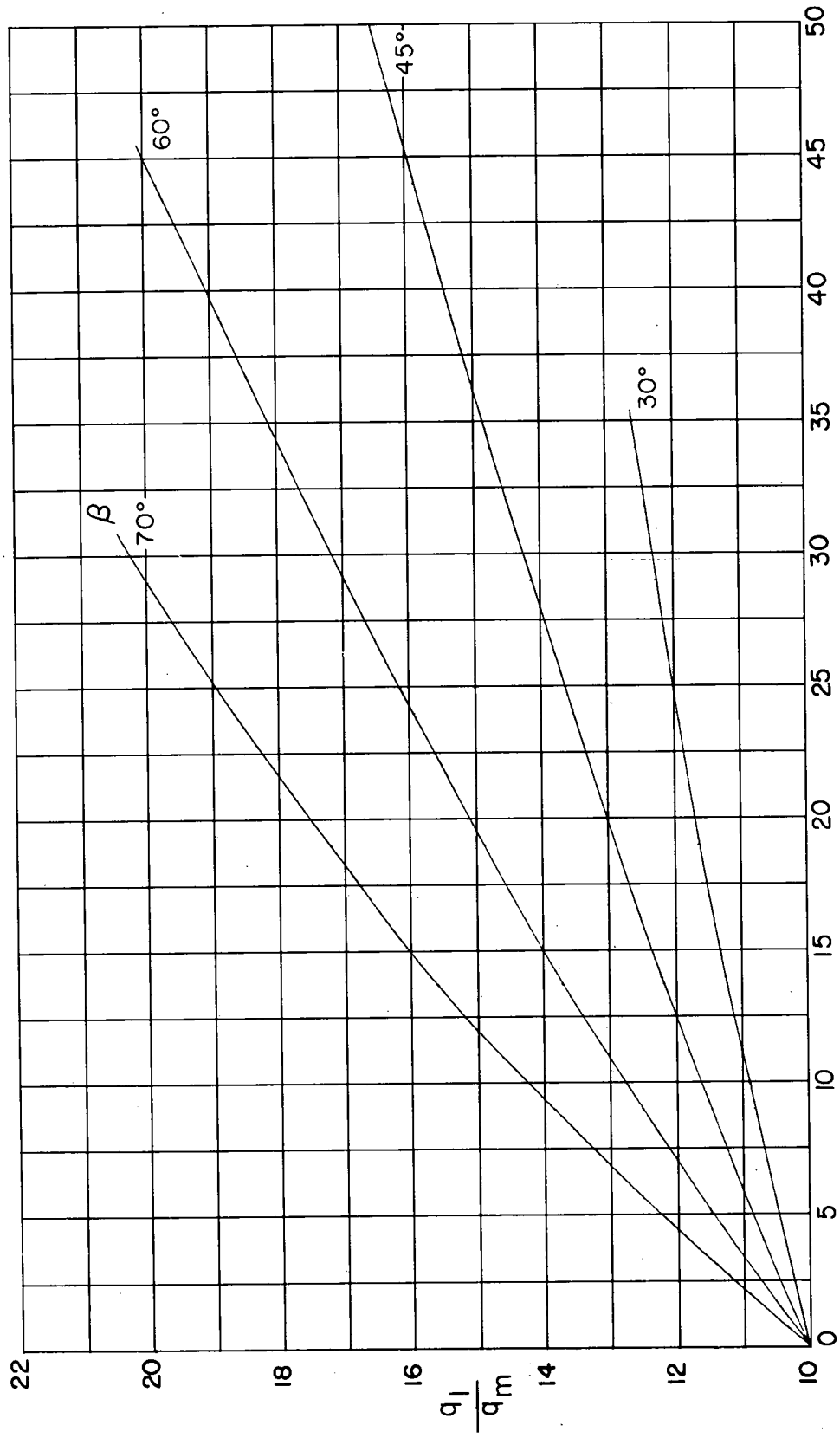

Figure 40.- Conversion chart showing relationship between entering and mean dynamic pressure as a function of turning angle and inlet angle.

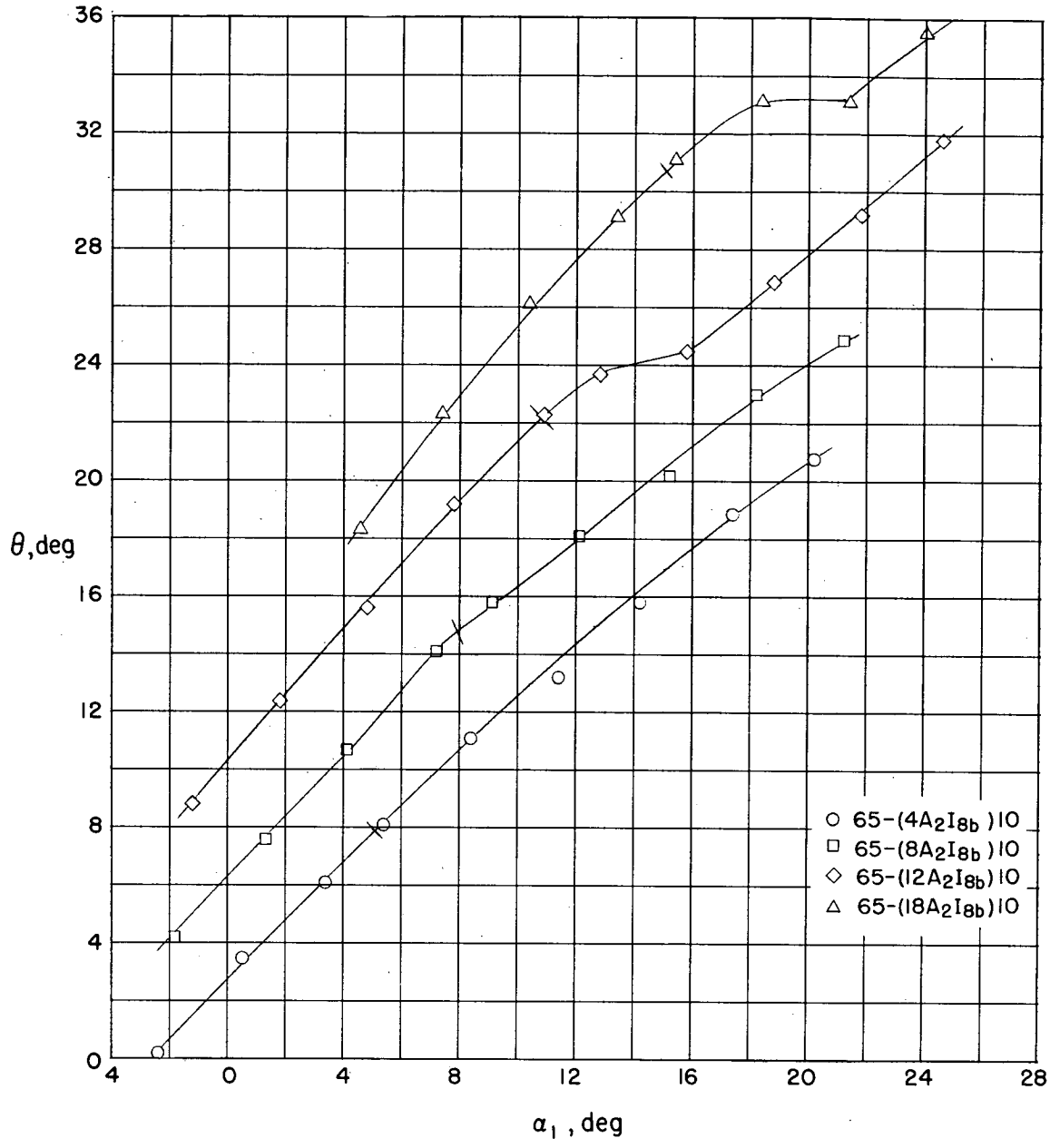

Figure 41.- Summary of turning angle θ, angle of attack α, and relationship for blade sections tested at $\beta_1 = 30^\circ$ with $\sigma = 1.0$. Short bars across curves indicate design points.

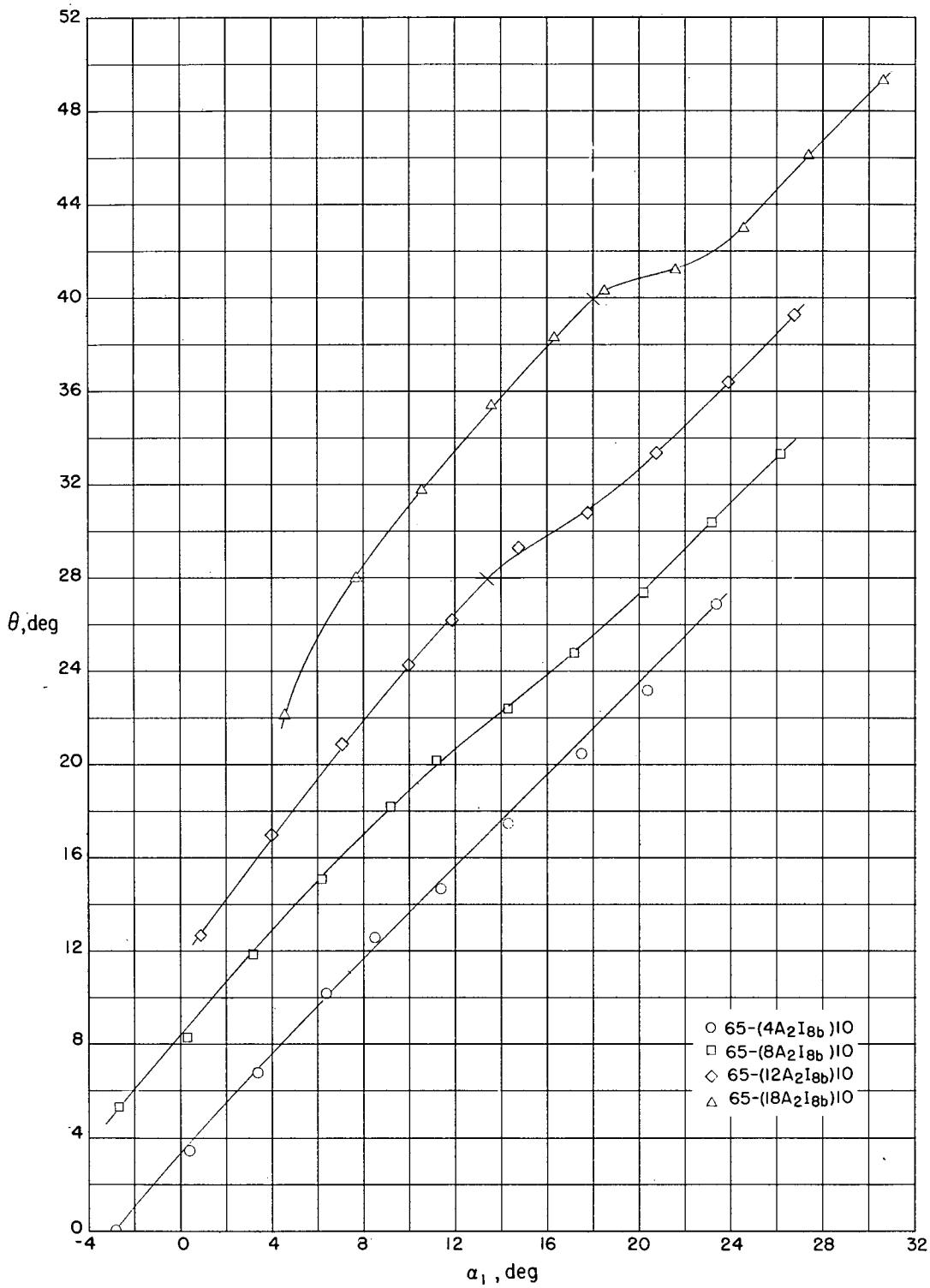

Figure 42.- Summary of turning angle θ, angle of attack α, and relationship for blade sections tested at $\beta_1 = 30^\circ$ with $\sigma = 1.5$. Short bars across curves indicate design points.

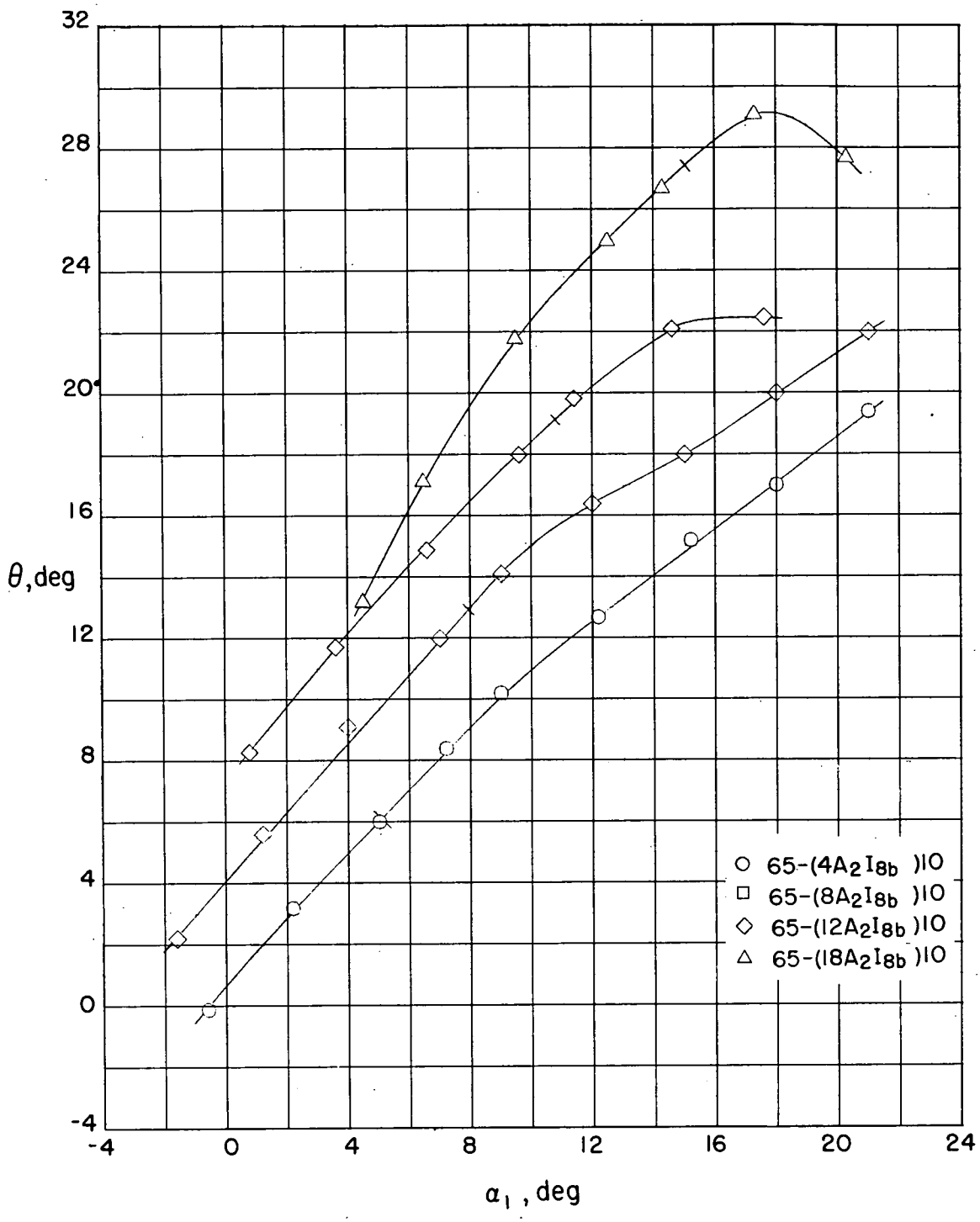

Figure 43.- Summary of turning angle θ, angle of attack α, and relationship for blade sections tested at $\beta_1 = 45^\circ$ with $\sigma = 1.0$. Short bars across curves indicate design points.

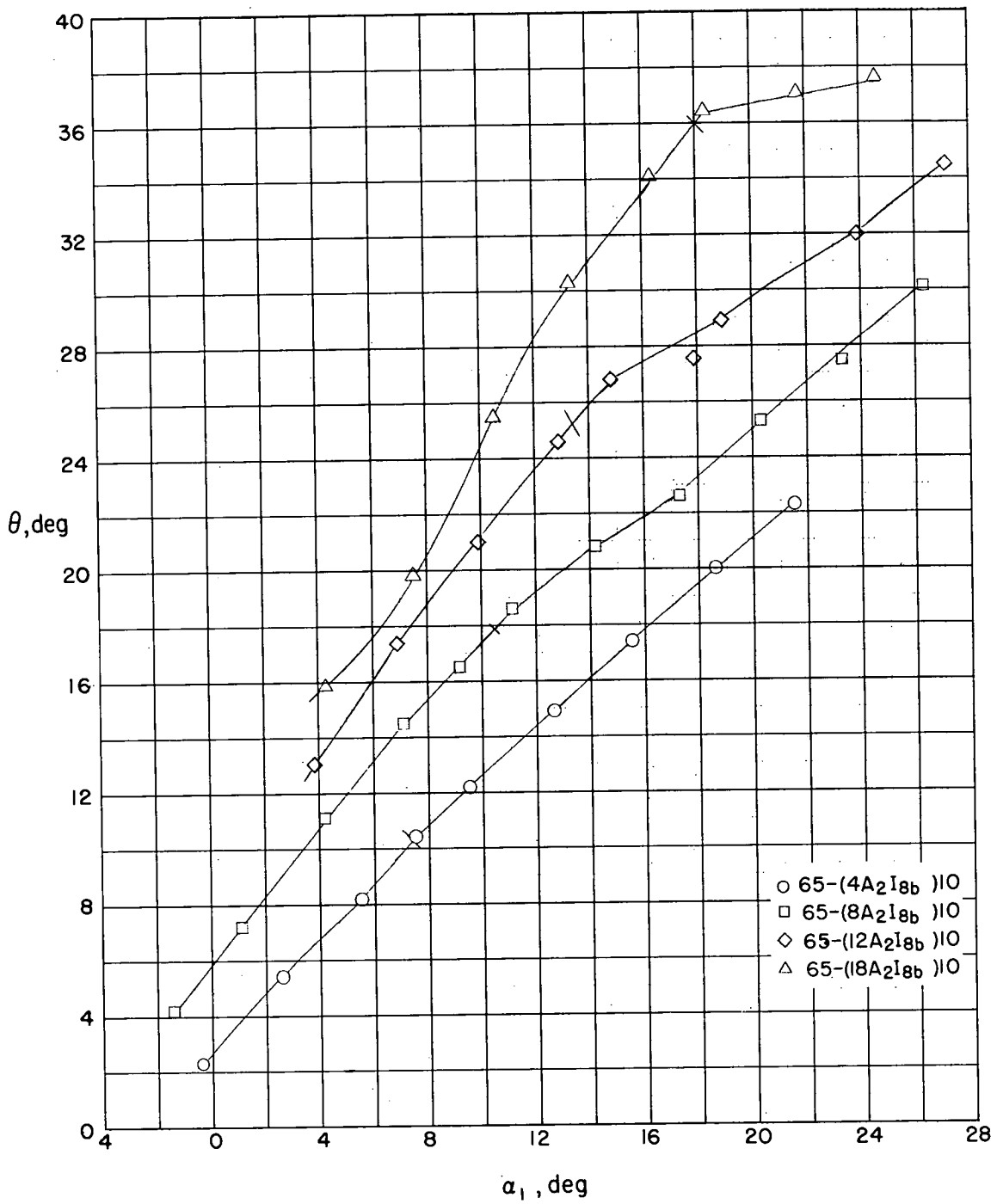

Figure 44.- Summary of turning angle θ, angle of attack α, and relationship for blade sections tested at $\beta_1 = 45^\circ$ with $\sigma = 1.5$. Short bars across curves indicate design points.

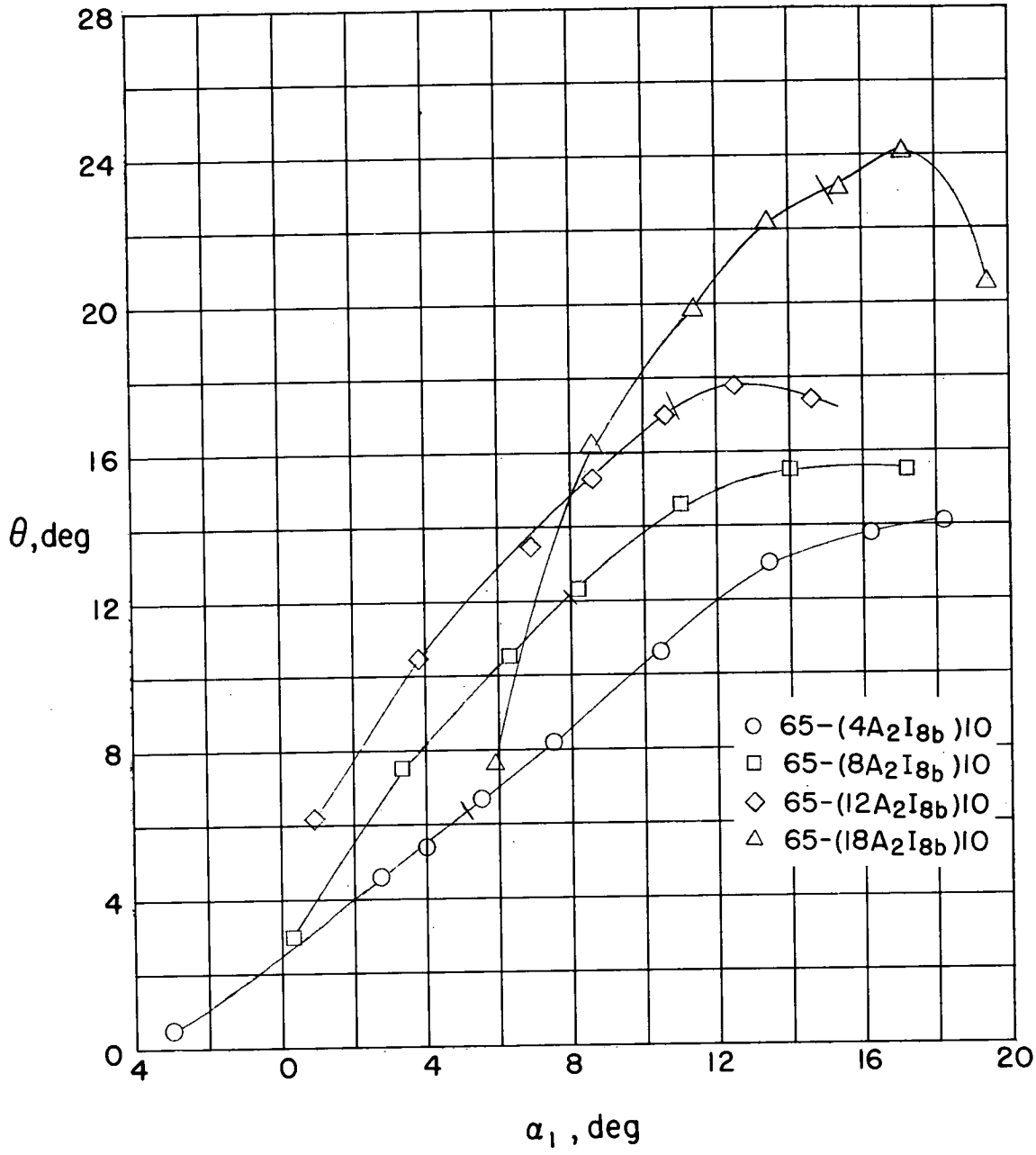

Figure 45.- Summary of turning angle θ, angle of attack α, and relationship for blade sections tested at $\beta_1 = 60^\circ$ with $\sigma = 1.0$. Short bars across curves indicate design points.

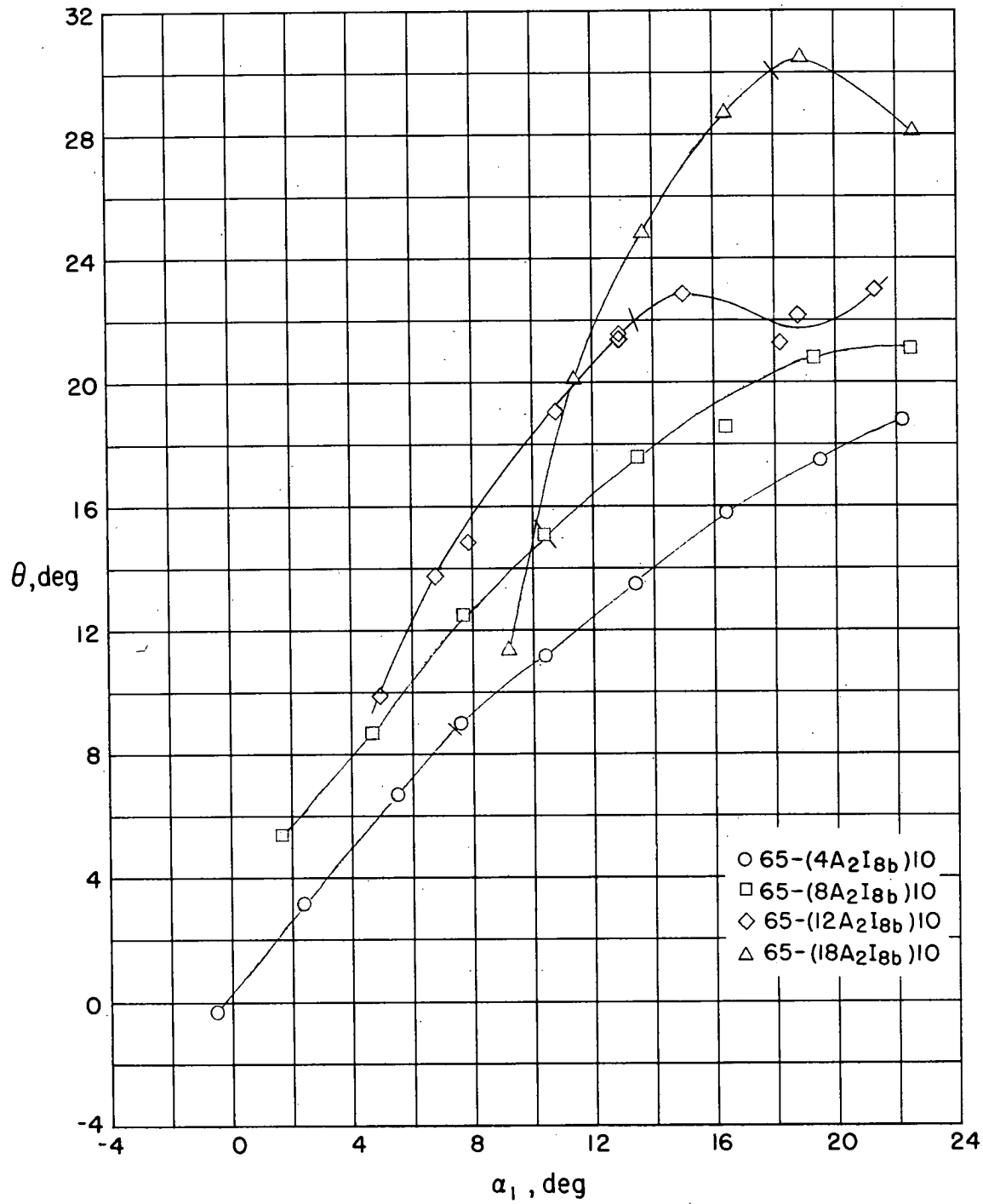

Figure 46.- Summary of turning angle θ, angle of attack α, and relationship for blade sections tested at $\beta_1 = 60^\circ$ with $\sigma = 1.5$. Short bars across curves indicate design points.

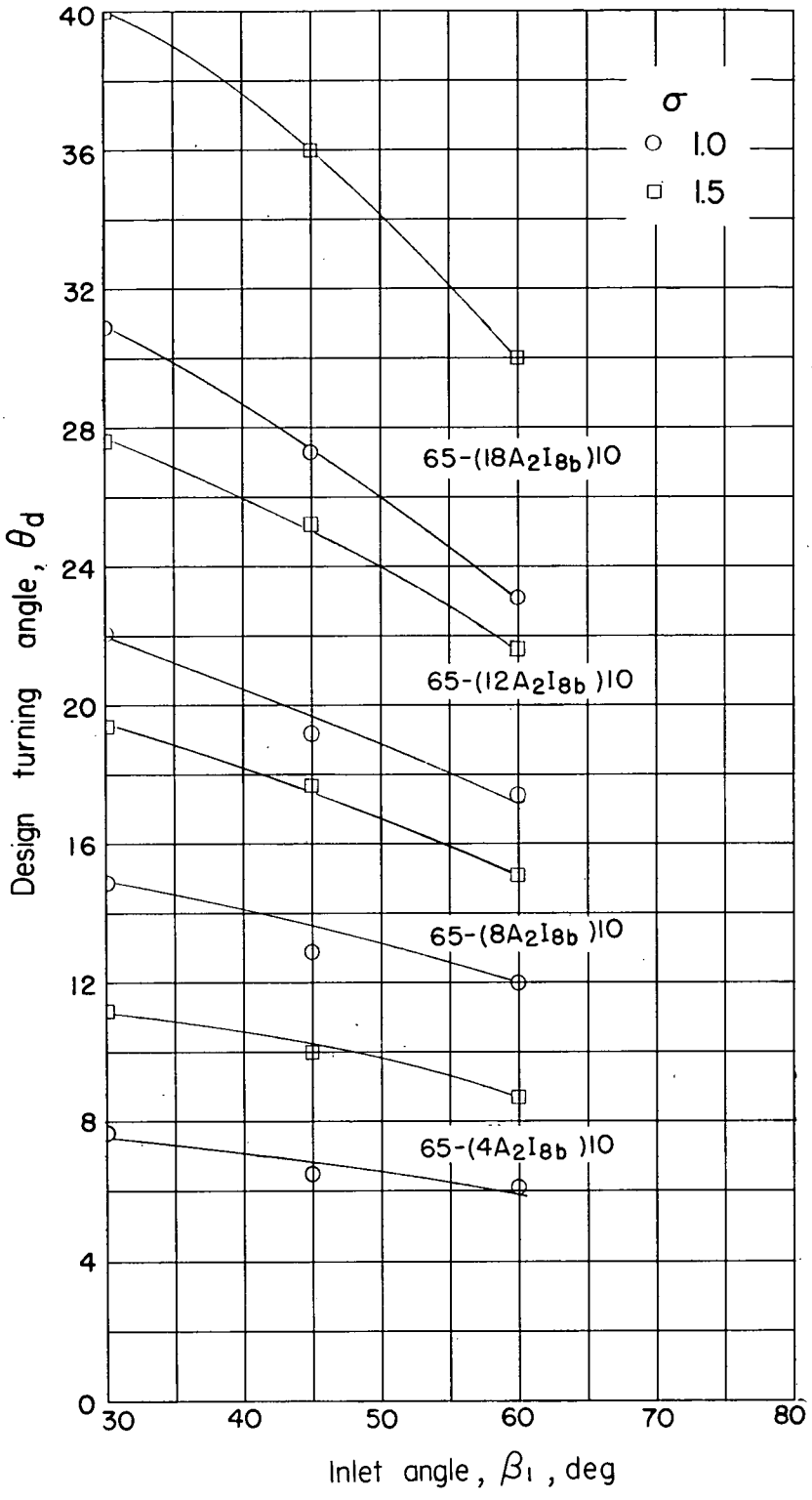

Figure 47.- Variation of design turning angle with inlet angle and solidity for typical sections.

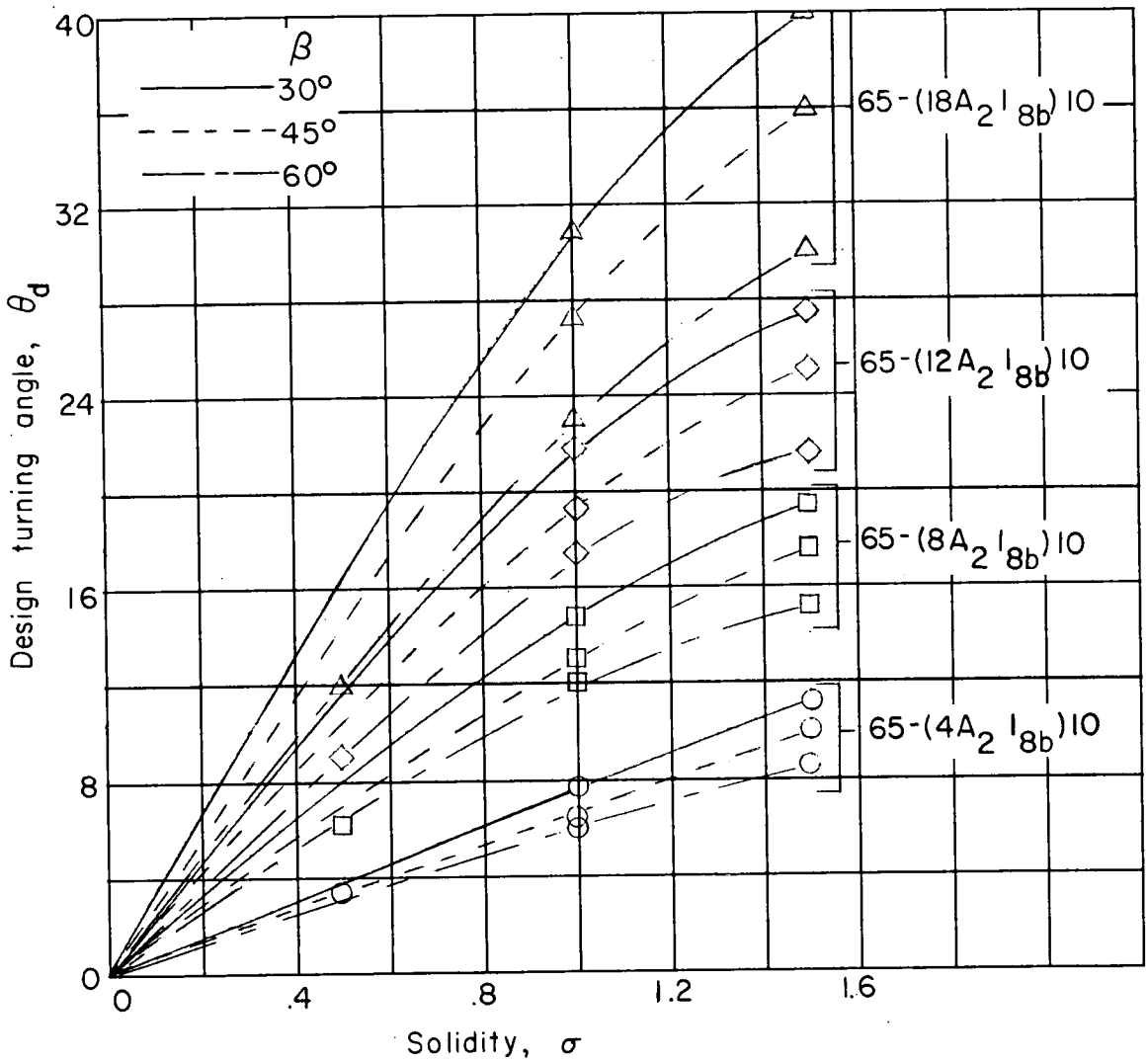

Figure 48.- Variation of design turning angle with solidity and inlet angle for the A_2I_{8b} sections tested.

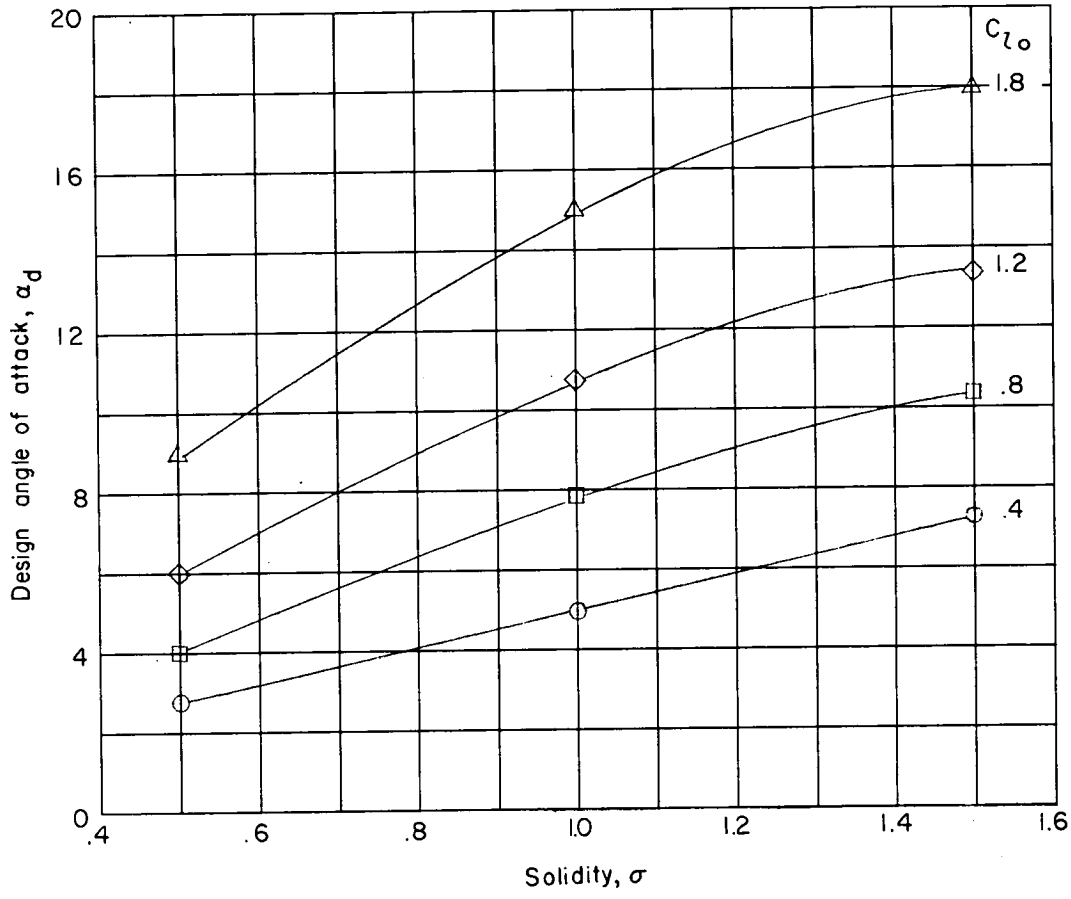

Figure 49.- Variation of design angle of attack with solidity for the A_2I_{8b} sections tested.

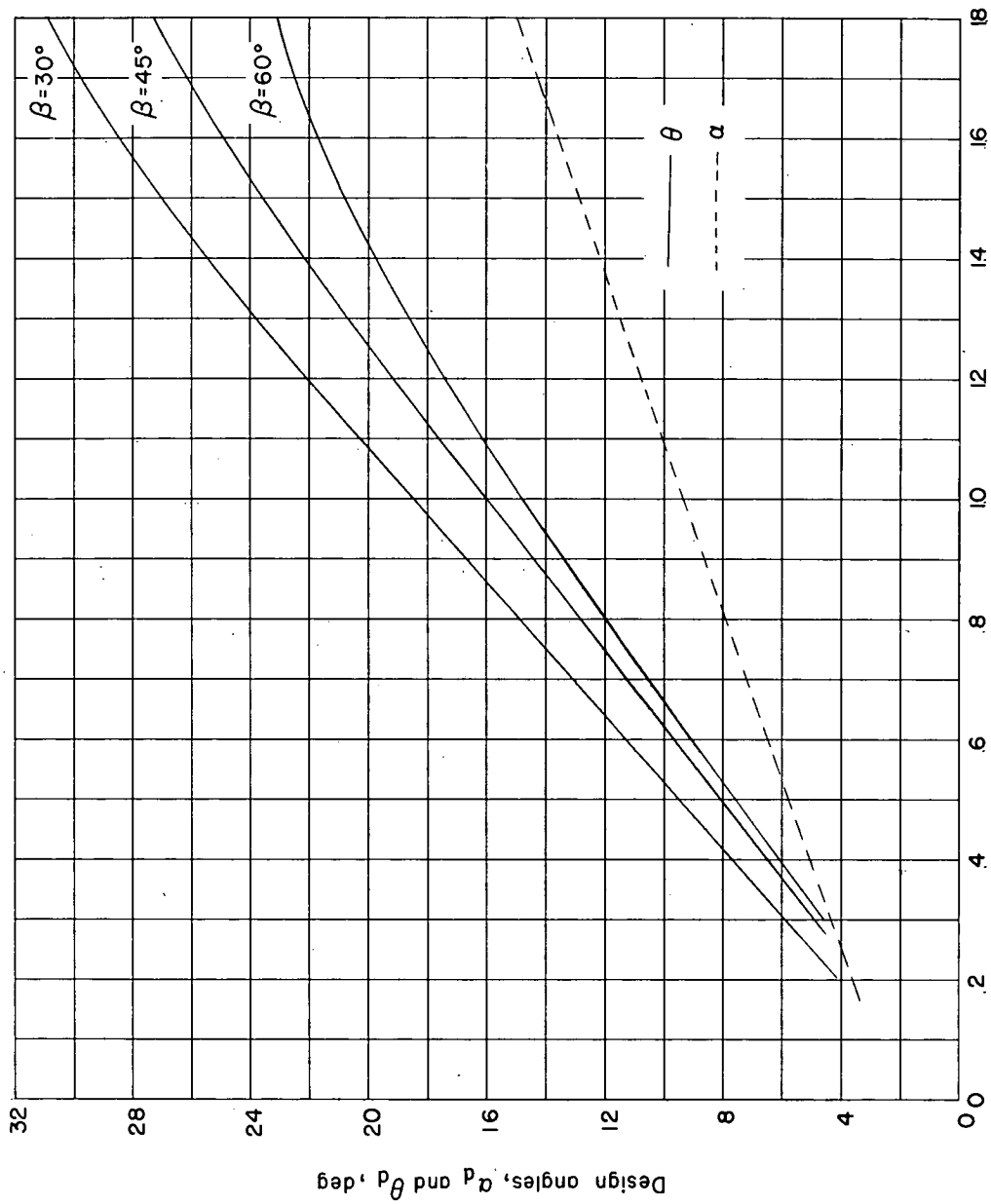

Figure 50.- Variation of design turning angle and design angle of attack with camber and inlet angle for the A_2I_8b section at $\sigma = 1.0$.

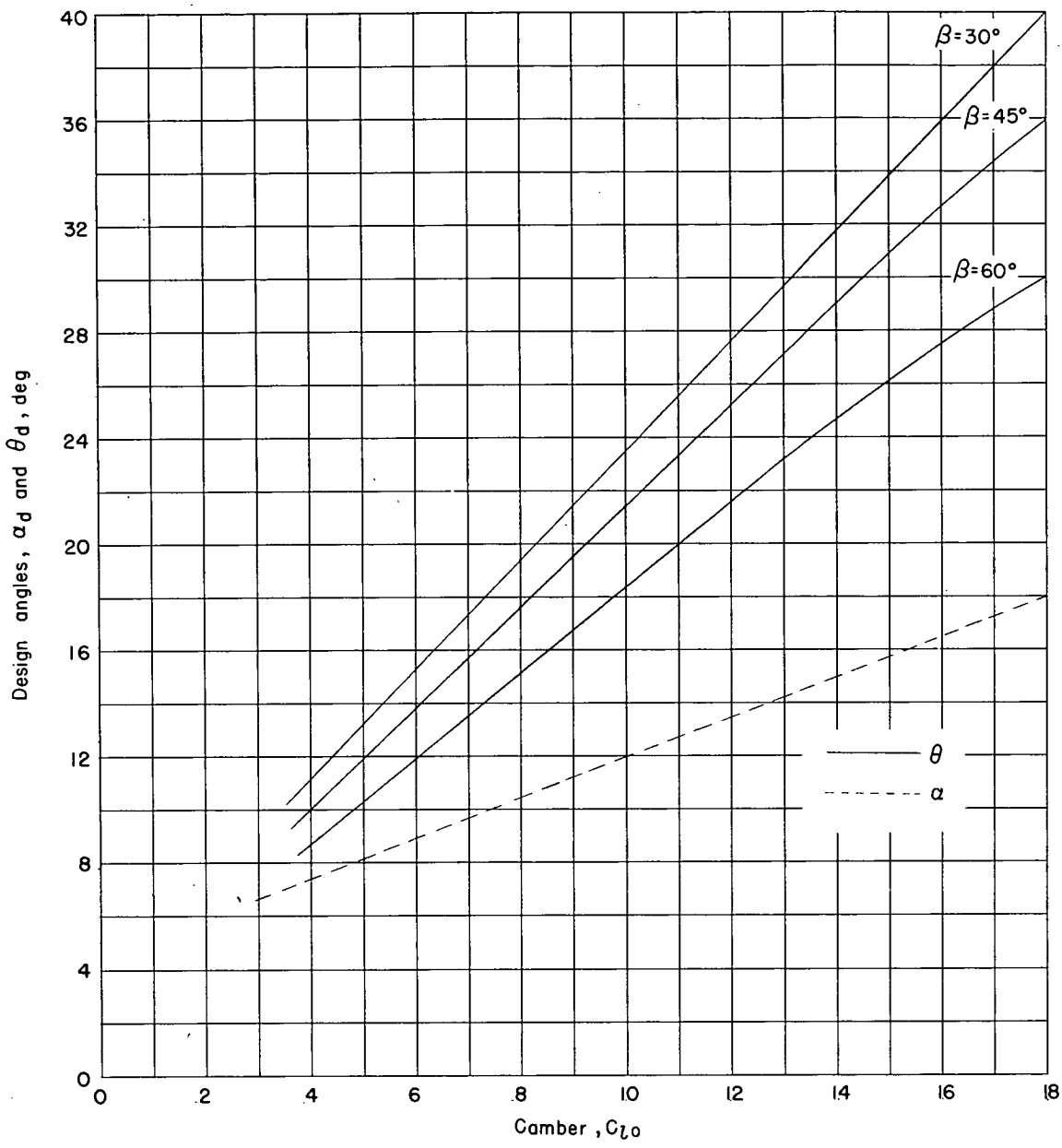

Figure 51.- Variation of design turning angle and design angle of attack with camber and inlet angle for the A_2I_{8b} section at $\sigma = 1.5$.

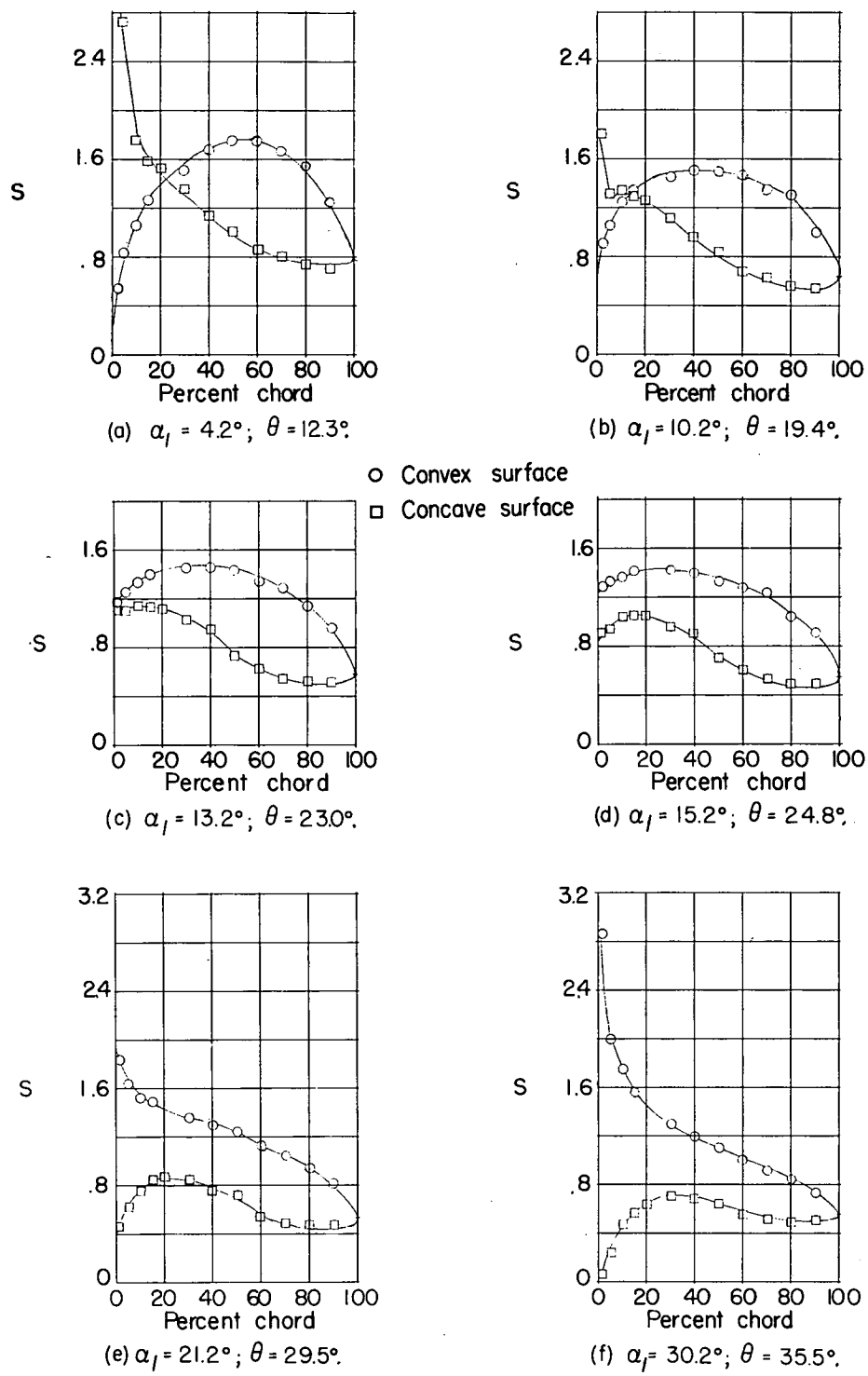

Figure 52.- Blade-surface pressure distributions and blade-section characteristics for the cascade combination $\beta_1 = 45^\circ$ and $\sigma = 1.5$ and NACA 65-$\left(12A_6I_{4b}\right)$10 blade section.

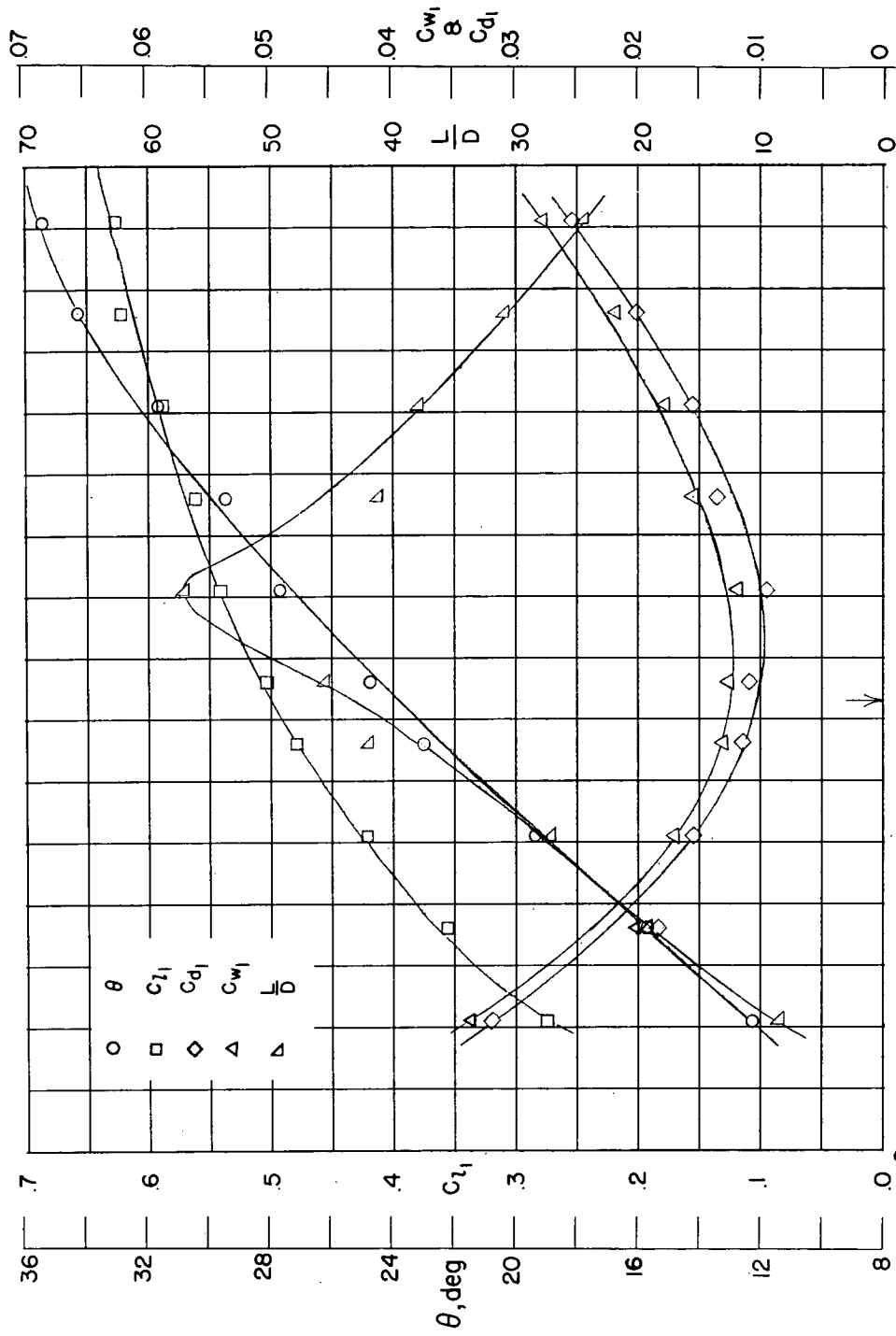

(g) Section characteristics. Arrow shows design angle of attack.

Figure 52.- Concluded.

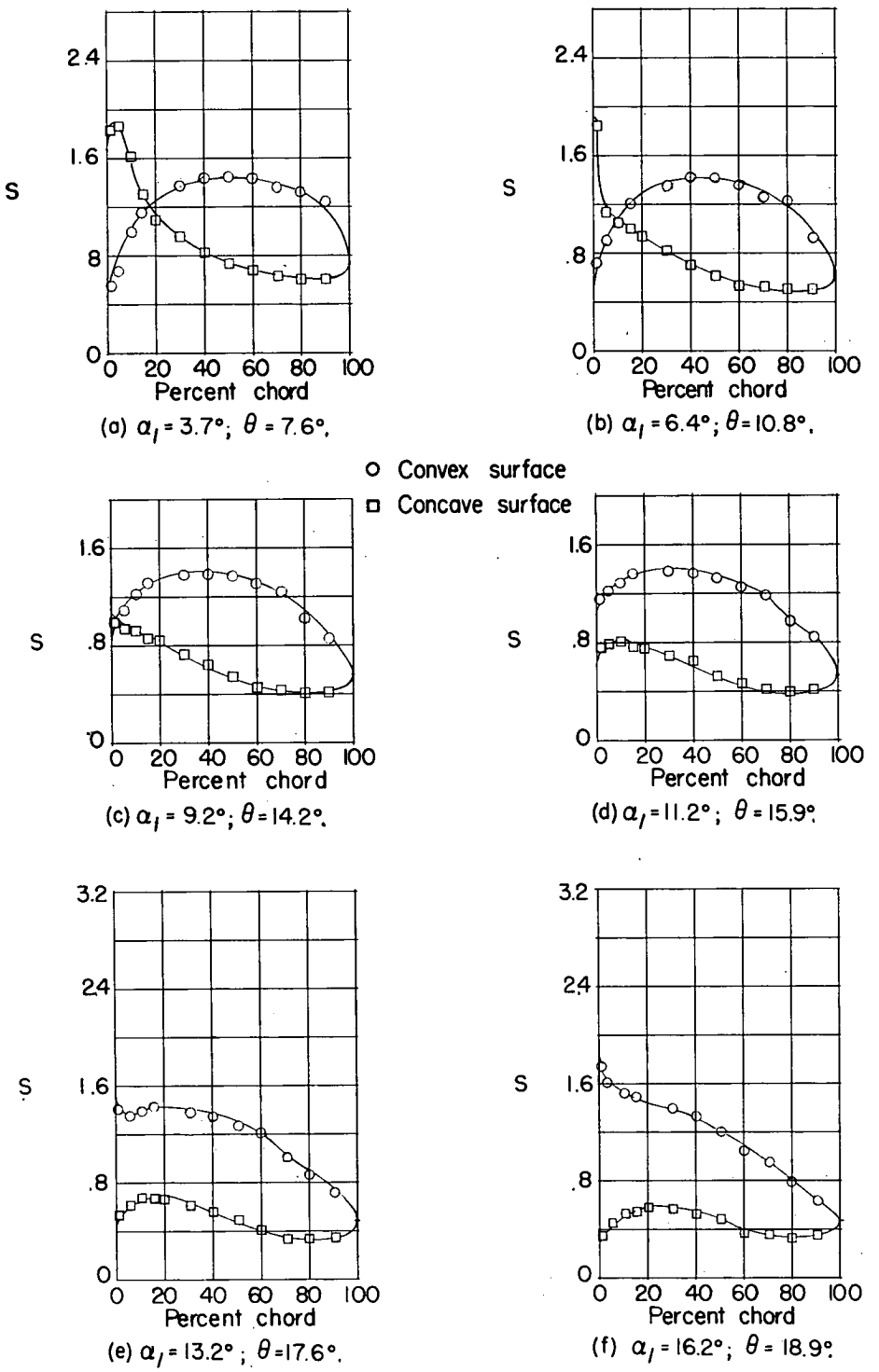

Figure 53.- Blade-surface pressure distributions and blade-section characteristics for the cascade combination $\beta_1 = 60°$ and $\sigma = 1.0$ and NACA 65-$\left(12A_6I_{4b}\right)$10 blade section.

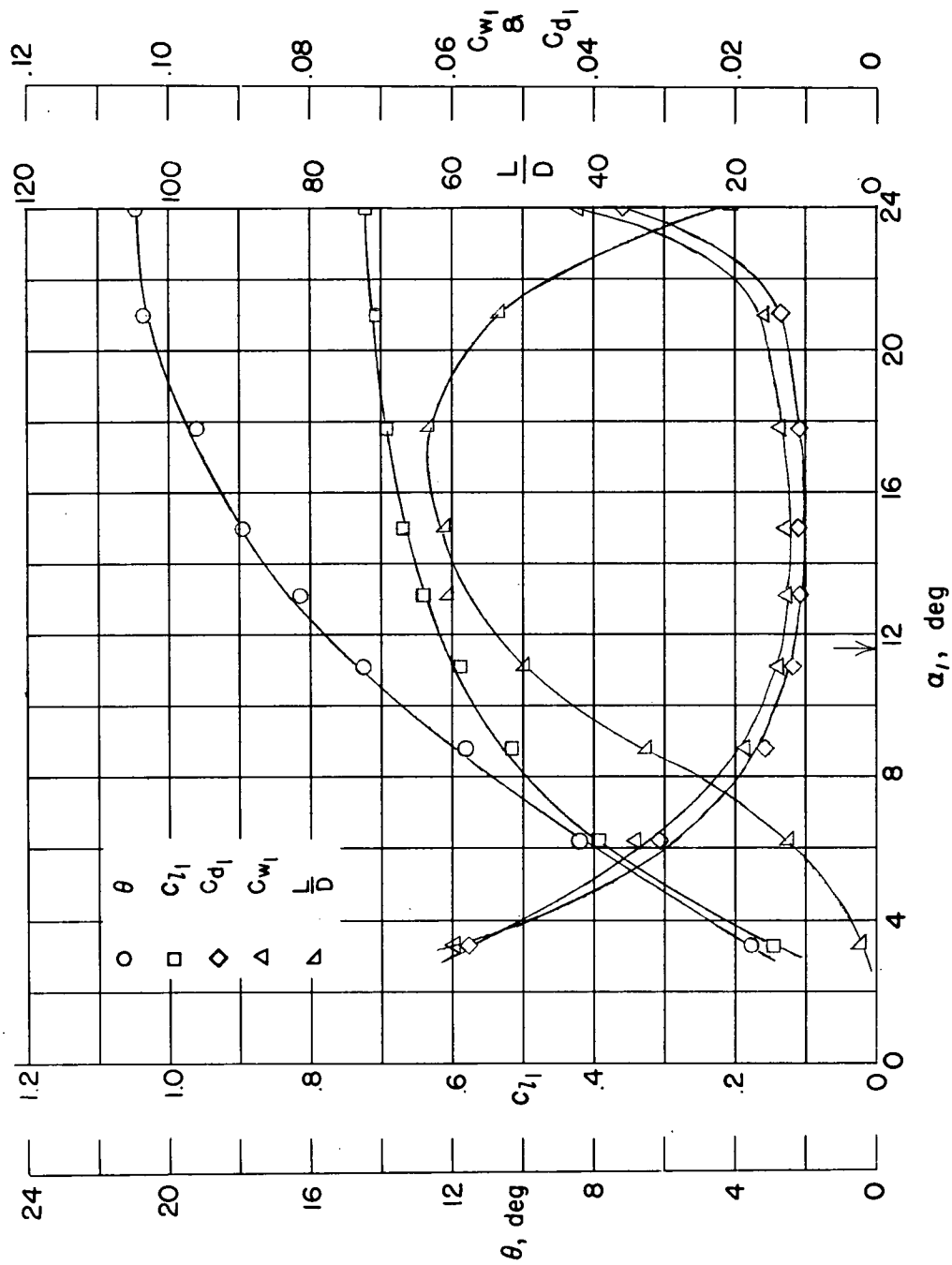

(g) Section characteristics. Arrow shows design angle of attack.

Figure 53.- Concluded.

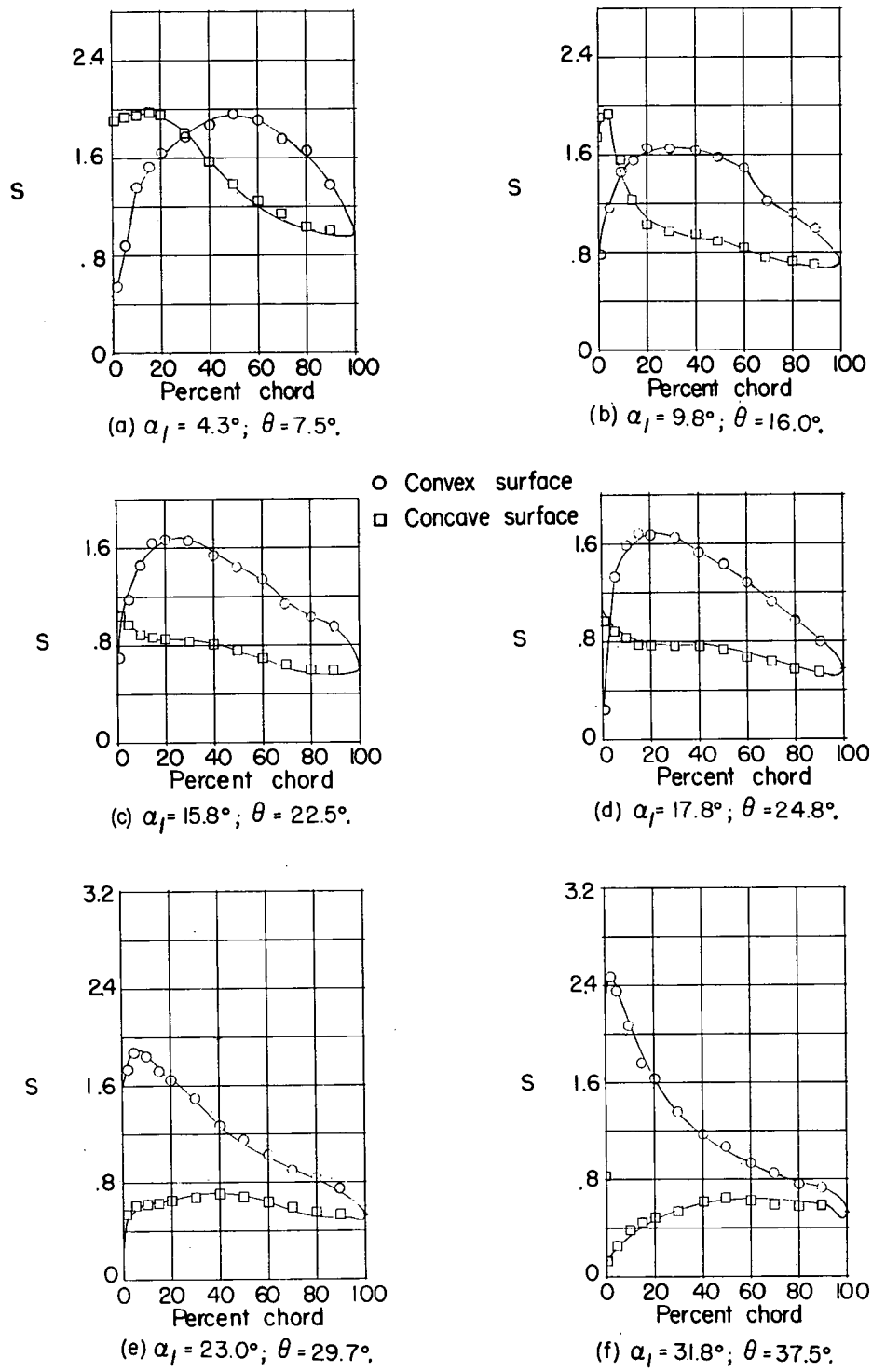

Figure 54.- Blade-surface pressure distributions and blade-section characteristics for the cascade combination $\beta_1 = 45^\circ$ and $\sigma = 1.5$ and NACA 65-$(12A_6I_4)$10 blade section.

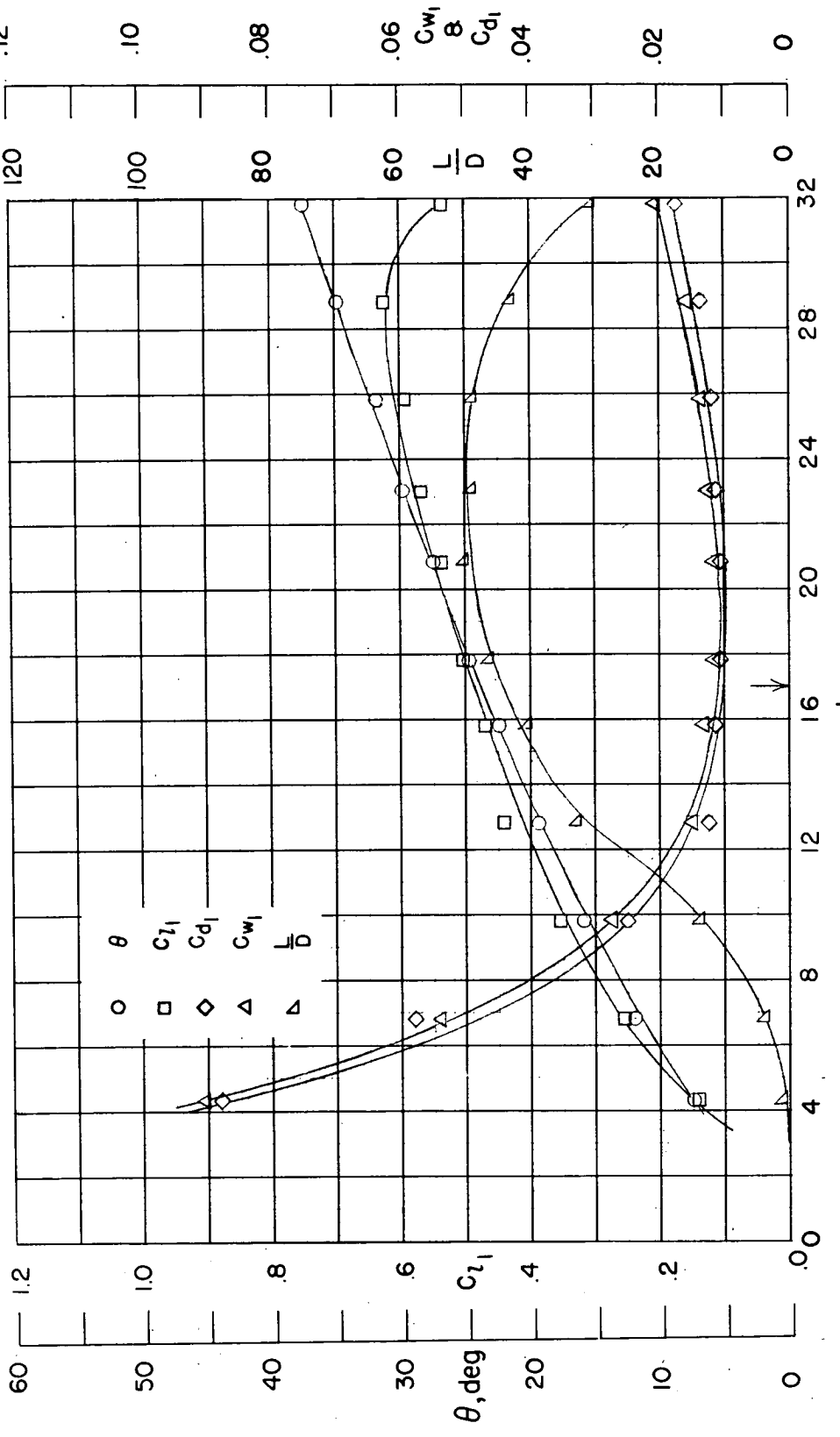

(g) Section characteristics. Arrow shows design angle of attack.

Figure 54.- Concluded.

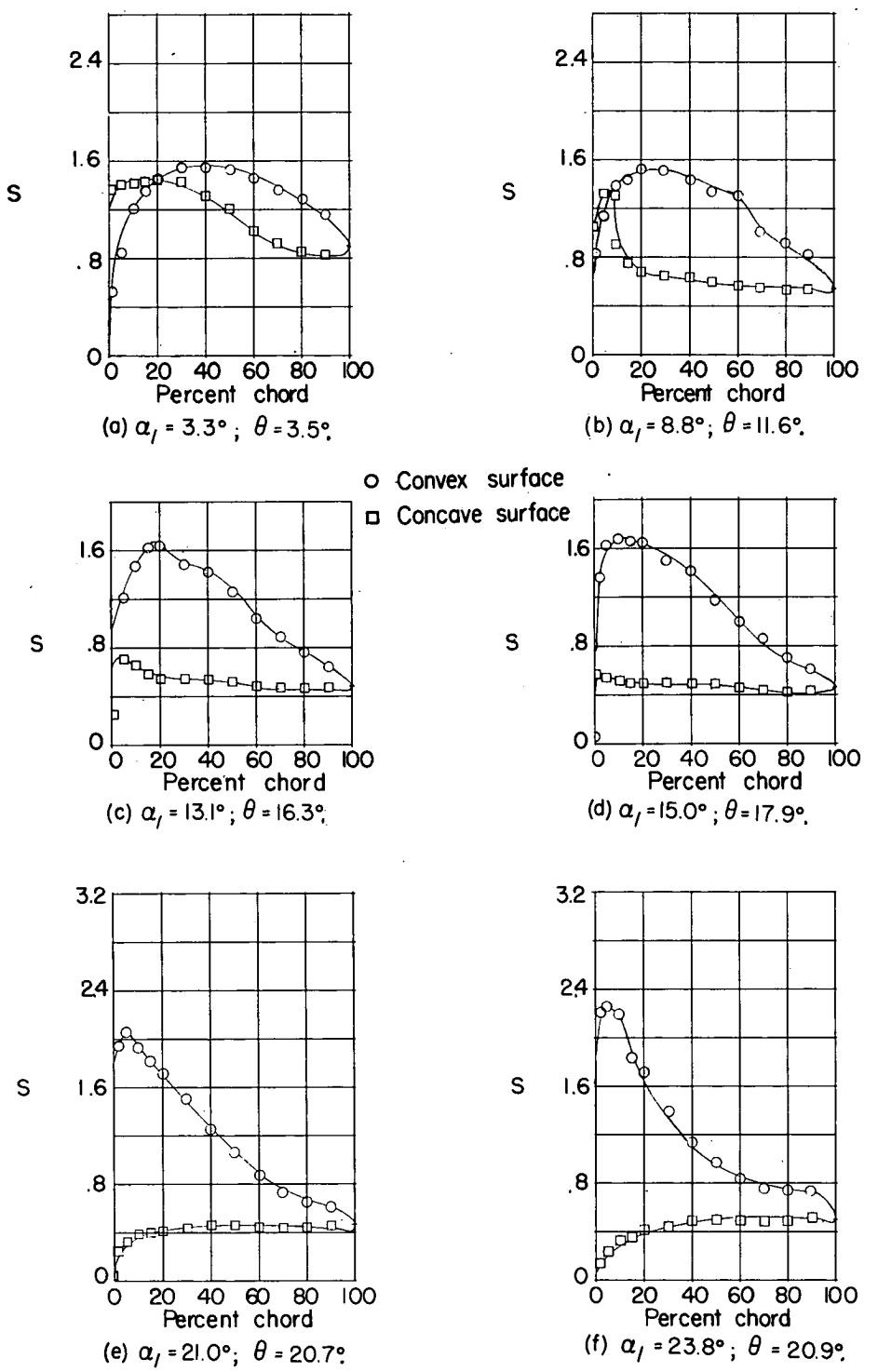

Figure 55.- Blade-surface pressure distributions and blade-section characteristics for the cascade combination $\beta_1 = 60^\circ$ and $\sigma = 1.0$ and NACA 65-$\left(12A_6I_4\right)$10 blade section.

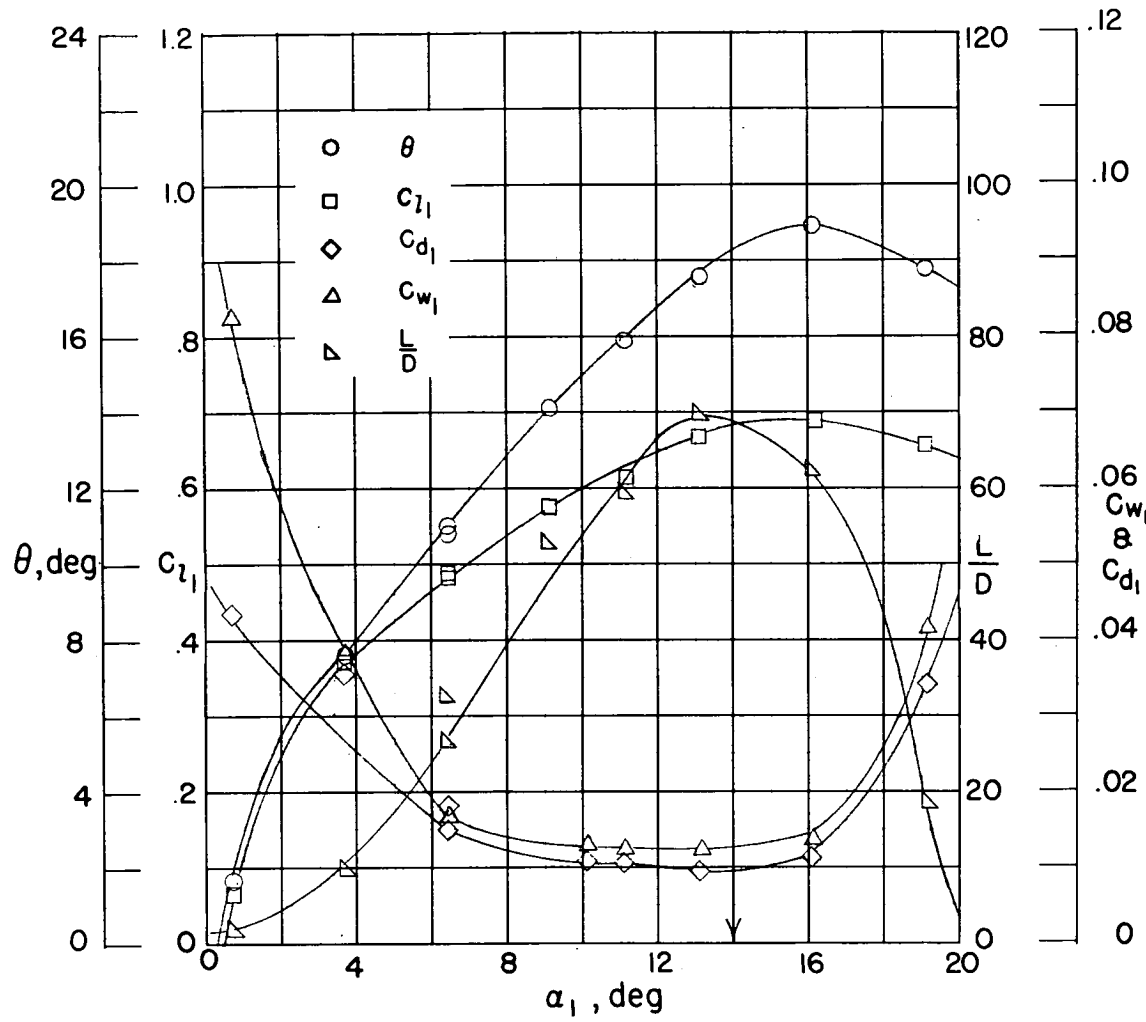

(g) Section characteristics. Arrow shows design angle of attack.

Figure 55.- Concluded.

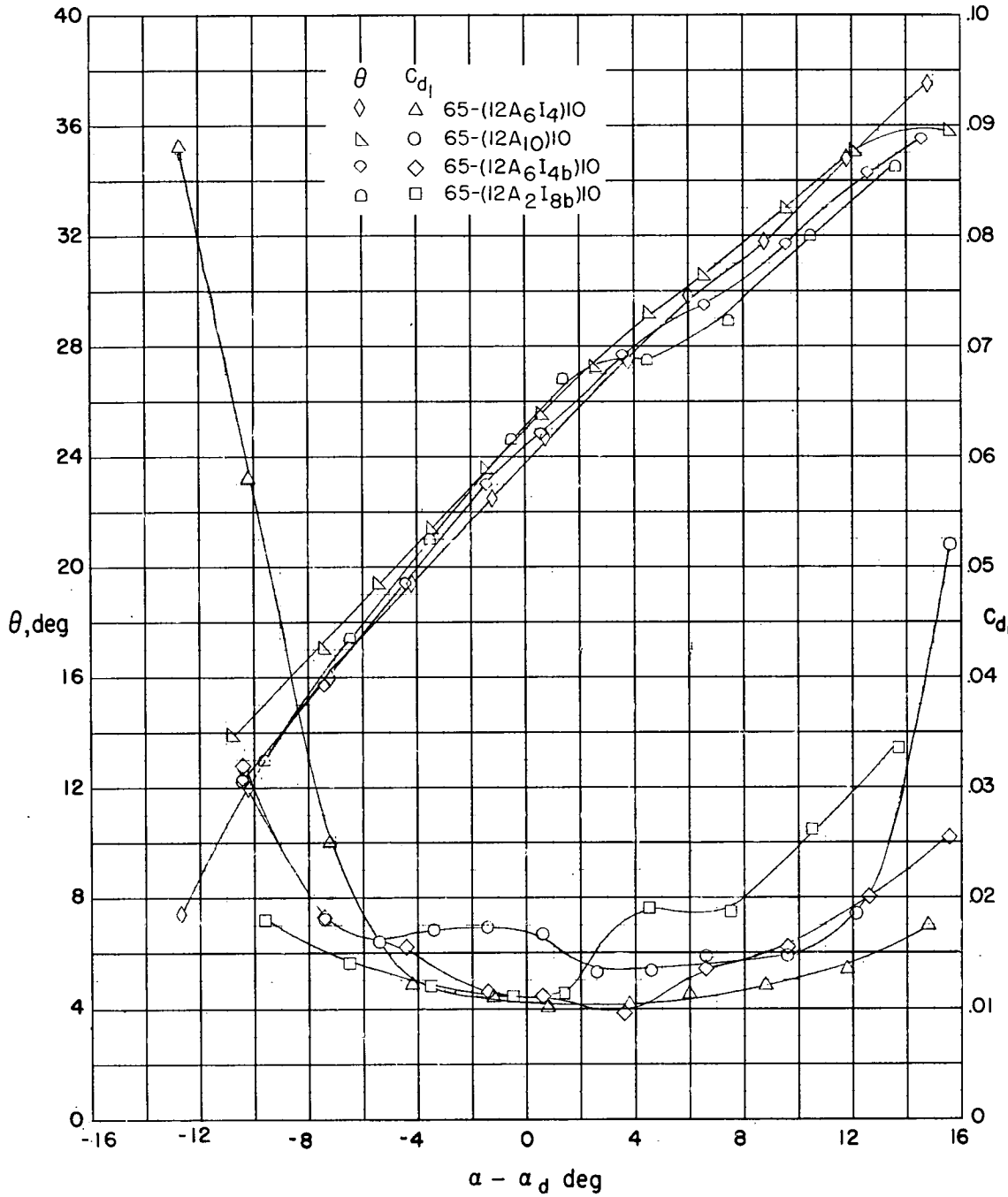

Figure 56.- Comparison of turning angle and drag-coefficient data at $\beta = 45^\circ$ and $\sigma = 1.5$ for the $C_{l_o} = 1.2$, 10-percent-thick blade sections having A_6I_4, A_{10}, A_6I_{4b}, and A_2I_{8b} mean lines over the usual angle-of-attack range.

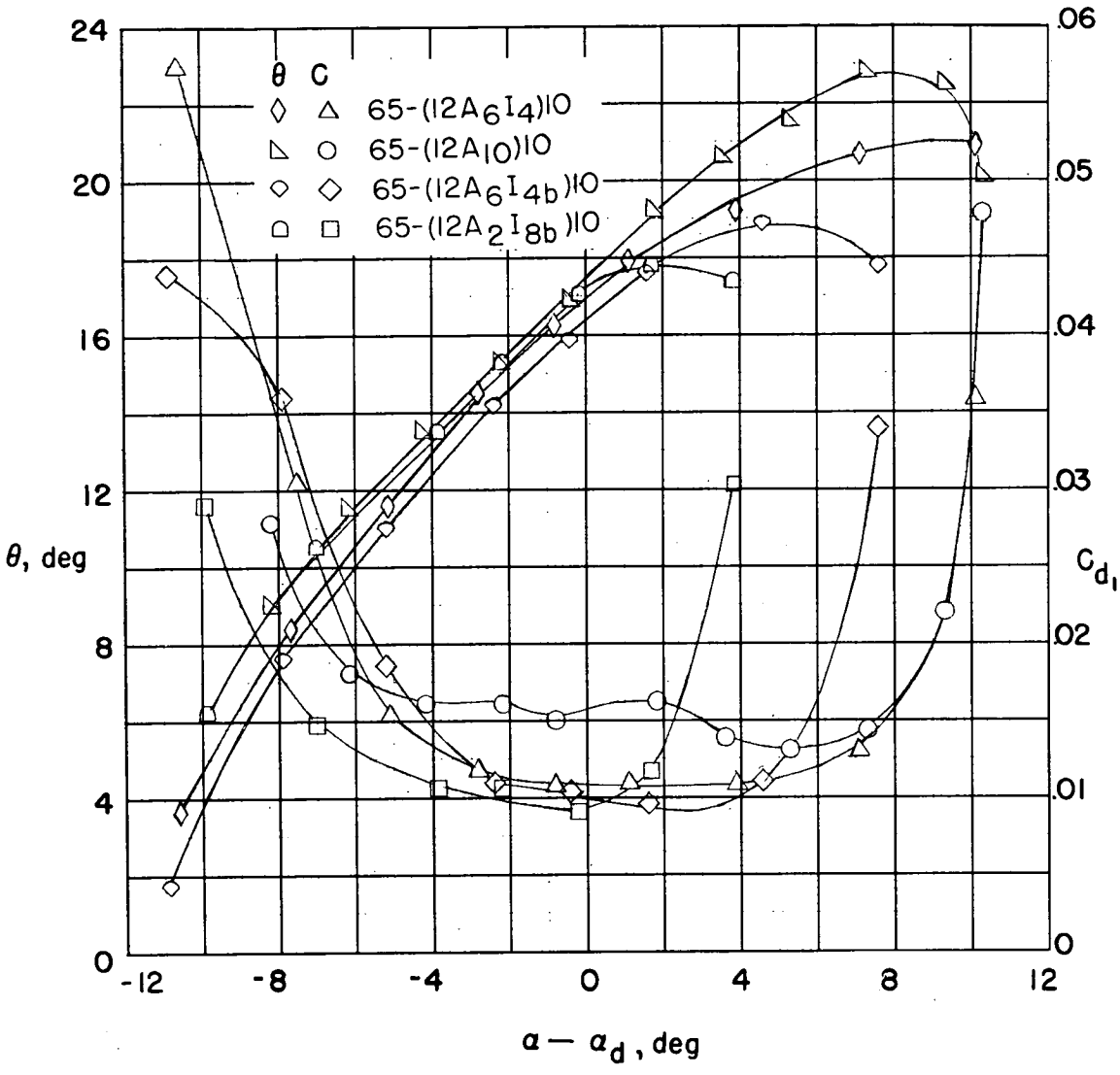

Figure 57.- Comparison of turning angle and drag-coefficient data at $\beta = 60^\circ$ and $\sigma = 1.0$ for the $C_{l_0} = 1.2$, 10-percent-thick blade sections having A_6I_4, A_{10}, A_6I_{4b}, and A_2I_{8b} mean lines over the usual angle-of-attack range.

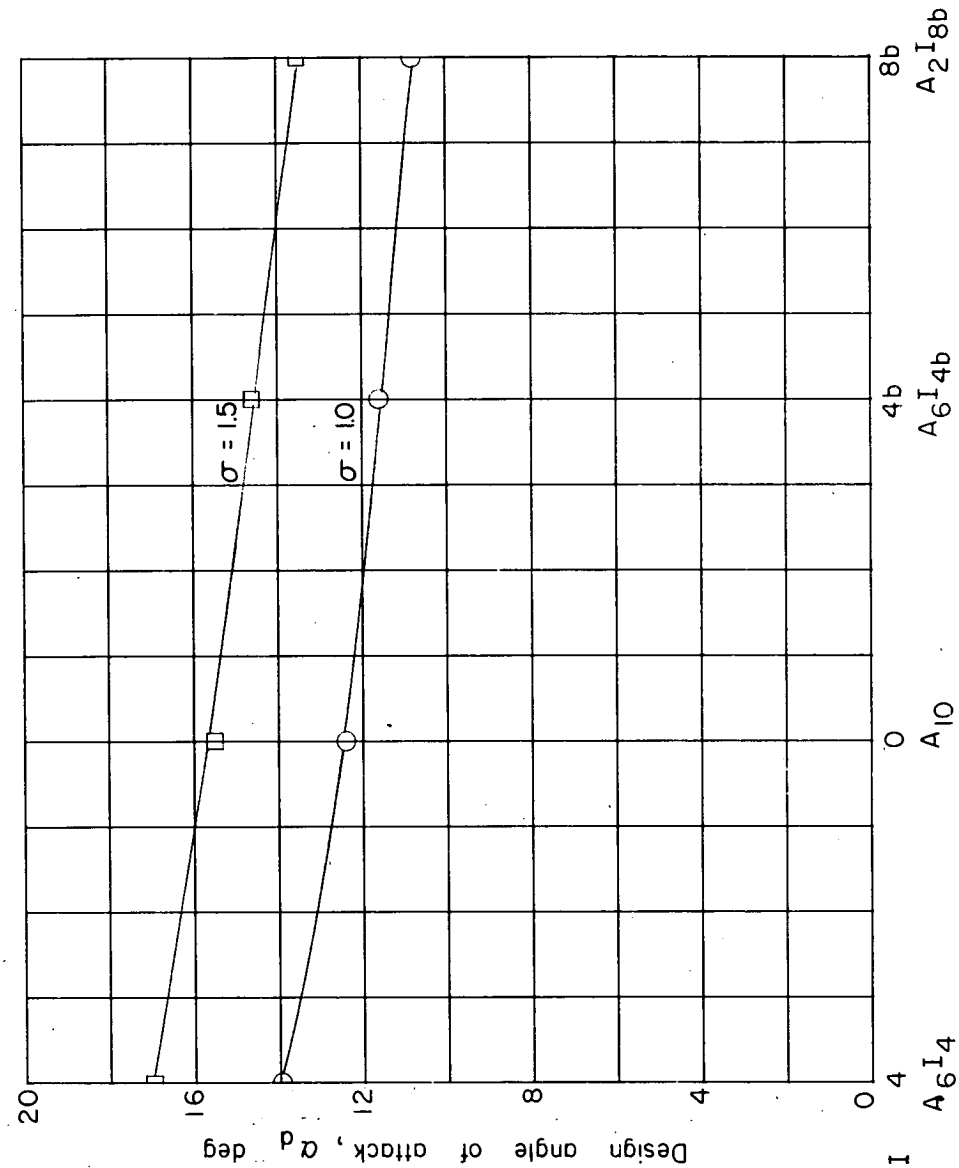

Figure 58.- Variation of α_d with changes in proportion of basic I-type loading. C_{l_o} = 1.2.

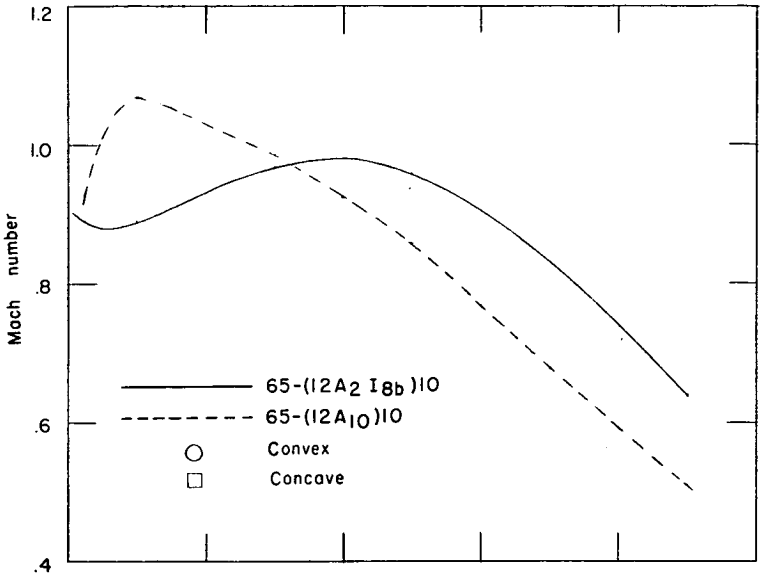

(a) Extrapolated local Mach number on convex surface.

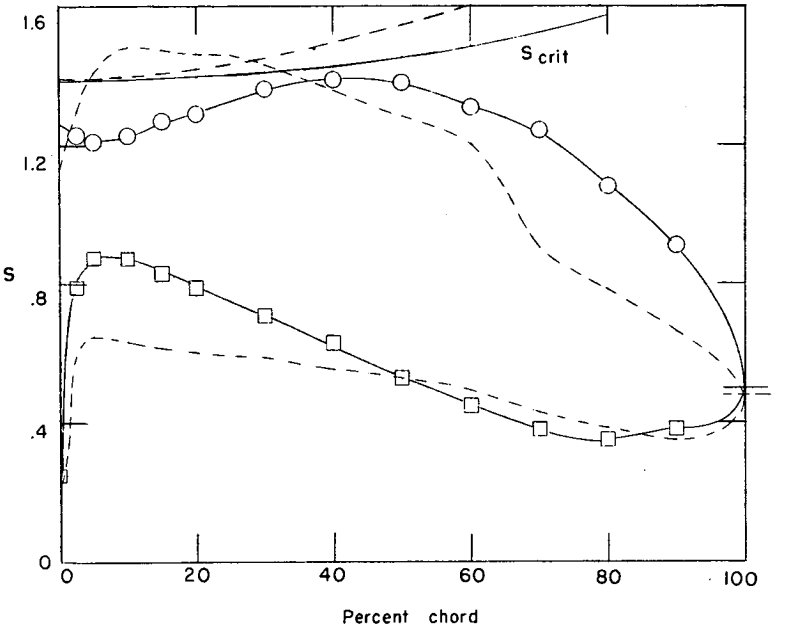

(b) Critical convex-surface pressure coefficients and low-speed pressure distributions.

Figure 59.- Comparison of extrapolated local Mach numbers and critical convex-surface pressure coefficients for an inlet Mach number of 0.75, and design low-speed pressure distributions at $\alpha_d = 10.8^\circ$ for the NACA $12A_2I_{8b}$ blade section and at $\alpha_d = 12.4^\circ$ for the NACA $12A_{10}$ blade section. $\beta = 60^\circ$; $\sigma = 1.0$.

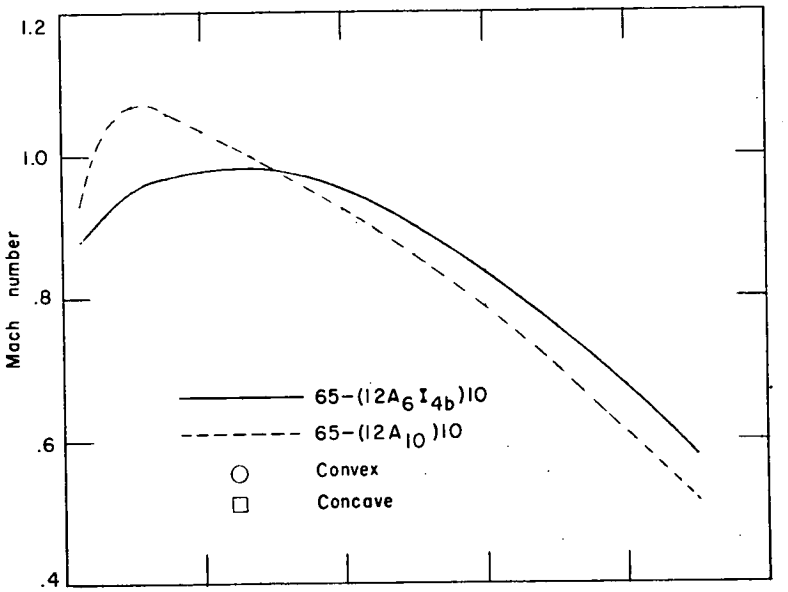

(a) Extrapolated local Mach number on convex surface.

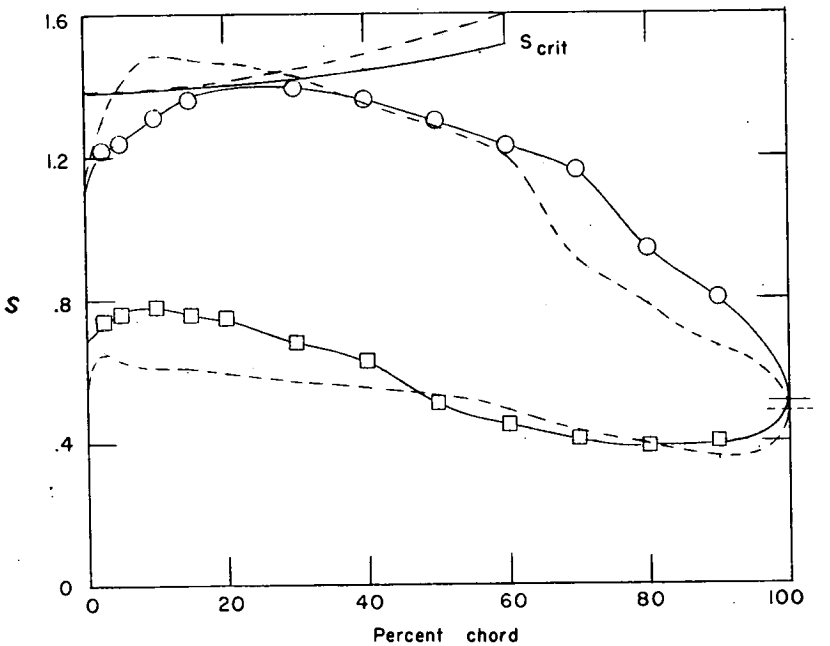

(b) Critical convex-surface pressure coefficients and low-speed pressure distributions.

Figure 60.- Comparison of extrapolated local Mach numbers and critical convex-surface pressure coefficients for an inlet Mach number of 0.75, and design low-speed pressure distributions at $\alpha_d = 11.4^\circ$ for the NACA $12A_6I_{4b}$ blade section and at $\alpha_d = 12.4^\circ$ for the NACA $12A_{10}$ blade section. $\beta = 60^\circ$; $\sigma = 1.0$.

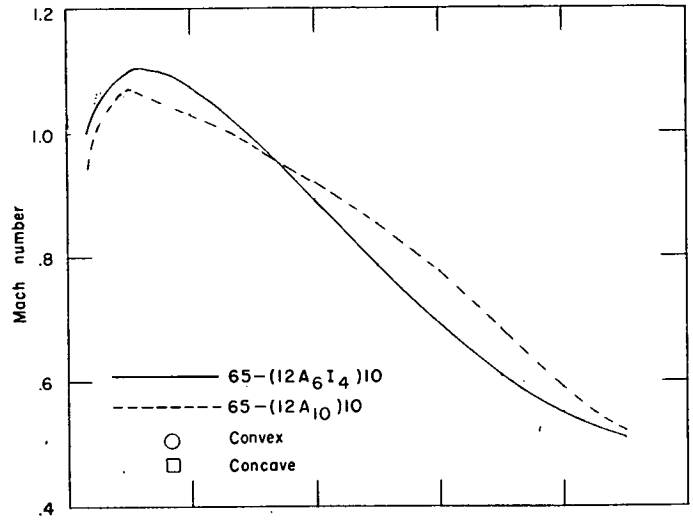

(a) Extrapolated local Mach number on convex surface.

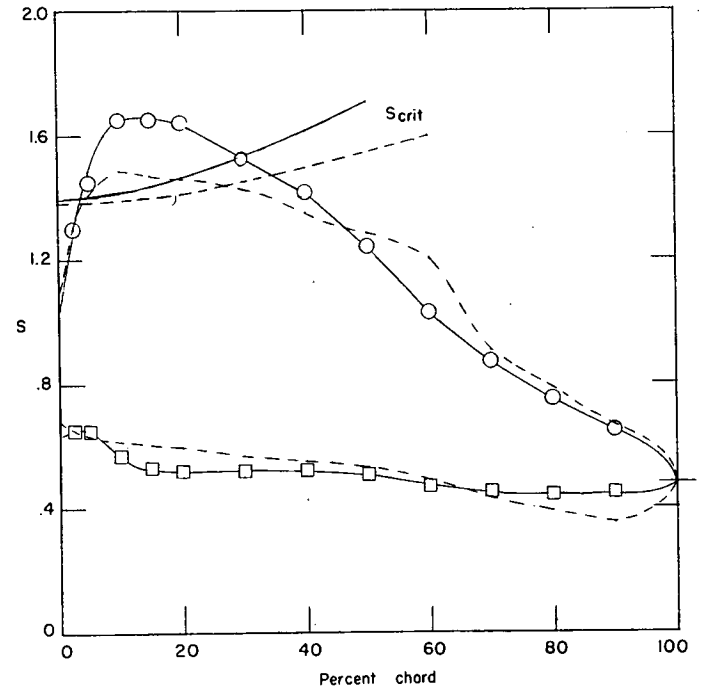

(b) Critical convex-surface pressure coefficients and low-speed pressure distributions.

Figure 61.- Comparison of extrapolated local Mach numbers and critical convex-surface pressure coefficients for an inlet Mach number of 0.75, and design low-speed pressure distributions at $\alpha_d = 14.0^\circ$ for the NACA $12A_6I_4$ blade section and at $\alpha_d = 12.4^\circ$ for the NACA $12A_{10}$ blade section. $\beta = 60^\circ$; $\sigma = 1.0$.

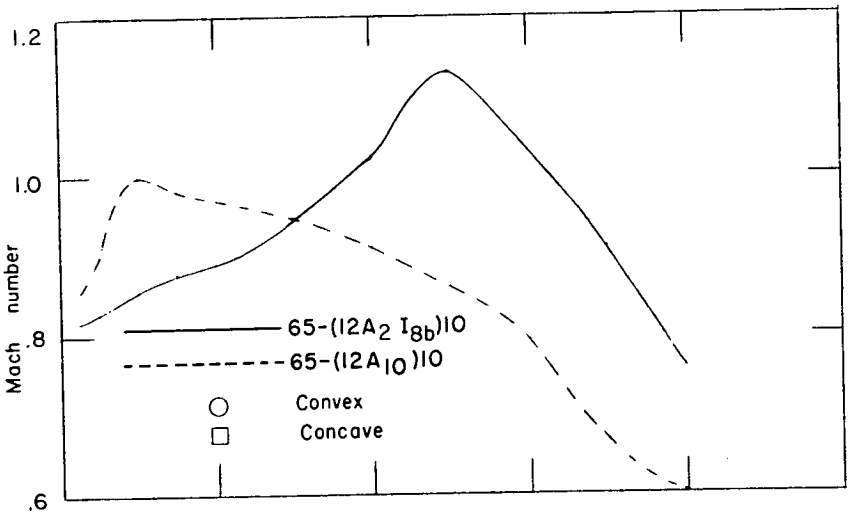

(a) Extrapolated local Mach number on convex surface.

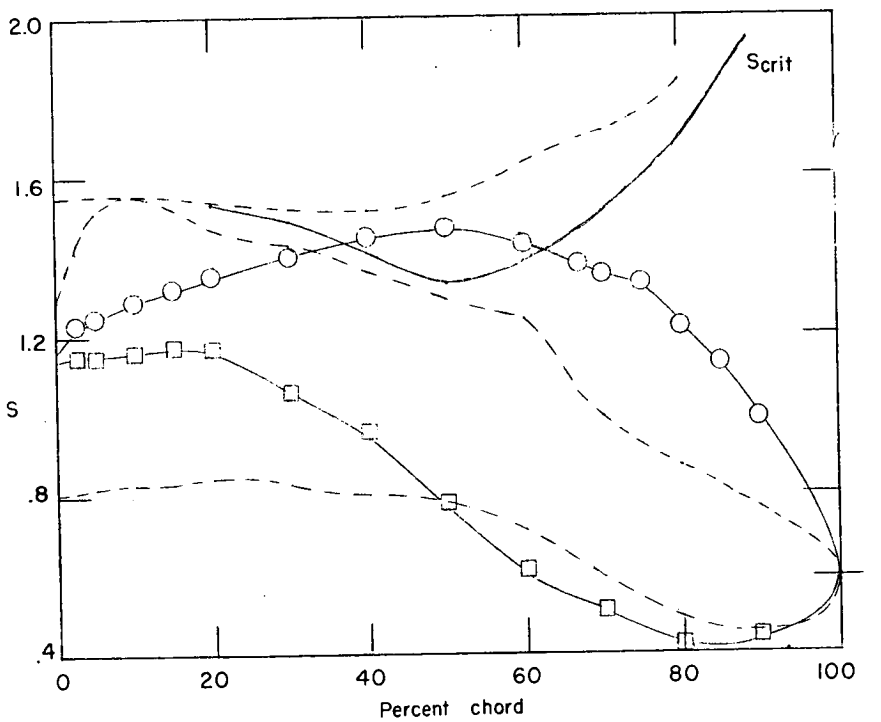

(b) Critical convex-surface pressure coefficients and low-speed pressure distributions.

Figure 62.- Comparison of extrapolated local Mach numbers and critical convex-surface pressure coefficients for an inlet Mach number of 0.70, and design low-speed pressure distributions at $\alpha_d = 13.4^\circ$ for the NACA $12A_2I_{8b}$ blade section and at $\alpha_d = 15.5^\circ$ for the NACA $12A_{10}$ blade section. $\beta = 45^\circ$; $\sigma = 1.5$.

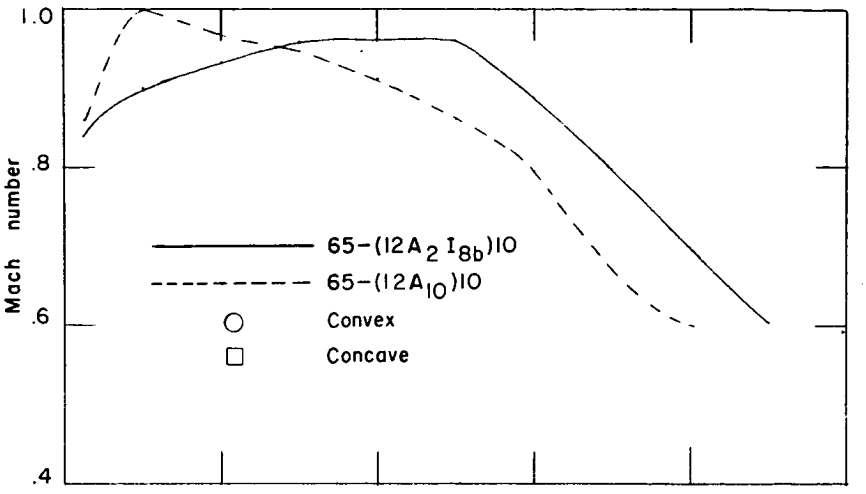

(a) Extrapolated local Mach number on convex surface.

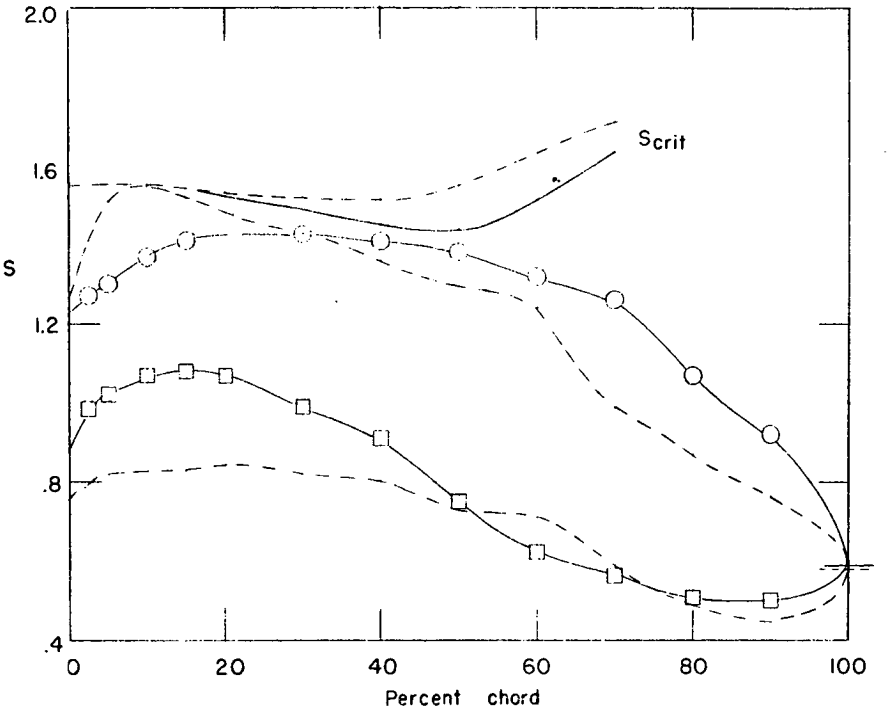

(b) Critical convex-surface pressure coefficients and low-speed pressure distributions.

Figure 63.- Comparison of extrapolated local Mach numbers and critical convex-surface pressure coefficients for an inlet Mach number of 0.70, and design low-speed pressure distributions at $\alpha_d = 14.6^\circ$ for the NACA $12A_6I_{4b}$ blade section and at $\alpha_d = 15.5^\circ$ for the NACA $12A_{10}$ blade section. $\beta = 45^\circ$; $\sigma = 1.5$.

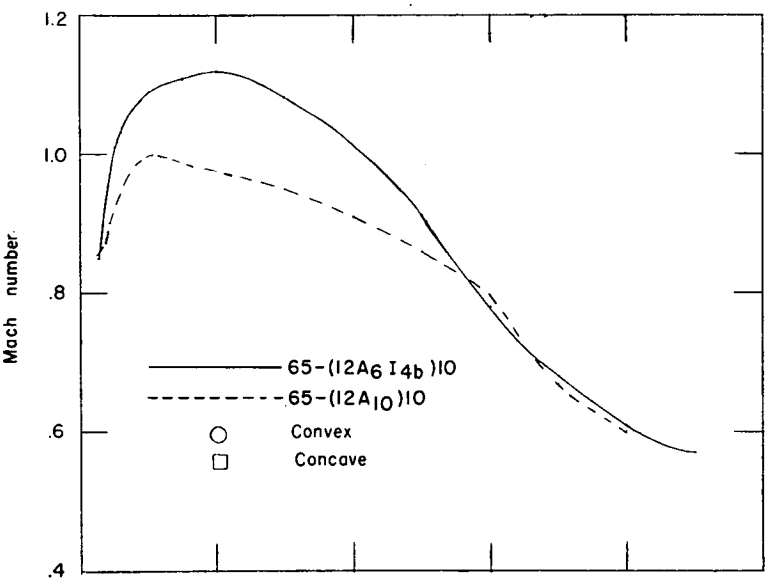

(a) Extrapolated local Mach number on convex surface.

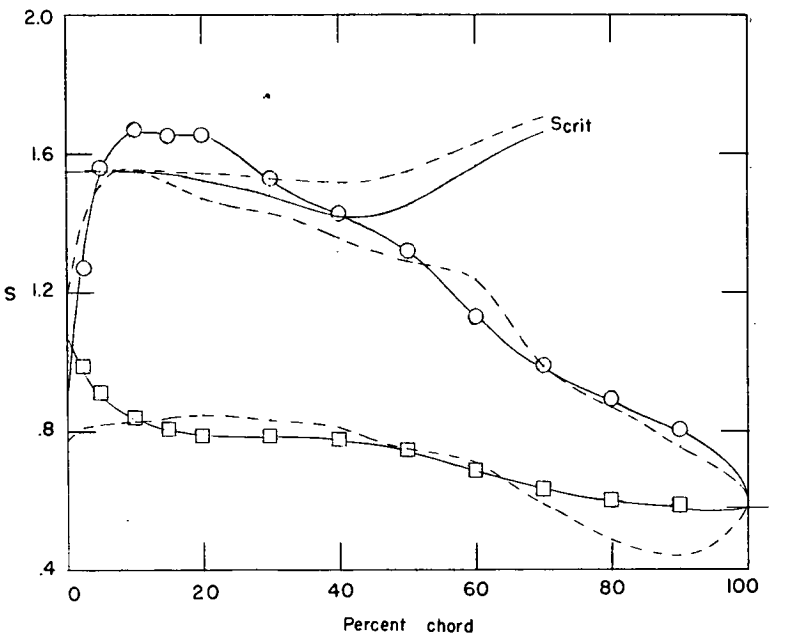

(b) Critical convex-surface pressure coefficients and low-speed pressure distributions.

Figure 64.- Comparison of extrapolated local Mach numbers and critical convex-surface pressure coefficients for an inlet Mach number of 0.70, and design low-speed pressure distributions at $\alpha_d = 17.0^\circ$ for the NACA $12A_6I_4$ blade section and at $\alpha_d = 15.5^\circ$ for the NACA $12A_{10}$ blade section. $\beta = 45^\circ$; $\sigma = 1.5$.

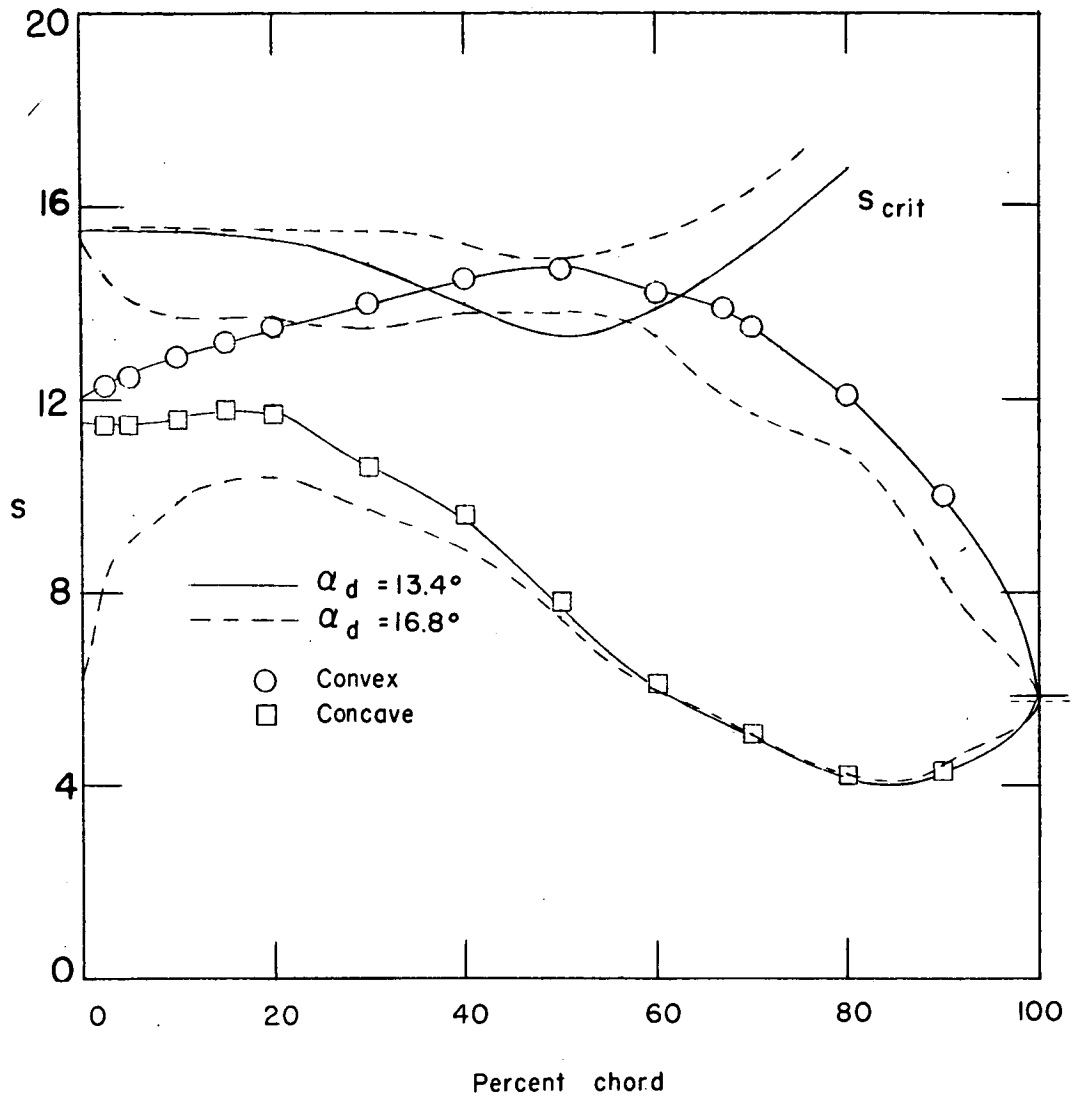

Figure 65.- Critical convex-surface pressure coefficients for an inlet Mach number of 0.70 and low-speed pressure distributions at $\alpha_d = 13.4^\circ$ and $\alpha = 16.8^\circ$ for the NACA $65\left(12A_2I_{8b}\right)10$ blade section. $\beta = 45^\circ$; $\sigma = 1.5$.

NACA-Langley - 11-25-53 - 325